
A Coherent Frequency Comb in the Extreme Ultraviolet

Christoph Gohle



München 2006

A Coherent Frequency Comb in the Extreme Ultraviolet

Christoph Gohle

Dissertation
an der Fakultät der Physik
der Ludwig–Maximilians–Universität
München

vorgelegt von
Christoph Gohle
aus München

München, den 21. März 2006

Erstgutachter: Prof. Dr. Theodor W. Hänsch

Zweitgutachter: Prof. Dr. Ferenc Krausz

Tag der mündlichen Prüfung: 26. April 2006

Inhaltsverzeichnis

Zusammenfassung	vii
Abstract	viii
1 Introduction	1
2 Frequency comb generators	5
2.1 Combs - Bridging large frequency gaps	5
2.2 Femtosecond lasers as comb generators	7
2.3 Spectroscopy with frequency combs	12
2.3.1 Single mode	12
2.3.2 Two-photon spectroscopy	13
2.3.3 Fourier transform spectrometry	15
3 Theoretical aspects of extreme ultraviolet frequency comb generation	19
3.1 High harmonic generation	21
3.1.1 The simple man's model	22
3.1.2 Macroscopic response	28
3.1.3 Noise sources and upconversion	28
3.2 Enhancement resonators for frequency combs	31
3.2.1 Passive optical resonators	32
3.2.2 Femtosecond pulses in dispersive resonators	35
3.2.3 Dispersion control	41
3.2.4 Precise dispersion characterization	46
3.2.5 Mirror reflectance measurement	50
3.2.6 Resonators as noise filters	59
3.2.7 "Solitonic" resonators	60
4 Experimental realization of an XUV frequency comb	63
4.1 Implementation of a fs-enhancement resonator	63
4.1.1 The laser system	63
4.1.2 Resonator mode and mode matching	66
4.1.3 Dispersion control and losses	68

4.1.4	Temporal pulse shaping	70
4.1.5	Electronic feedback loop	70
4.1.6	Diagnostics	72
4.1.7	Results and discussion	73
4.2	High harmonics in a resonator	78
4.2.1	Coupling	79
4.2.2	Harmonic spectrum and coherence	82
4.2.3	Discussion	87
5	Outlook	93
A	Quantum mechanical description of the atomic polarization	97
A.1	Solution in the strong field limit	97
A.2	Dipole spectrum for harmonic and frequency comb drive	100
A.3	Phase of the generated radiation	101
	Danke	111

Zusammenfassung

Im Verlauf dieser Arbeit wurde ein System entworfen und gebaut, welches einen Femtosekunden-Frequenzkammlaser durch nichtlineare Konversion in den vakuumultravioletten (VUV) Spektralbereich (120-30 nm) überträgt.

Der optische Frequenzkamm, für den im Jahr 2005 der Nobelpreis an John Hall und Theodor W. Hänsch verliehen wurde, ist ein unverzichtbares Werkzeug der Präzisionsspektroskopie geworden. Mit der Hilfe eines modengekoppelten Femtosekundenlasers ist es dabei möglich, die Radiofrequenzdomäne, in der die heutzutage genauesten Uhren arbeiten, und den Frequenzbereich des sichtbaren Lichtes miteinander zu verbinden. Damit wurde es erstmals möglich, beliebige optische Frequenzen direkt mit einer Cäsiumatomuhr, unserem primären Zeitstandard, zu vergleichen, sodass optische Frequenzen auf 15 Dezimalstellen genau bestimmt werden konnten. Unter anderem konnte mit dieser Methode einer der genauesten Tests der Quantenelektrodynamik (QED) im Rahmen der Bestimmung der 1S-2S Frequenz von atomarem Wasserstoff in einem unserer Labors durchgeführt werden. Aber auch neuartige Experimente in der Ultrakurzzeitphysik, welche eine präzise Kontrolle der optischen Wellenform benötigen, stützen sich auf die Frequenzkammetechnik.

Die Frequenzkammtechnologie in neue Spektralbereiche auszudehnen bietet viele interessante Möglichkeiten. Insbesondere ist es nützlich, die einzigartige Kombination aus hoher Spitzenleistung im Megawattbereich und großer spektraler Güte der einzelnen Kammlinien (Größenordnung 10^{14}) eines Femtosekundenfrequenzkammes auszunutzen. Zu diesem Zweck wird, bei der in der vorliegenden Arbeit vorgestellten Methode, der Femtosekundenpulszug in einen optischen Resonator hoher Güte eingekoppelt. Durch diesen Trick erhält man innerhalb der Resonatoranordnung Feldstärken, welche die des treibenden Lasers um ein Vielfaches übertreffen und deshalb einen nichtlinearen Prozess hoher Ordnung innerhalb eines Mediums aus Xenonatomen besonders effizient treiben können. Dadurch werden Harmonische des treibenden Frequenzkammes bis zur fünfzehnten Ordnung erzeugt. Das generierte Licht reicht damit bis weit in den VUV-Spektralbereich und enthält Photonen mit Energien von mehr als 20 eV. Dies ist ein Frequenzbereich der herkömmlichen kontinuierlichen Laser nicht oder nur schwer zugänglich ist, sodass mit der vorgestellten Quelle direkte Frequenzmessungen bei hohen Photonenergien erstmals in den Bereich des Möglichen rücken.

Insbesondere soll eine weiterentwickelte Variante der in dieser Arbeit demonstrierten VUV Frequenzkammquelle dazu verwendet werden, das traditionsreiche Projekt unserer Arbeitsgruppe, die 1S-2S Spektroskopie an atomarem Wasserstoff, in eine neue Runde zu führen. Der erzeugte Frequenzkamm in der Nähe von 60 nm soll zur direkten 1S-2S Spektroskopie an einfach geladenem Helium, einem wasserstoffähnlichen System mit erhöhter Kernladung, verwendet werden. Von einer solchen Messung erwartet man eine, im Vergleich mit Wasserstoff, erhöhte Empfindlichkeit auf relativistische Korrekturen aus der QED, da das System generell höhere Energien aufweist. Damit könnte ein Test erhöhter Empfindlichkeit für die Theorie der QED realisiert werden.

Weitere Anwendungen der kompakten und relativ einfachen kohärenten Quelle für VUV Strahlung könnten in der hochauflösenden Mikroskopie, VUV Holographie aber auch in der Ultrakurzzeit-spektroskopie liegen.

Abstract

In the course of this work, a system was designed and developed to nonlinearly convert a femtosecond frequency comb laser into the extreme ultraviolet (XUV) spectral range (120-30 nm).

The optical frequency comb, for which the nobel prize 2005 was awarded to John Hall and Theodor W. Hänsch, has become an indispensable tool for high precision spectroscopy. With the aid of a mode locked femtosecond laser it is possible to directly and phase coherently link the radio frequency domain and the frequency range of visible light. Today's most accurate time standard, the cesium atomic clock operates in the former and therefore it became possible for the first time to compare arbitrary optical frequencies with our primary time standard and measure them with 15 digits of accuracy. Among other things, this method allowed one of the most accurate test of quantum electrodynamics (QED) today in the course of the determination of the 1S-2S transition frequency of atomic hydrogen that is carried out in one of our labs. But also experiments in the field of ultrafast physics rely on the frequency comb technique to generate precisely controlled optical waveforms.

An especially intriguing possibility is to exploit the unique combination of high peak power in the megawatt range and the high spectral quality (on the order of 10^{14}) of single comb modes of a femtosecond frequency comb. To this end, in the method presented in this thesis, the femtosecond pulse train is coupled to an optical resonator of high finesse. With this trick, the field strength inside the resonator exceeds the driving lasers field by almost an order of magnitude. Enough to efficiently drive a nonlinear process of high order inside a medium of xenon atoms. As a result harmonics of the driving frequency comb up to 15th order are generated. The obtained field contains photons with energies exceeding 20 eV, a spectral region which is not or only hard to access by conventional continuous laser source. Therefore the presented XUV frequency comb source brings direct frequency measurements at such high photon energies into the realm of possibility for the first time.

In particular, an improved version of the demonstrated source will be used to take the next step in an experiment with a long tradition in our group, the 1S-2S spectroscopy of atomic hydrogen. The generated frequency comb in the vicinity of 60 nm wave length will be used to probe the 1S-2S transition in singly charged helium, a hydrogen like system with larger nuclear charge. From such a measurement it can be expected that, compared to hydrogen, relativistic corrections from the QED theory become more important as the system has higher energies in general. For this reason this could lead to a test of QED with increased sensitivity.

Other applications of such a compact and relatively simple coherent source of XUV radiation could be high resolution spectroscopy, XUV holography, but could also lie in the research area of ultrafast physics.

Chapter 1

Introduction

At all times, attempts to construct abstract and simple theories that explain phenomena observed in nature within a general context have led to new insight into the fabric of reality as well as it has enabled the invention of new techniques and tools that changed everyday life. As an example, the discovery of atomic line spectra and the photoelectric effect has led to the development of quantum mechanics, which is the basis for understanding the structure of solid matter¹ and has led to the development of electronics enabling such nice gadgets like televisions, microwave ovens and desktop computers. Conversely, the attempt to unify theories that describe separate fields of natural phenomena has triggered the discovery of the new phenomena. The opposition of Galilean invariance of Newtonian mechanics and Lorentz symmetry of the theory of electromagnetic fields led to the discovery of the theory of special relativity with its real life implications like the constancy of the speed of light, which was tested in the historic work of Michelson and Morley (1887) and time dilation (Rossi and Hall 1941), to name only a few. This interplay between theoretical insight and empirical studies of reality is the basis for all natural sciences and is crucial in the most fundamental of all these disciplines, physics².

Existing theories therefore require constant revision and verification in different contexts, as a theory, good as it may be for certain problems, can as well completely fail to predict essential features within others. Especially looking at extreme conditions within the physical parameter space has proven to be a very efficient way to discover new physics beyond the existing theories. For example high energy physics, which involves acceleration of the smallest constituents of matter to highest achievable energies and studies their interactions, was an inexhaustible source of new discoveries that eventually lead to the standard model of elementary particle physics. However it is not always feasible to test nature at its extremes, as for instance the energies where the standard model can be expected to become a bad approximation to reality lie more than 15 orders of magnitude above what is achievable in state of the art accelerators³. On the other hand,

¹Before the discovery of quantum mechanics (but after the discovery of atoms), it was a mystery why solids exist.

²fundamental in view of the belief that all phenomena in nature can be deduced from the the basic theories of particles and their interactions

³Current accelerators achieve energies of a few TeV (per particle), while the energy scale where the fundamental forces are expected to unify and grand unified theories (GUTs) or even string theories might become the relevant

if it is assumed that the effects of such new physics that become apparent at the extremes of the energy scale decrease continuously with the energy of the system under investigation, a possibly small signature should still be observable even at much lower energies.

At this point, precision measurements take over. If theorists can predict a measurable quantity with sufficiently high accuracy using current theory, and an experiment can also provide similar accuracy, then a comparison of these predictions and the experiment may reveal a discrepancy. Of course the required accuracy level to find discrepancies can not be predicted, as it is unknown if the theory under consideration is already correct or what a correct theory would predict for the same quantity. Cases, where precision measurements were used to identify shortcomings of old theories and helped to identify the correct one are the determination of the advance of perihelion of Mercury and the gyromagnetic factor of the electron. The advance of the Mercury perihelion was determined by astronomical observations with an accuracy better than 10^{-3} and showed a value that could not be explained using Newtonian mechanics. General relativity predicts a value that lies within the accuracy limit of the measurement, which was taken as a hint for its correctness by Einstein (1916) himself. The discrepancy of the gyromagnetic factor of the electron from the value of 2, according to the Dirac theory, that was predicted by quantum electrodynamics (QED) was found by Van Dyck Jr. et al. (1987) to agree with these predictions within one part in 10^9 . These kinds of experiments help to find (or extend) the limits of validity of the known theories without going to the extreme scales (in time, space and energy).

When comparing the accuracy that can be reached in experiments for determining different physical quantities, it turns out that time and frequency can be measured with the highest precision. The methods to determine other quantities like length, mass or charge are far more imprecise. A frequency is the number of periods of a periodic phenomenon per unit time. Therefore a frequency is as accurate as the realization of the time unit if no error is made in counting. This essentially means that determining a frequency and measuring time is fully equivalent. In fact every clock is a stable oscillator⁴ that produces a periodic phenomenon and a counter that counts the periods. Nowadays clocks based on a cesium hyperfine radio frequency transition as the oscillator are commercially available and routinely provide an accuracy of 10^{-12} . National standard institutes all over the world run Cs-atomic clocks that have an accuracy around 10^{-15} and this figure is expected to improve soon as new optical standards⁵ become available (like in Diddams et al. 2001).

Because clocks can currently be built with accuracies exceeding one part in 10^{15} and frequencies can in principle be determined with the same accuracy, it is attempted to put other physical units down to a frequency measurement. The most simple example of such an ascription is the redefinition of the meter using the speed of light in the year 1983. At that time the speed of light in vacuum was defined to be $c = 299\,792\,458$ m/s so that henceforth the length of an electromagnetic wave λ with angular frequency ω was determined via the equation $\lambda = 2\pi c/\omega$. With this trick, the accuracy of the determination of the wavelength is only given by the uncertainty in the determination of the frequency of the wave as the speed of light is no longer a quantity with

theories lie at the Planck scale, 1×10^{28} eV

⁴like a pendulum, a quartz crystal, or an atomic transition, etc.

⁵that use oscillators with optical frequencies in the PHz range

an error but a defined number. For this approach to be useful it is however necessary to provide a fine ruler of length markers, and therefore an electromagnetic wave with short wavelength is desirable. Nowadays, narrow bandwidth lasers operating in the visible spectrum are routinely available. However, the frequency associated with a visible electromagnetic wave is several hundred THz so that it is impossible to count the oscillations directly using electronic equipment. This is the reason why it took until 1983, when techniques became available that made a direct phase coherent counting of such high frequencies possible, to undertake the redefining of the meter. At that time heroic efforts were necessary to link optical frequencies to the radio frequency reference clocks using a chain of frequency multipliers, intermediate oscillators and phase-locked loops, each step using different techniques, equipment filling several laboratories and tens of hard working physicists to keep it running. Yet for each optical frequency that had to be measured a different chain of equipment was necessary. But this did not prevent physicists from using these new techniques and the associated potential accuracy of experiments that could be done with it. In our group, in collaboration with groups at Braunschweig and Novosibirsk, Russia such a frequency chain was operated to determine some transition frequencies in hydrogen and deuterium (Udem et al. 1997) that provided a novel accurate value of the ground state 1S lamb shift and a new value for the Rydberg constant. A measurement of the isotopic shift of the deuterium (Huber et al. 1998) 1S-2S transition, also performed in our labs, was able to determine the nuclear charge radius of the deuteron with a higher accuracy than scattering experiments at large accelerator facilities could provide.

Sixteen years later, in 1999 after a long period of heavy development and an unexpected convergence between ultrafast laser techniques and the ultranarrow continuous wave laser spectroscopy, a new type of universal frequency chain was created in our laboratories by Udem et al. (1999b), Reichert et al. (1999) that could directly link an optical frequency to a radio frequency using only 5 different lasers where one was a so-called optical frequency comb generator based on a mode-locked titanium sapphire laser emitting a periodic pulse train with pulses of less than 100 fs duration. This universal tool was subsequently refined and improved by Reichert et al. (2000), Diddams et al. (2000) and Holzwarth et al. (2000) and received the name "optical frequency synthesizer" to express its universality for optical frequency metrology. This induced a revolution in optical frequency metrology as it then was possible to cover essentially the entire visible spectrum with such a device and even small laboratories could now reach accuracies of 10^{-12} or better by simply using such a synthesizer together with a commercial rf primary frequency standard, a system that a single person could run and operate. Not only were many optical atomic transitions measured with this tool with previously unequalled accuracy (see for example in Niering et al. 2000, Udem et al. 2001, von Zanthier et al. 2000), but it also paved the way to reliable operation of atomic clocks using optical transitions (like in Diddams et al. 2001). These new optical atomic clocks hold the promise to improve frequency standards to even higher accuracies. Frequently it is predicted that they could reach a level of 10^{-18} .

If it is for the moment naively assumed that the effects of GUTs or string theories scale linear with energy and become strong (order of unity) when the Planck scale is approached, then the conclusion is that a measurement of accuracy 10^{-18} can detect such effects in an experiment at an energy of *only* a few GeV, energies which are accessible at many accelerator facilities all around the world. Of course this assumption is very birdbrained and the dream of applying the

mentioned high accuracy techniques to accelerator experiments is further away than a dream as frequency metrology can now reach frequencies corresponding to a few eV only. Moreover, state of the art theories are far from being able to predict the dynamics of quarks in a proton (for example) with an accuracy that comes close to 10^{-18} . Yet, the attempt to make higher frequencies and energies accessible to precision metrology holds the promise to obtain more stringent test of fundamental theories, and the work at hand tries to take first basic steps into this direction.

A more realistic goal for the present considerations is to continue the long and glorious history of hydrogen spectroscopy associated with our laboratories, but taking one step to higher energies. Singly positively charged helium ions are electronically identical to neutral hydrogen but due to the doubled nuclear charge, the energy level gross structure (i.e. the major quantum number energies) are a factor $2^2 = 4$ times higher than in hydrogen. This means that for exciting the 1S-2S transition, photons with an energy of 20 eV or 60 nm wavelength are required. Simultaneously, supporting the silly argument from the previous paragraph, the corrections of the Bohr(Schrödinger)-levels due to Dirac theory and QED scale more strongly. The Lamb shift of the ground state scales as Z^4 if Z is the nuclear charge and higher order QED corrections to the energy levels that have not (yet⁶) been verified in an experiment, scale as Z^6 and therefore both become relatively stronger compared to the transition frequency itself. Therefore it can be hoped that a precision measurement on He^+ can yield a more stringent limit on the validity of QED or maybe even a deviation from QED calculations.

The problem with the proposed spectroscopy on the 1S-2S transition of He^+ is that there was essentially no narrow bandwidth source at the required photon energy available, the reason being that 20 eV lies above the ionization threshold of any neutral atoms and molecules, not far but only just, so that the absorption cross sections are rather high and there is no discrete level structure⁷ that can support lasing. However, it is known that nonlinear up conversion of lower frequency fields can produce UV light with similar coherence properties as the fundamental wave. To be able to reach the XUV range between 10 and 100 eV, extreme nonlinear processes of high order (high order harmonic generation, HHG) are necessary, which in turn require an extremely strong driving field. It has to be so strong that the nonlinear medium disintegrates within a few (ten) laser cycles, which means that the generation process itself will cease after that time, and it is required that the power to be converted is concentrated into a bunch of similar length, a few ten femtoseconds. This means, the generation can only take place in pulsed operation, which at first sight contradicts the spectroscopic requirement of a narrow bandwidth source (1/10 fs \sim 100 THz). On the other hand, it is known that a periodic train of ultrashort pulses produces a frequency comb spectrum that is quasi-cw in the sense that the broadband power is concentrated into a equidistant array of isolated single frequency components, each of them essentially a continuous harmonic source. This thesis documents an attempt to design and build an XUV source based on HHG with sufficiently high repetition rate that the frequency comb, which is expected to survive the process of HHG, can be used for high resolution spectroscopy in a wavelength range previously inaccessible to frequency metrology.

⁶Once the proton charge radius is determined by a group at PSI (Switzerland) working on muonic hydrogen, these corrections can be verified with the results already obtained with the hydrogen experiment in our group. A description of the experiment that is being prepared at PSI was presented by Kottmann et al. (2001).

⁷because the upper level lies in the continuum

Chapter 2

Frequency comb generators

Just after the invention of the laser it was quickly realized that the interference between beams of two different lasers exhibited a beat note¹ whose frequency f_{beat} is the difference between the two laser frequencies f_i

$$f_{\text{beat}} = f_1 - f_2. \quad (2.1)$$

These beat frequencies could be simply observed by placing a photodiode into the interference between the two lasers. However, the frequency difference between such laser could not be larger than a few 100 GHz as electronic equipment is not fast enough to detect or count higher frequencies. But as visible frequencies are about 10^4 times higher, the intervals that could be measured using this technique are relatively small compared to the optical frequencies.

2.1 Combs - Bridging large frequency gaps

A method to increase the gap that can be measured, is to place a laser in between the two whose frequency difference should be determined and determine both beat frequencies of the two lasers to be measured against the intermediate laser. By doing this the detectable beat frequencies are only about half the total frequency difference. Still, the total gap is given by the sum of the two beats. This method could of course be extended to larger and larger gaps if a sufficient number of intermediate oscillators is added to the system. Realistically this route can not be taken as, for 1 nm in wavelength (in the visible domain) to be bridged, 10 lasers would already be necessary and the system becomes really cumbersome.

It is well known that a periodically modulated single frequency signal acquires sidebands that are spaced integer multiples of the modulation frequency apart from the original (carrier) frequency. This can also very quickly be seen mathematically. Let $E_0(t)$ be a single frequency carrier² at ω_0

$$E_0(t) = E_0 e^{i\omega_0 t} \quad (2.2)$$

¹just as in acoustics where a beat is heard if two violin strings are simultaneously played that have a slightly different tuning.

²For convenience only the positive frequency components are written down. To obtain a real physical quantity always add the complex conjugate.

Otherwise there are also other tricks like changing the modulation frequency and tracking the beat frequency as a function of it. There is no uncertainty associated with determining the mode number if it is done sufficiently careful as both mode number and sign are discrete quantities and a failure to determining them cause a finite error in the determined frequency that can be detected. In this way, frequency gaps much larger than the modulation frequency can be determined, the limit being given by the sideband farthest away from the carrier (having useable power).

Extremely broadband frequency comb generators based on harmonic phase modulation have been constructed by Kourogi et al. (1995). For such a modulator, the modulation function takes the form

$$A(t) = e^{im \sin(\omega_r t)} \quad (2.6)$$

for which the Fourier coefficients are

$$\hat{A}_n = J_n(m), \quad (2.7)$$

where J_n is the n^{th} order Bessel function of the first kind. These quickly drop to zero as n becomes larger than m , which means that the largest possible modulation index m is desirable. The most distant sideband is then $m\omega_r$ away from the carrier. For achieving the highest m while keeping the modulation frequency high too, Kourogi et al. placed their electrooptic phase modulator inside a high finesse optical resonator, whose free spectral range was matched to the modulation frequency, so that for the stored light the modulation added up in phase round trip after round trip in the resonator and comb widths of more than 10 THz could be achieved, finally limited by dispersion in the resonator. The achieved modulation index in these devices was on the order of one, but the useable bandwidth in this work was not defined by a 3dB criterion as in the above considerations but by the requirement that the generated sideband had a prescribed signal to noise ratio sufficient for beat detection.

2.2 Femtosecond lasers as comb generators

Another type of comb generator that can provide in excess of 50 THz of bandwidth directly from a laser oscillator without the need for active modulation are so-called mode-locked lasers. In a mode-locked laser, a pulse of very short duration is circulating in the laser resonator. Each time this pulse hits the output coupler mirror a copy of it is released from the laser resonator. In steady state operation (i.e. some time after the laser has been started and all the "turn on" transients have decayed), the emitted pulse train will have a perfectly periodic amplitude envelope $A(t)$ as in (2.4) with a period determined by the laser resonator round trip time T . The Fourier components \hat{A}_n will have non-negligible magnitude up to frequencies corresponding to the inverse pulse duration, which for modern Ti:Sapphire based laser systems can reach down to 5 fs, so that the corresponding frequency comb may have a bandwidth of around 200 THz. The carrier frequency (or center frequency⁴) of such lasers is around 375 THz. The spectrum of such a frequency comb

⁴As there is no unique definition of the carrier frequency for such combs because they don't start with a single frequency source and the spectrum is so broad and may be asymmetric that it is impossible to define a carrier frequency in a sensible way.

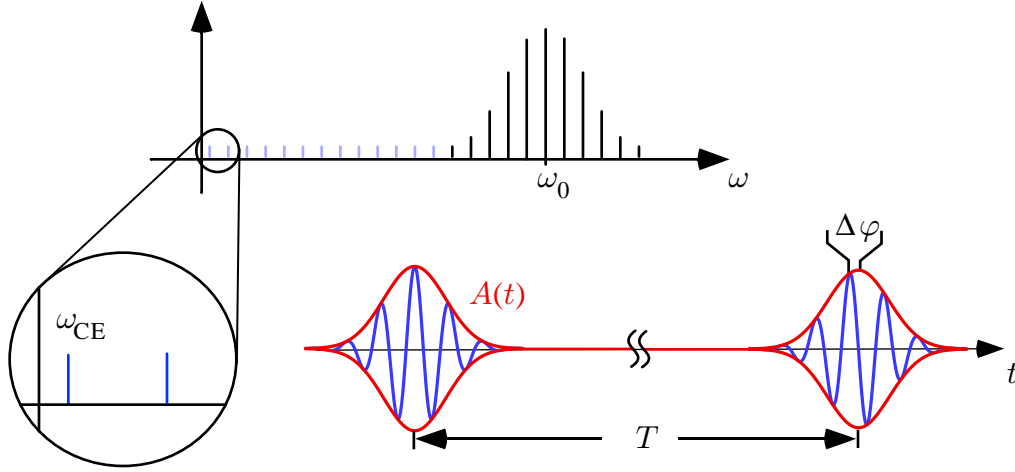


Figure 2.2: Frequency comb emitted from a mode-locked laser and the corresponding time domain picture. The frequency comb has a center mode at ω_0 . Extending the comb to zero yields ω_{CE} . The phase shift of the carrier wave with respect to the envelope from one pulse to the next is given by $T\omega_{CE} = \Delta\phi$.

contains frequencies, according to (2.4)

$$\omega_n = n\omega_r + \omega_0 = n'\omega_r + \omega_{CE} \quad (2.8)$$

where the second equality is obtained by absorbing integer multiples of repetition frequency ω_r contained in ω_0 into the first term and an appropriate renumbering (see figure 2.2). It is easy to see that $T\omega_{CE} = \Delta\phi_{CE}$ is the phase shift of the carrier wave with respect to the pulse envelope from one pulse to the next.

The bandwidth of such a comb approaches the center frequency in magnitude. Therefore it is possible to count the gap between a frequency ω and its second harmonic 2ω using such a comb generator. But because

$$\omega = 2\omega - \omega \quad (2.9)$$

the frequency itself can be counted. Therefore with the trick depicted in figure 2.3, where the second harmonic of a comb mode on the low frequency end of the comb is compared to the nearest comb mode on the high frequency end results in a radio frequency, which together with the repetition frequency is sufficient to completely determine every (optical!) mode frequency of the comb (up to an integer and a sign) via (2.8). The unknown sign of the carrier envelope frequency ω_{CE} may be found by varying the repetition rate only and determining the sign of the change of ω_{CE} .

A prerequisite for this trick to work obviously is that there actually is a mode of sufficient power close to the doubled mode frequency. As may be recalled from music, the interval between a tone at a certain frequency and its double frequency is called an octave. Therefore a frequency comb fulfilling the prerequisite for the above trick was termed an octave spanning frequency comb. Nowadays mode-locked laser sources are available that provide octave spanning spectra right out of the box (Fuji et al. 2005, Fortier et al. 2003), but if this is not the case a conceptually

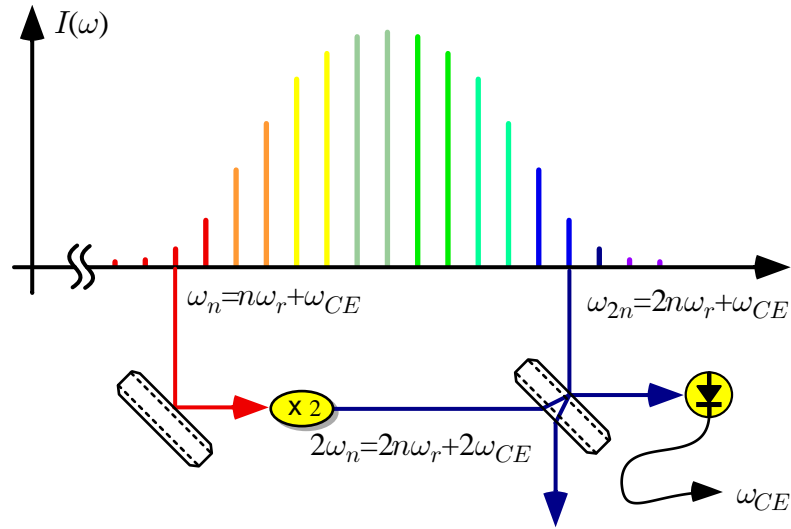


Figure 2.3: Self-referencing technique. A mode from the low frequency side of the comb is frequency doubled and compared to a mode from the high frequency end. Like this the absolute frequency of the low frequency mode, and therefore all modes can be determined via two radio frequencies ω_r and ω_{CE} and a large integer n .

simple yet powerful trick can be applied to achieve an octave of bandwidth. As was explained in the previous section, periodic modulation of a signal adds sidebands to the existing spectrum at a spacing equal to the modulation frequency. The optical Kerr effect is a nonlinear effect where the refractive index of a dielectric medium depends on the intensity of the light in the medium so that

$$n = n_0 + n_2 I(t), \quad (2.10)$$

where n_0 is the linear refractive index, $I(t)$ the intensity of the electromagnetic wave and n_2 is the Kerr coefficient. Now the intensity of the pulse train changes periodically with the repetition frequency ω_r of the pulse train and therefore, if it is travelling in a Kerr medium, it will phase modulate itself, extending the frequency comb without changing the structure (2.8). If the pulse train travels a large distance with high peak intensity (e.g. small mode diameter) and large intensity contrast (short pulse) in such a Kerr medium, this can add so many sidebands that the resulting comb spans an entire octave. The invention of special microstructured fibers enabled such a continuum generation even for mode-locked lasers that run at a gigahertz repetition rate. These fibers have a core diameter that is smaller than in standard single mode fibers, which is achieved by essentially using air as the cladding material, and thereby reaching a very large index contrast. As a result the area of the guided optical mode is much smaller than in a standard single mode fiber. Additionally, these fibers can be designed such that the dispersion for pulses propagating in the fibers is nearly zero so that the highest peak power can be maintained for a relatively long propagation length. Figure 2.4 shows the effect of such a fiber on the spectrum of a mode-locked fs-laser frequency comb with a repetition rate of 800 MHz with an initial bandwidth of about 50 THz being broadened to over 500 THz, spanning the octave between

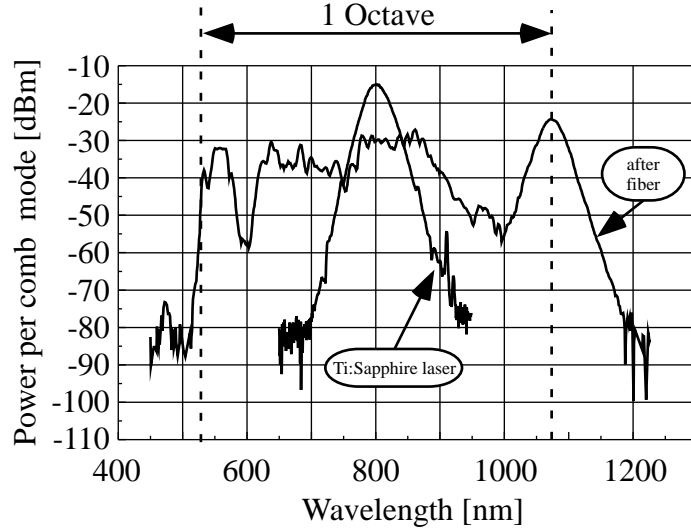


Figure 2.4: Spectrum of a Ti:Sapphire fs-laser before and after broadening it using the self phase modulation effect in a special microstructure fiber. The modes of the frequency comb are not resolved. The band width of the spectrum increases by about a factor of 10. The resulting spectrum spans the octave between 532 nm and 1064 nm. $\text{dBm} := 10 \log_{10}(P/1\text{mW})$, P power per mode.

532 nm and 1064 nm.

A schematic of a real frequency comb setup is shown in figure 2.5. Instead of selecting a single mode to do the selfreferencing, a (relatively) narrow band section can be selected by the frequency doubling crystal phase-matching conditions. In this way all the phase-matched modes are mixed in a sum frequency process instead of doubling only one mode. The generated modes still have twice the carrier envelope frequency, and an interference with the blue modes of the comb still exhibits the carrier envelope frequency ω_{CE} . Care has to be taken however that all these beat notes add up in phase, i.e. that the frequency doubled pulse arrives simultaneously on the beamsplitter with the blue part of the original pulse. Therefore an adjustable delay line is used for the blue part of the original comb.

Now that every comb mode can be assigned an exact frequency⁵, any unknown laser frequency ω_l within the spectral range of the comb can be counted directly by only counting the (radio frequency) beat signal ω_b , between the laser and the nearest by mode of the comb. When the mode number n and the sign of the beat signal is determined, the laser frequency may be calculated via

$$\omega_l = n\omega_r + \omega_{CE} \pm \omega_b, \quad (2.11)$$

making optical frequency measurements an (almost) trivial task. No limit of the achievable accuracy of this optical counting technique has been found so far. Upper limits on the error of a frequency measurement using frequency comb technique have been determined to be smaller

⁵in terms of the radio frequencies, ω_r and ω_{CE} , which may be counted or controlled electronically.

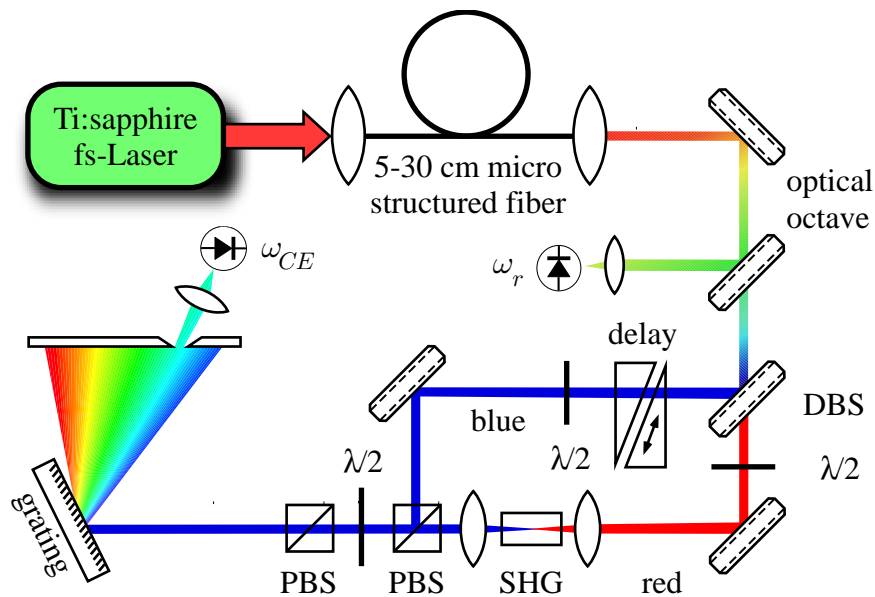


Figure 2.5: f-2f interferometer setup. The microstructure fiber broadens the comb to an optical octave. The output is split into a red frequency part and a blue part at a dichroic beam splitter (DBS). The red part is frequency doubled (SHG) while the blue part is delayed such that when the doubled part and the original blue part are superimposed on the next beam splitter, both pulses arrive simultaneously. In this way, all the beat signals from the different components of the combs leading to the same beat frequency interfere constructively. Filtering away the modes that don't contribute to a beat signal with a grating and a slit improves signal to noise ratio. $\lambda/2$: half wave plate, PBS: Polarizing beamsplitter, SHG: second harmonic generation

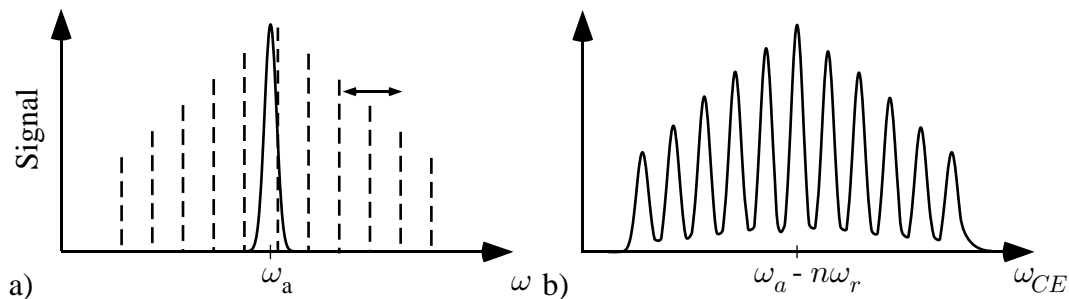


Figure 2.6: Linear (single photon) spectroscopy with a comb. Panel a) shows the response of the atom to a single frequency (solid) and the comb spectrum (dashed) that can be shifted by tuning the offset frequency. Panel b) gives the atomic response as a function of the carrier envelope frequency. For a linear response of the atom this spectrum is just the convolution of atom response and comb spectrum.

than 10^{-15} (Holzwarth et al. 2000, Diddams et al. 2002) and some properties of the comb have been tested by Zimmermann et al. (2004) to be more accurate than one part in 10^{20} .

2.3 Spectroscopy with frequency combs

Frequency combs not only provide a method to directly count optical frequencies and provide and optical clockwork for all optical clocks that can be expected to outperform radio frequency primary time standards in the very near future. They also in some sense combine the best of ultrafast physics and precise narrow band spectroscopy. The modes of a frequency comb can be made similarly narrow as the single mode of a stabilized single frequency laser source using essentially the same techniques (Jones and Diels 2001) so that in principle each mode of the comb can be used for high resolution spectroscopy. But the comb provides up to 10^6 of those simultaneously so that one can dream of taking survey spectra across the entire optical domain with a resolution and simultaneous accuracy on the order of 10^{-15} in the twinkling of an eye. This section discusses some of the possibilities.

2.3.1 Single mode

The most obvious spectroscopic application of a frequency comb is to use a single mode of it to excite a narrow band atomic transition as was done by Gerginov et al. (2005). The idea is very simple: place an atomic absorber into the beam of a mode-locked laser and record the spectroscopic signal (like fluorescence or absorption) as a function of carrier envelope frequency ω_{CE} while keeping the repetition rate ω_r fixed. As shown in figure 2.6 the observable atomic response is just the convolution of the comb spectrum and the atomic response. This already shows some restrictions of the method:

1. If the width of the atomic response is on the order of or larger than the spacing between

the comb modes, the resulting signal will have little or no structure and no frequency can be determined.

2. The position of the resonance ω_a has to be known beforehand to better than half a comb spacing. Otherwise the mode number has to be determined by measuring at different repetition rates also.
3. If there are many resonances within the frequency comb spectral range, it may become hard to identify each of them as all of them will appear in every ω_r copy of the signal and a deconvolution may become impossible as the driving field (the Fourier transform of the spectrum) is zero most of the time.

Another point that has to be kept in mind, is that the total output power of the frequency comb is distributed among up to 10^6 individual modes and at most one single mode can drive the resonance of the atom so that it may become hard to detect a signal due to low transition rates. However, if the atom numbers in the sample is sufficiently high and good detection techniques are employed this method still works, as demonstrated by Gerginov et al. (2005). In that work, as opposed to scanning the carrier envelope frequency, the repetition rate was scanned, while keeping the former fixed. This makes the tuning mechanism easier to implement and avoids some problems associated with the carrier envelope frequency becoming zero or $\omega_r/2$.

2.3.2 Two-photon spectroscopy

If two-photon transitions are probed with a frequency comb some of the prerequisites for frequency comb spectroscopy can be more easily fulfilled. First, if a transition is two-photon allowed, parity and angular momentum conservation immediately forbid a direct single photon decay to the ground state. Therefore, if there are no other decay channels, the excited state is typically very long lived and the transition has a small natural linewidth. Additionally, if the transition is excited with two counter-propagating photons of the same frequency, the first-order Doppler shift due to the motion of the atom is cancelled, and therefore the observed linewidth can be close to the natural one, avoiding the problem of smearing the atomic response across several comb modes.

It was also quickly realized that (for an atom at rest) if a pair of modes from the frequency comb was resonant with the atomic two photon resonance at frequency ω_a , i.e.

$$\omega_a = (n\omega_r + \omega_{CE}) + (m\omega_r + \omega_{CE}) = (n + m)\omega_r + 2\omega_{CE}, \quad (2.12)$$

the same holds true for a pair of modes, one k modes to the left and the other k modes to the right of the original modes

$$\omega_a = ((n + k)\omega_r + \omega_{CE}) + ((m - k)\omega_r + \omega_{CE}). \quad (2.13)$$

Hence, the entire frequency comb power contributes (see figure 2.7) to driving the two-photon transition if the resonance condition (2.12) is fulfilled. It was Baklanov and Chebotayev (1977)

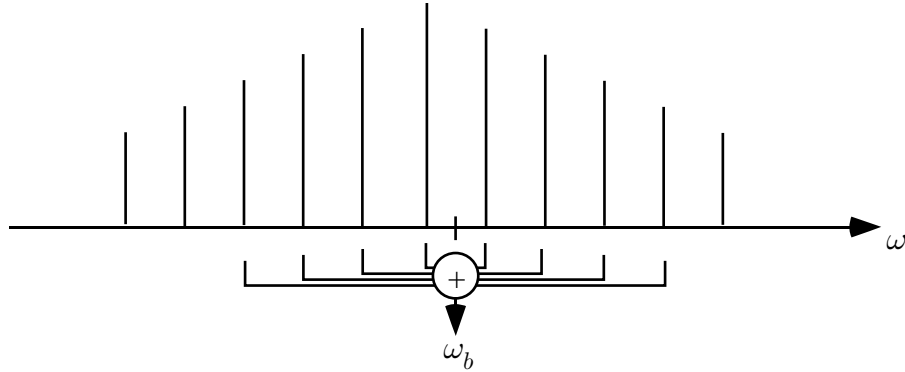


Figure 2.7: Pairs of comb modes can add to the same transition frequency ω_b of a two-photon transition. Due to the perfect periodicity of the comb, its entire spectrum contributes to driving a narrowband two-photon transition.

who pointed out that if the relative phases of all these modes are chosen right so that the contributions from different mode pairs add up in phase⁶, the transition rate for the two-photon transition is equal to the transition rate obtained with a single frequency laser with the same average power. Depending on $n + m$ being even or odd $\omega_{CE} + (n + m)\omega_r/2$ is one of the comb modes (even) or just in the middle between two comb modes (odd). Therefore the resonance condition reappears after a scan of the frequency comb by $\omega_r/2$ only, in contrast to the situation in 2.3.1 where spectra repeated after a scan twice as large.

Experimentally, such two-photon comb spectroscopy has been demonstrated by Eckstein in 1978 already using an actively mode-locked dye laser. In that work the 3s-4d and the 3s-5s two-photon transitions in sodium were investigated in a vapor cell. Of course at that time no octave spanning frequency combs were available, and absolute frequency measurements could not be performed like this. But the about 1 THz wide, mode-locked dye lasers available at that time still enabled the determination of frequency differences as large as hundreds of GHz. A main limitation for these experiments was the relatively high temperature of the sample. The Doppler effect can *not* be completely cancelled in this frequency comb two-photon spectroscopy, even if a standing wave arrangement is used, as the photons in the frequency comb do not all have the same frequency. Therefore the first order Doppler shift for counter-propagating two-photon absorption is

$$\Delta\omega_{Doppler} = \frac{v}{c}(\omega_1 - \omega_2) = v\Delta\omega \quad (2.14)$$

with v being the projection of the atoms velocity onto the beam axis and ω_i being the frequencies of the two photons. Therefore, in a worst case estimate, the Doppler width of the signal is given by

$$\Delta\omega_{Doppler} = \frac{\sqrt{\langle v^2 \rangle}}{c} \Delta\omega. \quad (2.15)$$

Here $\Delta\omega$ is the bandwidth of the comb and it was assumed that only modes from the wings of

⁶which in the simplest case holds true if the phases are all zero (at some time), i.e. the pulses in the pulse train are Fourier limited.

the comb spectrum contribute. Compared to the width of the signal in a collinear (not Doppler free) arrangement the width in (2.15) is reduced by the relative bandwidth of the comb $\Delta\omega/\omega$

There are essentially two ways to fix this. One is to cool the sample, reducing the full Doppler width, the other is to reduce the comb bandwidth. An experiment that uses the first option was performed by Snadden et al. (1996), which investigated the 5s-5d and 5s-7s transitions in atomic rubidium vapor that was cooled in a magneto-optical trap and excited by a mode-locked Ti:Sapphire femtosecond laser. In this experiment the sample was cold enough to observe nearly natural linewidths of the transitions under investigation. First results on absolute optical frequency measurements using the same technique were obtained by Marian et al. (2004) also on laser cooled rubidium.

Also (almost⁷) absolute frequency determination was performed by Witte et al. (2005), who first demonstrated a big advantage of frequency comb spectroscopy: because the frequency comb is simultaneously a train of ultrashort pulses, extremely high electric fields are available for short periods of time. This fact facilitates the nonlinear conversion of the frequency comb spectrum to higher order harmonics (4th order in this case).

2.3.3 Fourier transform spectrometry

It is a well known fact that the Fourier transform of the first order-autocorrelation of any electric field yields the electric field's spectrum. This fact is widely used in Fourier transform spectrometers. These devices (which work in principle in any spectral domain) are essentially Michelson interferometers that are lit by the (broadband) radiation whose spectrum is to be determined. An interference pattern is recorded at the output port of the interferometer as a function of length difference between the two interferometer arms. The Fourier transform of the resulting function yields the spectrum of the radiation. One of the problems with these kind of devices that limits the accuracy, is the determination of the arm length difference, which is typically measured interferometrically using an auxiliary laser, essentially performing a wavelength measurement.

Of course in reading the introduction of this work, the reader has learned his lesson: Why measure a length were a frequency could be measured. To demonstrate this we (Keilmann et al. 2004) have performed a pioneering experiment in our laboratories, where a new time domain Fourier transform spectrometer in the mid infrared spectral region was demonstrated. The basic idea is really simple: Two frequency combs having identical carrier envelope frequency ω_{CE} but different repetition rates ω_{r1} and ω_{r2} respectively, are made to interfere and the interference is recorded with a photo detector. If the difference between the two repetition rates is sufficiently small, e.g.

$$\left| \frac{2(\omega_{r1} - \omega_{r2})}{\omega_{r1} + \omega_{r2}} \right| \ll \frac{1}{n_0}, \quad (2.16)$$

n_0 being the typical (center) mode number of the comb, the beat signals that appear at frequencies below half the repetition rate are beats between modes of the two combs with identical mode number, i.e.

$$\omega_{beat,n} = n\omega_{r1} + \omega_{CE} - n\omega_{r2} - \omega_{CE} = n\Delta\omega_r, \quad (2.17)$$

⁷they failed to determine the modenummer without doubt

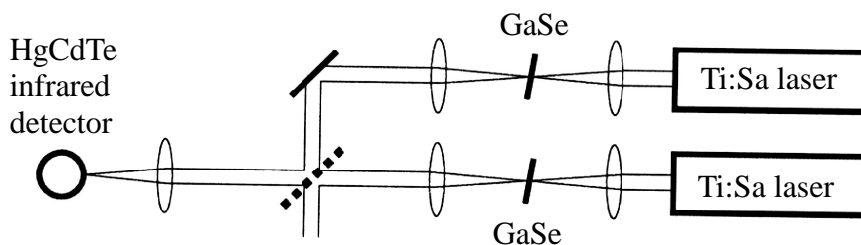


Figure 2.8: Two mode locked femtosecond lasers are focused into two GaSe crystals where optical rectification generates two offset free frequency combs in the mid infrared region around 1000 cm^{-1} . These two beams are combined on a beamsplitter and the resulting timedomain interferogram is recorded on a HgCdTe photo detector.

with $\Delta\omega_r = \omega_{r1} - \omega_{r2}$ and the amplitude of that signal being proportional to the product of the amplitudes of the two corresponding optical frequencies. This means that in this arrangement there is a close correspondence between the optical spectrum and the radiofrequency spectrum via

$$I_{opt}(\omega) \mapsto I_{rf} \left(\frac{2\Delta\omega_r}{(\omega_{r1} + \omega_{r2})} (\omega - \omega_{CE}) \right). \quad (2.18)$$

Here we assigned the average of the two optical frequencies to their beat frequency.

In the experiment described in more detail in the article (Keilmann et al. 2004), two offset free mid-infrared frequency combs were generated by rectification (i.e. difference frequency generation) of the output of two near infrared Ti:Sapphire mode locked femtosecond lasers in two GaSe-crystals as shown in figure 2.8. The two driving lasers had a repetition rate of 87 MHz with a difference of nominal $\Delta\omega_r = 2\text{ Hz}$. The resulting mid infrared beams were colimated and superimposed on a ZnSe beamcombiner. The resulting interferogram was recorded on a HgCdTe photo detector.

A fourier transformation of the time domain interferogram yields the detected mid infrared spectrum, which is checked by placing molecular trichlorethylene gas with a strong absorbtion band at 940 cm^{-1} into the mid infrared beam. The resulting spectrum clearly exhibits a pronounced dip at that frequency. Figure 2.9 summarizes the result.

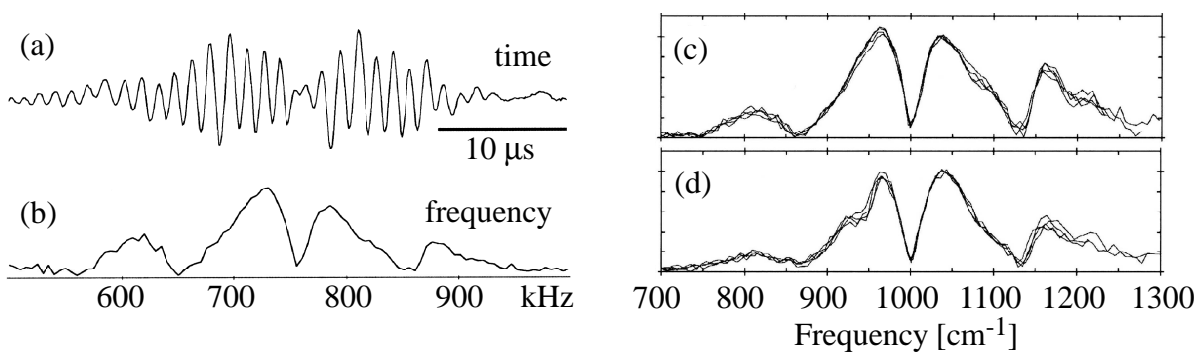


Figure 2.9: (a) time domain photocurrent recorded by a sampling oscilloscope. (b) power spectrum obtained by taking the fourier transform of such a trace. (c) infrared spectrum obtained from such a power spectrum using (2.18) and (d) spectrum obtained, when placing trichloroethylene into the beam path. The strong absorption band near 930 cm^{-1} is clearly observed.

Chapter 3

Theoretical aspects of extreme ultraviolet frequency comb generation

Extreme ultraviolet (XUV) lasers at the time of writing are in a similar situation as visible lasers in the 1960's. They are of little use for high resolution spectroscopy because of relatively broad-band emission. In the visible, it was not until 1972 that the first widely tuneable single mode laser appeared. In this chapter I present our approach to creating a quasi-continuous XUV source that is in principle suitable for high resolution spectroscopy.

There is hardly any gain medium available that supports the lasing in the XUV spectral range and it is almost impossible to create strong feedback on such a gain medium due to the lack of high reflectance mirrors in that wavelength range. Still, very impressive performance can be achieved using so-called free electron lasers (FEL). In these devices a relativistic electron beam is passed through a periodic alternating magnetic field array (a so-called undulator). The electrons are accelerated perpendicular to the propagation direction due to the Lorenz force and emit broadband synchrotron radiation into a narrow cone around the forward direction due to their relativistic velocities. If the deflection angle in the undulator is on the order of the cone angle, so that the emitted radiation overlaps at any time with the electron beam, a phase-matching condition for constructive interference of the generated light is established by the requirement that the generated (faster) electric field has traveled an integer number of cycles with respect to the electron's center of mass motion during one undulator period of the electron. Therefore the emission wavelength of an FEL can be tuned by changing the undulator period and/or the electron velocity. If the emitted radiation power is high enough, back action of the generated field onto the generating electron bunch will become important. This back action tends to divide the electron bunch into smaller pieces (so-called microbunches with wavelength separation) so that more and more electrons will radiate in phase with the local electric field, amplifying the existing field exponentially. This process will stop, as all the electrons are collected into the microbunches and the gain curve saturates. If there is no additional feedback mechanism, every electron bunch follows this process starting out from zero field. This mode of operation is called "self amplified spontaneous emission"(SASE). The transversal mode profile of such a SASE FEL is nearly transform (diffraction) limited but the temporal/spectral properties are less favorable when considering high-resolution spectroscopy. As every electron bunch starts out from vacuum

fluctuations (synchrotron radiation) the phase of the first photon generated by the bunch has a random phase. Additionally, the saturation length of such a system is typically too short to establish phase coherence across the whole bunch, which is why the spectrum of a single pulse is far from being transform limited¹.

Another possibility to create laser-like radiation in the XUV and soft X-ray spectral region is to convert available highly coherent visible and near infrared (NIR) laser sources using nonlinear conversion processes. There, the nonlinear response of dielectric media is utilized, to create harmonics and/or sum and difference frequencies of the laser's frequency (frequencies). In the low field limit, assuming purely elastic photon scattering, the atomic polarization in a dielectric medium can be expanded in a Taylor series in $E(t)^2$

$$P(t) = \int_{-\infty}^t \chi_1(t - \tau)E(\tau)d\tau + \int_{-\infty}^t \int_{-\infty}^t \chi_2(t - \tau, t - \tau')E(\tau)E(\tau')d\tau d\tau' + \dots, \quad (3.1)$$

where the (nonlinear) susceptibilities $\chi_n(t)$ are assumed to be zero for times $t < 0$ as required by causality. The Fourier transform of (3.1) can be written as

$$\hat{P}(\omega) = \hat{\chi}_1(\omega)\hat{E}(\omega)d\omega + \int \hat{\chi}_2(\omega', \omega - \omega')\hat{E}(\omega')\hat{E}(\omega - \omega')d\omega' + \dots, \quad (3.2)$$

where $\hat{E}(\omega)$, $\hat{P}(\omega)$ and $\hat{\chi}_n(\omega)$ are the Fourier transforms of the electric field, the polarization and the nonlinear susceptibilities respectively. From this it can immediately be seen that the spectrum of the polarization contains all possible sums and differences of frequencies of the driving field. Specifically, if the driving field only contains a single frequency, integer multiples of this driving frequency are created. Obviously these new frequency components in the polarization are radiated away so that these new frequency components are available in the electromagnetic field too. As Boyd (2003) points out, the magnitude of the nonlinear susceptibility χ_n for nonresonant drive can be estimated by

$$\chi_n \approx \frac{\chi_1}{E_a^n}, \quad (3.3)$$

with E_a being the electric field seen by the participating electrons in the ground state of the atom. For electric fields much smaller than E_a , the magnitude of nonlinear polarization at n times the driving frequency will then be dominated by the lowest order contribution to this n^{th} harmonic³ and the harmonic yield will decrease exponentially with harmonic order as

$$\hat{P}(n\omega_0) \propto \left(\frac{\hat{E}(\omega_0)}{E_a} \right)^n \quad (3.4)$$

For a driving field amplitude approaching E_a , this lowest order approximation no longer holds, and for $E(\omega_0) > E_a$ the Taylor series fails to converge completely. In that case a perturbative ansatz to calculate the nonlinear response and the generated radiation will be no longer valid, and different methods are required.

¹for an overview see Materlik and Tschentscher (2001).

²see for example in Boyd (2003).

³The $(n + 2k)^{\text{th}}$ order susceptibilities can contribute to the same frequency as $\omega_n = n\omega_0 = (n + k)\omega_0 - k\omega_0$ is contained in the $n + 2k^{\text{th}}$ order polarization spectrum.

From the experimental point of view, first observations of a deviation from the exponential falloff of laser harmonics of high order were reported by McPherson et al. (1987) and Ferray et al. (1988). They observed that, when focusing intense laser pulses into a dilute noble gas target, after a steep exponential falloff of power with harmonic order, an extended region (plateau) of essentially constant intensity per harmonic is generated up to a maximum energy, at which the efficiency sharply cuts off. This observation triggered many experiments looking at spectral spatial and temporal characteristics of such a source, as it promised to be a relatively small "tabletop" source for highly coherent high energy photons.

It is important to notice, that if the nonlinear properties of the generating medium are time independent⁴, that is, there are no external degrees of freedom coupling to the system (like spontaneous photons from excited states of the medium, ionization or scattering with phonons) then the coherence (i.e. phase and amplitude stability) of the polarization depends on the coherence properties of the driving field only, so that it is expected that the coherence of the driving field will be transferred to the coherence of the generated field. From this point of view, high harmonic generation can provide a way to generate (quasi)continuous radiation in the XUV, provided a source of sufficiently high repetition rate can be built.

This chapter presents a method for generating XUV radiation from a mode-locked laser source with a repetition rate three orders of magnitude higher than any other known (Lindner et al. 2003) tabletop ultrafast laser based XUV source at the time of writing. It is organized as follows.

In section 3.1 the theory of high order harmonic generation will be reviewed, to get an overview of what properties of the driving field are necessary to obtain XUV and/or soft X-ray photons with a high efficiency.

Section 3.2 will present theoretical considerations, regarding high finesse optical resonators suitable for ultrafast lasers. Such a resonator, in the presented method for generating XUV radiation with high repetition rate, is crucial for maintaining a sufficiently high laser intensity to efficiently generate XUV photons.

3.1 High harmonic generation

If a dielectric medium is driven by extremely high intensities, so that the driving electric field is comparable to the atomic electric field seen by its valence electrons, the spectrum of generated harmonic radiation does not exhibit the usual exponential falloff of generated power vs. harmonic order as expected from lowest-order perturbation theory. Instead, an extended region of harmonics of equal power is observed (plateau), that quickly cuts off at a certain photon energy. This behavior was first observed by Ferray et al. (1988) and McPherson et al. (1987). In noble gases, the required intensity to observe such a phenomenon lies above 10^{13} W/cm².

As mentioned in the previous section, this behavior can not be explained within a perturbative approach to nonlinear frequency conversion, as the Taylor expansion (around zero driving field) of the nonlinear response fails to converge at these high intensities. To overcome this difficulty,

⁴as assumed in eq. (3.1), which depends on the driving field only and not explicitly on time

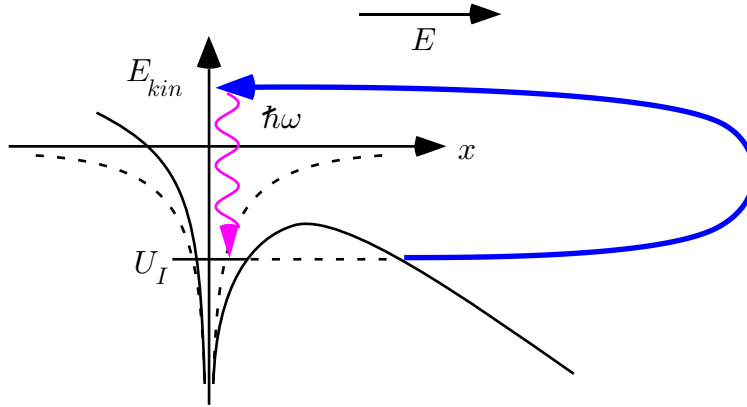


Figure 3.1: Three step model of HHG. The atomic potential plus the potential of the driving field make a tunnel barrier. Once the electron has tunneled through this barrier in the first step, it is accelerated, in a second step, in the alternating driving field and may return to the parent ion with a kinetic energy E_{kin} . If it recombines, in the last step, into the ground state, it emits a photon of energy $\hbar\omega = E_{kin} + U_i$, $-U_i$ being the binding energy of the electron.

a different approach to understand the nonlinear response of a medium under these conditions is required. In this section a brief overview of the theoretical model describing the high field nonlinear response of dielectric media will be given.

3.1.1 The simple man's model

The "three step"- or "simple man's model" of high order harmonic generation which will be discussed now was put forward by Corkum (1993) and Kulander et al. (1993). It provides a simple and intuitive approach to the phenomenon of high order harmonic generation and some of its properties. Later this model was justified by the quantum mechanical considerations of Lewenstein et al. (1994) which are outlined in appendix A. According to this three step model the electron participating in the process first tunnels from the atomic ground state through the barrier formed by the Coulomb potential and the laser field (see figure 3.1).

After this step, where the electron appears in the continuum at the position of the parent ion ($x \approx 0, \dot{x} = 0$) and is accelerated by the laser field. This motion can essentially be treated classically and is (for sufficiently high field amplitude) dominated by the alternating field of the laser which will induce an oscillating motion of the electron. Under certain conditions the electron may return to the vicinity of the parent ion and, in the third step, recombine to the ground state. If it does so with a kinetic energy E_{kin} , a photon of energy $E_{kin} + U_I$, where U_I is the ionization potential of the atom, is emitted. It is quite straightforward to see that it can only return to the parent ion and recombine if the driving laser field is linearly polarized. Therefore, from now on the laser field will be assumed to be linearly polarized along the x-direction

$$\mathbf{E}(t) = \mathbf{e}_x E_0 \cos(\omega t), \quad (3.5)$$

where \mathbf{e}_x is the unit vector in x-direction.

First step: Ionization

The ionization rate (neglecting ground state depletion) for an atom in a static electric field may be calculated analytically. In the classic book of Landau and Lifschitz (1966) this rate may be found to be

$$\Gamma \propto \frac{E_0}{U_I^{5/2}} \exp\left(-\frac{4\sqrt{2m}U_I^{3/2}}{3e\hbar E_0}\right). \quad (3.6)$$

This can be generalized to varying fields, which has been done by Keldysh (1965). Another result was given by Ammosov, Delone and Krainov (1986) and is known as the ADK rate. Both these approaches, in the high field limit, give results similar to (3.6), only with different prefactors (which depend weakly on E) to the exponential. The quasistatic approximation used in both of these calculations assumes that the tunneling time of the electron through the Coulomb barrier are short compared to an optical cycle, which is fulfilled if the so-called Keldysh parameter

$$\gamma = \sqrt{\frac{U_I}{2U_p}} \quad (3.7)$$

is smaller than one. Here U_p is the ponderomotive energy, the average kinetic energy, of an electron in a harmonic electric field, which is given by

$$U_p = \frac{e^2 E_0^2}{4\omega^2 m_e}. \quad (3.8)$$

The electric field amplitude E_0 is related to the intensity of the laser beam by

$$I = \frac{c\epsilon_0}{2} E_0^2. \quad (3.9)$$

For a Keldysh parameter γ much larger than one, the field ionization rate is dominated by multiphoton absorption, which has a different power scaling and is also given in the work of Keldysh (1965). Experimentally one typically deals with an intermediate regime of γ , as for example the intensity where γ is about one is found for most noble gases to be around 10^{14} W/cm². For this regime an expression was derived recently by Yudin and Ivanov (2001). In the high field/low frequency limit $\gamma < 1$ this result reproduced the quasistatic limit, while in the multiphoton limit, the ionization probability is no longer zero even at zero electric field. For extremely high electric fields the Coulomb barrier will be lower than the ground state energy. Threshold intensities for Ne, Ar and Kr for example are approximately 10^{15} W/cm², 4×10^{14} W/cm² and 3×10^{14} W/cm² respectively. Obviously at higher intensities any model involving tunnel ionization must fail as there is no longer a barrier to overcome. For such intensities different approaches to the problem are required (for example Bauer and Mulser 1999, and references therein).

Second step: Free evolution

It is well known that the canonical momentum of an electron in an electric radiation field

$$\tilde{\mathbf{p}} = \mathbf{p} - e\mathbf{A}(t) \quad (3.10)$$

is a conserved quantity (in coulomb gauge). Therefore the momentum of the electron at time t that appeared in the continuum at time t_0 with velocity $\mathbf{v}(t_0) = 0$ is simply given by

$$\mathbf{p}(t) = e(\mathbf{A}(t) - \mathbf{A}(t_0)), \quad (3.11)$$

and the electron trajectory takes the form

$$\mathbf{x}(t) = \frac{e}{m_e} \left(\int_{t_0}^t \mathbf{A}(t') dt' - \mathbf{A}(t_0)(t - t_0) \right) + \mathbf{x}_0. \quad (3.12)$$

This can be conveniently split into two terms: A linear drift motion that depends only on the vector potential $\mathbf{A}(t_0)$ at the time of ionization

$$\mathbf{x}_{\text{dr}}(t) = -\frac{e}{m_e} \mathbf{A}(t_0)(t - t_0) + \mathbf{x}_0 \quad (3.13)$$

and the driven oscillatory motion

$$\mathbf{x}_{\text{osc}}(t) = \frac{e}{m_e} \int_{t_0}^t dt' \mathbf{A}(t') \quad (3.14)$$

Third step: Recombination

The electron can only recombine (or in general interact) with the parent ion, if it returns to it. Specifically, if it is required that the electron returns to the position, were it started its journey⁵ $x(t_{\text{rec}}) = x(t_0)$ this results in the condition

$$\int_{t_0}^{t_{\text{rec}}} dt' \mathbf{A}(t') = (t_{\text{rec}} - t_0) \mathbf{A}(t_0). \quad (3.15)$$

The solution to this equation, in most circumstances, can not be given in closed form⁶. But a simple graphical method exists to determine the recombination time t_{rec} for the case of linearly polarized driving field. As shown in figure 3.2, when the oscillatory motion \mathbf{x}_{osc} is plotted versus time, the drift motion at time t_0 has the same slope as the oscillatory motion because $\dot{\mathbf{x}}_{\text{osc}}(t) = \frac{e}{m_e} \mathbf{A}(t_0) = v_{\text{dr}}$. With an appropriate offset to the drift motion, it can be made a tangent to the oscillatory motion. Then solutions to (3.15) are found at each intersection of the drift with the oscillatory motion. From these considerations it can be immediately seen that, in the case of a harmonic field, there is recombination only if the ionization takes place between a peak of the field and the following zero crossing. For later ionization times (until the next peak of opposite sign) the electron does not return to the parent ion. It can also be seen in figure 3.2 that for some trajectories the electron can return more than once. If it is not absorbed by the parent ion at the first possible instant, it may also recombine later.

Particularly important for HHG is the kinetic energy of the recombining electron as this determines the emitted photon energy via $E_\nu = E_{\text{kin}}(t_{\text{rec}}) + U_I$. Figure 3.3 shows the kinetic

⁵This condition is justified by (A.13) from the quantum mechanical derivation in appendix A.

⁶even if the field is harmonic and linearly polarized

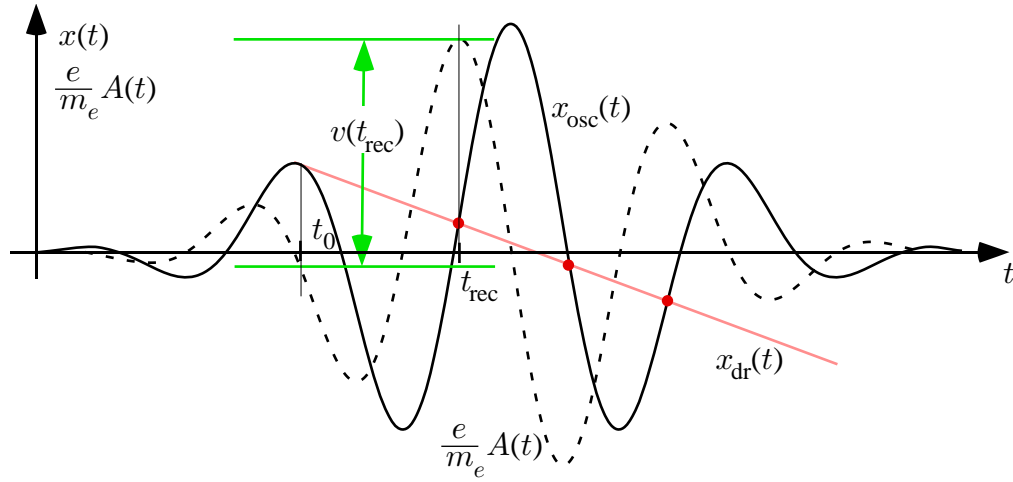


Figure 3.2: Graphical determination of the recombination time and return velocity of the electron. $x(t)$ with solid and $\frac{e}{m_e}A(t)$ with a dashed line. See text for an explanation.

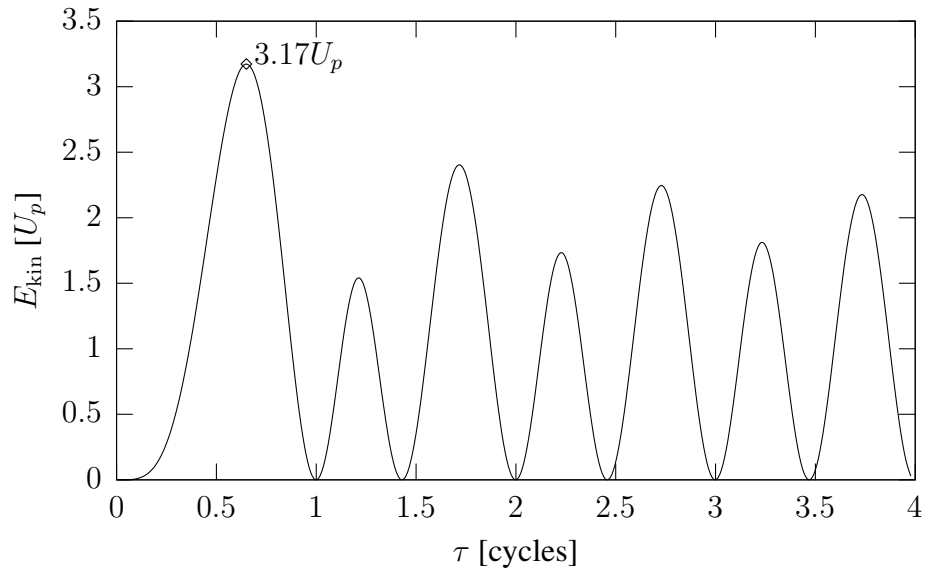


Figure 3.3: Kinetic energy of the returning electron as a function of the travel time τ . The absolute maximum of this function is found to be $3.17U_p$.

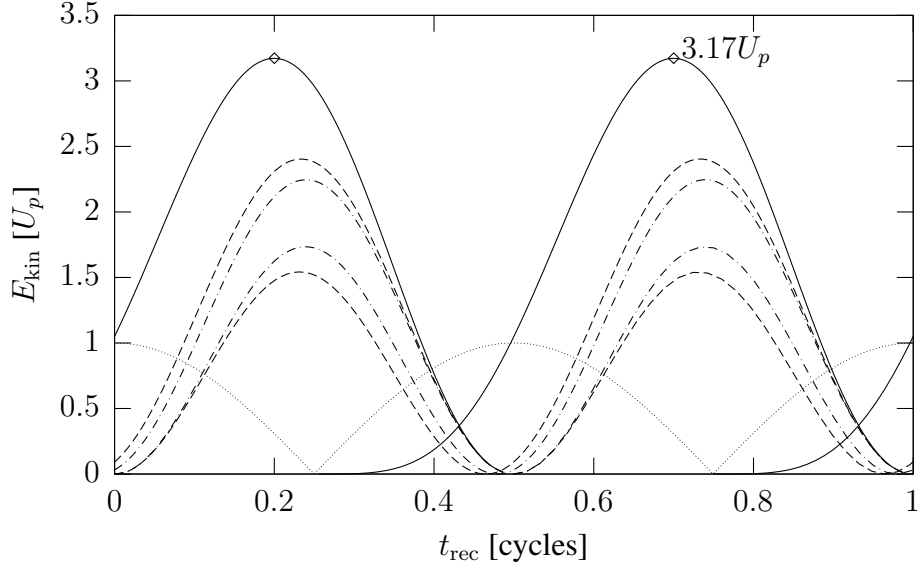


Figure 3.4: Kinetic energy of the returning electron as a function of return time for trajectories shorter than an optical cycle (solid), between one and two (dashed), and between two and three optical cycles (dash-dotted). This shows the instantaneous spectral distribution of the generated field (for a finite time window). The strongest contribution comes from the trajectories shorter than an optical cycle. The dotted line is proportional to the electric field at the time of recombination.

energy of the recombining electron as a function of travel time $\tau = t_{rec} - t_0$ for the case of a harmonic driving field. This parameter was chosen, as it uniquely (modulo half an optical period) identifies the possible trajectories that return to the parent ion. The absolute maximum of this function is found to be $3.17U_p$ which determines the highest frequency found in the atomic polarization. This is the well known cutoff frequency that is given by

$$\hbar\omega_{\text{cutoff}} = 3.17U_p + U_I. \quad (3.16)$$

It is also very instructive to look at the kinetic energy of the returning electron as a function of return time t_{rec} . This is shown in figure 3.4. This gives a hint of how the instantaneous spectral distribution⁷ of the dipole moment looks. It will have maxima at $\hbar\omega = E_{kin}(t_{rec}) + U_I$ for each of these trajectories. Note however that the contribution of trajectories longer than one optical cycle are strongly suppressed⁸.

It is important to note that there is always more than one trajectory of the electron that returns with the same kinetic energy, contributing to the polarization component of the same frequency. To determine the polarization amplitude at this frequency it is therefore necessary to know, in

⁷i.e. The Fourier transform of the dipole moment with a moving time window centered at t_{rec} of a length shorter than an optical half cycle.

⁸This is due to the fact that the size saddle points in the quantum mechanical description of HHG (appendix A) are much smaller for longer trajectories, i.e. small $G_n(\omega)$ in (A.16).

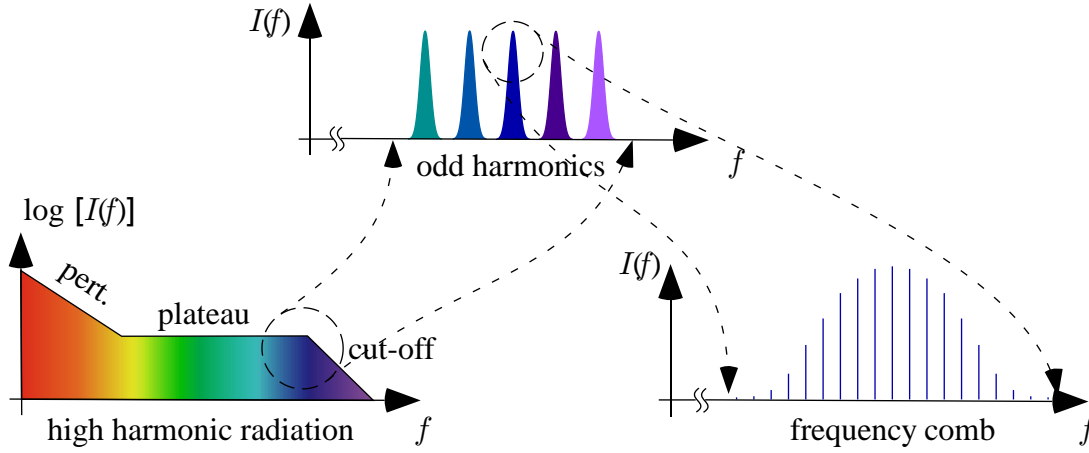


Figure 3.5: The hierarchy of the emitted harmonic spectrum. The spectrum emitted during a half cycle of the driving field is characterized by a plateau of constant intensity up to a maximum energy, the cutoff energy. Interference between emission from each half cycle of one pulse leads to a peak structure with maxima at odd multiples of the driving frequency. Interference between the pulses in the frequency comb pulse train lead to a frequency comb structure according to (A.22).

addition to the amplitudes of the contributing trajectories, the relative phase of these different contributions. Both of these quantities can not be calculated from the simple model presented here. The quantum mechanical model in appendix A.3, however allows the calculation of the phase. There it is also show that the phase of the generated radiation depends on the drive intensity, which provides a amplitude to phase coupling that has to be taken care of, when producing a coherent frequency comb in the XUV.

Putting everything together, the spectrum of the atomic polarization, with a frequency comb as the driving field, shows the characteristics depicted in figure 3.5. The spectrum emitted within one half cycle of the electric field contains all frequencies from zero up to the cutoff frequency $\hbar\omega_{max} = U_I + 3.17U_p$ and the power of all these frequency components is approximately the same (modulo interference between contributions from different classical trajectories). This is the so called plateau of HHG. For photon energies on the order of the ionization potential and below, the presented model is not valid, as the kinetic and/or potential energy of the electron is too low and neglecting the atomic potential is not a good approximation. Therefore the real spectrum has a quickly dropping shoulder for these low frequencies. Because the dipole emission repeats itself with every half cycle (with alternating sign) of the driving field this broad emission has a substructure with twice the period of the driving frequency, corresponding to the odd harmonics. These are still relatively broad due to the finite duration of the driving pulses. Finally, as is argued in appendix A.2, because the driving pulse train is a frequency comb, so is each of the resulting odd laser harmonics. The comb equation for the $2j + 1$ harmonic is

$$\omega_n(2j + 1) = n\omega_r + (2j + 1)\omega_{CE}. \quad (3.17)$$

as in (A.22). Each of these comb modes should in principle be infinitely narrow, if the modes in

the driving comb are.

3.1.2 Macroscopic response

After the discussion of the atomic response to a driving field, the next step to get the emission characteristics from a macroscopic sample, is to integrate the emission from the atoms across the generating volume with the appropriate phases due to generation and propagation and including reabsorption of the XUV light by core level electrons. This integral will again give large contributions only if the phase has a saddle point across a non-negligible volume. This condition is often referred to as the phase-matching condition.

There are three main contributions to the (spatial) phase of the generated light.

- the atomic phase (A.24) depends on intensity and is therefore a function of space and time.
- the geometrical phase (the phase shift of a Gaussian beam with respect to a plane wave)

$$\phi_{geom}(r, z) = -\arctan\left(\frac{z}{z_R}\right) + \frac{\pi r^2}{\lambda R(z)}, \quad (3.18)$$

where r and z are the radial and longitudinal coordinates, respectively, of a Gaussian beam with a focus at $z = 0$, $z_R = 1/2 \times kw_0$ is the Rayleigh length of the focus with radius w_0 , k is the wave vector and $R(z)$ is the wavefront radius of curvature.

- dispersion due to neutral atoms, ions and electrons. As the driving field will (in the intensity regime necessary for HHG) strongly ionize the generating medium, the strongest contribution to the refractive index will come from the free electrons and results in a phase shift (with respect to vacuum plane waves) of

$$d\phi_{plasma}(r, z) = \frac{e^2 \lambda^2}{8\pi^2 \epsilon_0 m_e c^2} N_{el}(r, z, t) dz \quad (3.19)$$

with ϵ_0 being the vacuum polarizability and $N_{el}(r, z, t)$ the electron density that depends on the laser intensity and therefore on space and time.

Under certain circumstances (involving the target density, size and position of the medium with respect to the focus and other things) phase-matching can be achieved (see for example (Balcou et al. 1997) and references therein). Depending on the precise conditions, this can lead to more or less complex spatial beam profiles and temporal pulse shapes.

3.1.3 Noise sources and upconversion

As the main interest in this work is to provide a frequency comb suitable for high resolution spectroscopy in a wavelength range previously inaccessible to ultranarrowband lasers, one main question that arises is, weather the frequency comb will survive the nonlinear conversion or not. As was already stated earlier, if the nonlinear conversion is elastic that is if the effective photonic

equation of motion⁹ is time-independent, energy conservation requires that the generated photons are sums of integer numbers of photons from the driving field. If that driving field is an ideal frequency comb with frequencies (2.8) the output of the n^{th} harmonic has to contain frequencies

$$\omega_j^{(2n+1)} = j\omega_r + (2n+1)\omega_{CE} \quad (3.20)$$

and no other components.

However, a real frequency comb suffers from noise both in phase and amplitude due to fundamental limits (like shot noise) and technical noise sources (like acoustic vibrations modulating the repetition rate of the laser, air currents, thermal fluctuations and the like). Any of these will add other spectral components that may be broadband (like shot noise, which has a white frequency spectrum). Also the time independence of the conversion dynamics has to be checked critically. The theoretical derivation presented in appendix A completely neglects other channels than recombination back to the ground state. One major other channel is ionization, which does not contribute to the generated radiation but changes ground state population and the dispersion relation for propagation of the electric field inside the medium. This section tries to discuss the impact of all these noise sources on the expected frequency structure of the generated radiation.

A simple, purely classical analysis of the process of nonlinear upconversion of a harmonic signal shows that the phase noise power in the signal will be amplified in the upconverted signal with respect to its carrier by a factor n^2 with n being the harmonic order of the upconverted signal. In brief, the argument is as follows. Let's assume an input signal

$$V(t) = V_0 \exp(i(\omega_0 t + \phi(t)) + c.c.), \quad (3.21)$$

where $\phi(t)$ is the phase noise term. If the phase noise is sufficiently small $\langle \phi^2(t) - \langle \phi^2 \rangle \rangle \ll 1$ the power spectrum of this signal is given by Rutman (1978)

$$|\hat{V}(\omega)|^2 = \frac{V_0^2}{4} (\delta(\omega - \omega_0) + |\hat{\phi}(\omega - \omega_0)|^2). \quad (3.22)$$

Under the assumption that the nonlinear conversion coefficient is determined by the carrier only, the n^{th} harmonic of that signal will take the form

$$V_n(t) = V_n(V_0, \omega_0) \exp(i(n\omega_0 t + n\phi(t))) \quad (3.23)$$

and the power spectrum of the upconverted signal becomes

$$|\hat{V}_n(\omega)|^2 = \frac{V_n^2(V_0, \omega_0)}{4} (\delta(\omega - n\omega_0) + n^2 |\hat{\phi}(\omega - \omega_0)|^2). \quad (3.24)$$

If the harmonic order becomes too high, the noise background will eventually become larger than the carrier signal at ω_0 (within some bandwidth) so that the carrier can no more be identified. This phenomenon is customarily referred to as carrier collapse in harmonic upconversion. Based on this argument, Telle (1996) have predicted that a phase coherent radio frequency to optical link would not be possible with frequency combs.

⁹i.e. after taking the trace over the atomic degrees of freedom.

Amplitude noise in the driving signal will produce amplitude changes in the upconverted signal that may be very large as the conversion efficiency depends highly nonlinearly on the driving field strength. The driving amplitude is also coupled to the phase of the generated field via (A.24). For example, for a driving field with an intensity high enough that the ponderomotive energy is 10 times the photon energy of the fundamental field, an amplitude change of 10% could already cause a nonlinear phase change of 2π for the long trajectory.

Another effect that affects the phase of the generated light (as well as the fundamental radiation field) is the linear refractive index of the generating medium. As for high order harmonic generation the driving field is so strong that many atoms are ionized, the dispersion inside the medium is dominated by the plasma refractive index which in turn is dominated by the contribution from the electrons. The electron plasma dispersion relation is given by

$$k(\omega) = \frac{\omega}{c} \sqrt{1 - \frac{\omega_{el}^2}{\omega^2}}, \quad (3.25)$$

where ω_{el} is the plasma frequency

$$\omega_{el} = \sqrt{\frac{N_{el}e^2}{\epsilon_0 m_e}}, \quad (3.26)$$

and N_{el} is the electron density. Fluctuations in the plasma density lead to phase fluctuations in both the driving wave and the generated field. Such fluctuations may come from density fluctuations of the generating medium but they are also induced by fluctuations in the driving intensity. This is an additional mechanism that couples amplitude and phase of the generated XUV radiation. The plasma dispersion relation approaches the vacuum dispersion relation quadratically as the frequency ω increases. Therefore the plasma density has the largest effect on the fundamental wave propagation. For the 11th harmonic the effect is a factor of 121 weaker.

Other sources of noise in the HHG radiation include spontaneous emission from the plasma recombination and decay from excited states. These spontaneous emission processes are however typically nondirectional, so that the power gets distributed across the entire solid angle 4π and only a small amount is emitted into the well-collimated Gaussian beam of HHG. There may also be other bound states than the ground state, to which the atom can recombine, resulting in an emission of photons with a different energy. However such processes are rather improbable and additionally, as the atom can carry away momentum, this results in an emission that will go into a large solid angle, so that it will have only small power inside the well collimated beam of HHG radiation.

The experiments by Zerne et al. (1997), Bellini et al. (1998) and Lynga1999 clearly show that the noise contributions from fluctuations of the gas density and other external factors to the phase and amplitude of the generated radiation are not large. However, these experiments only test such external noise sources as two identical replica of one laser pulse are used to generate XUV radiation in two different media and observing the interference between the two XUV beams. By doing that, any fluctuations in the driving field are rejected as they affect both XUV beams in the same way. Therefore it remains to be proven that the temporal coherence of the driving frequency comb actually survives the high harmonic process.

Gain medium	λ [nm]	P_{av} [W]	f_r [MHz]	τ [fs]	P_p [MW]	Reference
Ti:Sapphire	790	2	11	30	6	Fernandez et al. (2004)
Yb:Fibre	1060	76	75	400	2.5	Limpert et al. (2003)
Yb:Fibre	1060	10	75	80	1.7	Limpert et al. (2002)
Yb:YAG Disk	1030	60	34.3	810	2.1	Innerhofer et al. (2003)
Yb:KY(WO ₄) ₂	1028	22	24.6	240	3.7	Brunner et al. (2002)
Yb:YAG + fiber	1030	18	34	33	12	Innerhofer et al. (2004)
Ti:Sa RegAmp	800	0.7	0.1	35	200	Lindner et al. (2003)

Table 3.1: Currently available ultrafast high power laser oscillators and their parameters. λ : Wavelength, P_{av} : average power, f_r : repetition frequency, τ : pulse duration, P_p : peak power

3.2 Enhancement resonators for frequency combs

To simultaneously meet the requirements for high resolution spectroscopy with frequency combs (Chapter 2.3) and high harmonic generation (Chapter 3.1), to reach the XUV wavelength range, a laser source is required that provides GW peak powers while maintaining a repetition rate of several 10-100 MHz.

The peak power of a mode-locked laser is approximately given by the product of the average power P_{av} and the duty factor $2\pi(\omega_r\tau)^{-1}$, where ω_r is the repetition frequency of the laser and τ is the pulse duration. A selection of available sources that provide high peak powers at repetition rates in the MHz range is given in table 3.1. It can be seen there, that highest average output powers can be achieved using Ytterbium (Yb) doped thin disk lasers. However, the gain bandwidth of these laser materials is relatively small, resulting in pulse durations in the several 100 fs to ps range. Fiber lasers with Yb as gain medium show similar properties. In contrast, Ti:Sapphire based laser systems can produce 10 fs pulse durations and with longer pulse durations give the ability to tune the center wavelength over a wide range. These lasers are typically limited to around 1 W average output power due to the available pump sources and constraints from the mode locking mechanism. All of the given laser systems provide a few MW peak power with the exception of the last entry in the table. This system is a commercially available regenerative amplifier system working at a considerably lower repetition rate than the others. It is the only system in the list, for which high order harmonic generation with relatively high repetition rates and conventional methods has been reported. None of the other listed systems seems to provide sufficient peak power, and other ways of obtaining the required field strength, while keeping the repetition rate high, have to be sought.

A common technique to enhance the nonlinear conversion efficiency of a continuous laser source is to place the nonlinear medium inside a optical resonator arrangement. If certain resonance conditions are met, the light wave stored inside the resonator interferes constructively with the wave driving the resonator, and orders of magnitude higher circulating power compared to the incident power can be achieved inside such an arrangement. This has two effects:

- The high power can drive the nonlinear medium more strongly, resulting in stronger nonlinear response and higher single pass conversion efficiency.

- The power that is not converted after a single pass through the medium remains cycling in the resonator and can contribute to subsequent passes.

For mode-locked laser sources that emit a periodic pulse train, this technique is also applicable and has been proven in several applications to enhance nonlinear conversions (Persaud et al. 1990, Watanabe et al. 1994, Yanovsky and Wise 1994, McConnell et al. 2001). Additionally resonant cavities for mode-locked lasers have also been proposed by Jones and Ye (2002) and later used (Vidne et al. 2003, Jones and Ye 2004) for "coherent amplification". In that scheme a resonator was driven with the laser output until it reached steady state and a pulse with enhanced power was circulating in the resonator. That pulse was then ejected from the resonator using an acoustooptic modulator. If this sequence is periodically repeated, it results in an amplified pulse train but with a lower repetition rate.

The resonance condition for a mode-locked source is somewhat more complicated than for a continuous source as it demands that the incoming and stored light stay in phase round trip after round trip not only for a single frequency but for an entire comb of frequencies as given by (2.8). Expressed in time domain language, the resonance is achieved, if

- the stored pulse envelope has not changed its shape after one round trip through the resonator,
- the stored pulse envelope after one round trip is synchronised to the next incoming pulse and
- the electric fields inside the envelopes of the stored pulse and the incoming pulse stays in phase.

The first statement says that the dispersion inside the resonator has to be zero (after each round-trip). The other two statements (which to be meaningful, require the first) say that the resonator repetition rate and offset frequency have to match those of the driving laser.

In the following sections a brief overview on optical resonators and their steady state response to monochromatic light fields will be given. A formalism is derived to extend that to mode-locked laser sources. Then, methods for dispersion control and characterization will be described. This is a crucial point in designing and building a resonator for mode-locked lasers. Also a method to determine the reflectivity of the low loss mirrors used for the cavity that was built during this work will be presented. Finally some ideas on how introducing a small nonlinearity into such a resonator might help improving its properties will be given.

3.2.1 Passive optical resonators

In general, to find the eigenmodes of an optical resonator involves solving the boundary value problem of the wave equation for the electromagnetic field¹⁰. For laser beams, in most circumstances it is sufficient to use the so-called paraxial approximation in conjunction with spherical boundary conditions (spherical mirrors) which leads to eigenmode solutions called Gaussian

¹⁰see for example Jackson (1962).

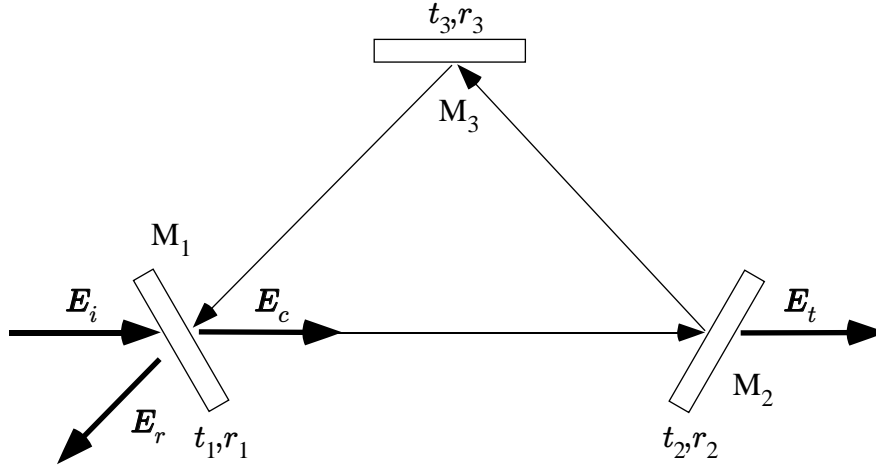


Figure 3.6: Sketch of a typical optical resonator. The incident electric field \mathbf{E}_i is coupled to the resonator through a input coupler M1 with complex transmission amplitude $t_1(\omega)$ and reflection amplitude $r_1(\omega)$. Circulating field \mathbf{E}_c , reflected field \mathbf{E}_r and transmitted field result from the driving incident field.

beams as introduced by Kogelnik and Li (1966). Then the problem separates into solving for a transversal mode pattern and finding the eigenfrequencies for each of these transversal modes. Optical resonators typically look similar to the sketch given in figure 3.6.

For sake of simplicity, let's assume the incident field has a transversal mode distribution that perfectly overlaps with one of the transversal modes of the resonator. Let's also assume a monochromatic wave of frequency ω and denote the incident complex field amplitude on the beam axis just before the input-coupling mirror \mathbf{E}_i so that the electric field on the beam axis in front of the input coupler can be written as¹¹

$$\mathbf{E}_i(t) = \frac{1}{2}(\mathbf{E}_i e^{i\omega t} + c.c.). \quad (3.27)$$

Likewise we define the reflected field amplitude \mathbf{E}_r on the same side of mirror M1, the circulating amplitude \mathbf{E}_c just behind the input coupling mirror and the transmitted amplitude \mathbf{E}_t just behind the second mirror M2 in the cavity. The circulating field amplitude is given by the part of the incident field transmitted through the mirror M1 plus the field that was already present at this point one round trip earlier and has passed through all the elements in the cavity including reflection off mirror M1. The steady state response of such a system is determined by the requirement that circulating amplitude does not change from round trip to round trip so that

$$\mathbf{E}_c = t_1 \mathbf{E}_i + \mathbf{G}(\omega) \mathbf{E}_c. \quad (3.28)$$

The quantity \mathbf{G} is a matrix¹² often called net round trip gain. Solving equation (3.28) yields

$$\mathbf{E}_c = (1 - \mathbf{G}(\omega))^{-1} t_1 \mathbf{E}_i \quad (3.29)$$

¹¹Throughout this work, bold face characters denote vector quantities. Hats will denote fourier transforms of quantities without hats, except in appendix A where they will also be used for quantum mechanical operators

¹²In general, it is a linear map operating on the electric field. In this special case, were the resonator is assumed

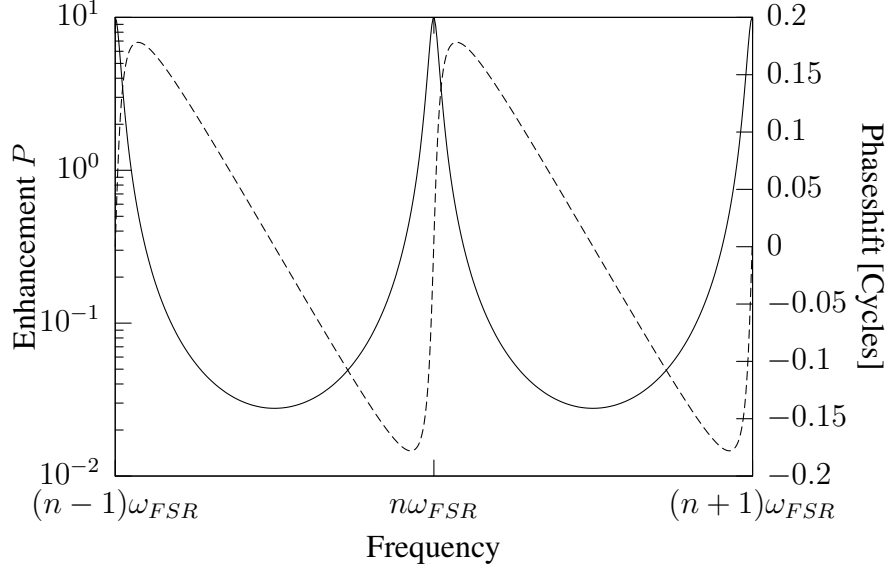


Figure 3.7: Enhancement factor (solid) and phase shift (dashed) with respect to the driving field in a resonator with $r = 0.9$, $t_1 = \sqrt{0.9}$ (according to eqs. (3.31) and (3.32))

In the simplest case if the medium inside the resonator is vacuum and the mirrors have polarization independent reflectivity, \mathbf{G} is a scalar with an explicit value of

$$G(\omega) = e^{i\frac{\omega L}{c}} r_2(\omega) r_3(\omega) r_1(\omega) r_m(\omega) = r(\omega) e^{i(\frac{\omega}{c}L + \phi(\omega))} \quad (3.30)$$

with L being the geometrical round trip length of the resonator, r_m corresponding to a transversal mode dependent round trip phase shift and diffraction loss and $r_1 r_2 r_3 r_m = r(\omega) e^{i\phi(\omega)}$ with r real.

The power of the circulating field compared to the driving power is obtained by taking the square modulus of (3.29) using the form (3.30) for \mathbf{G} to give

$$P(\omega) = \frac{|E_c|^2}{|E_i|^2} = \frac{|t_1(\omega)|^2}{1 + r^2(\omega) - 2r(\omega) \cos(\frac{\omega}{c}L + \phi(\omega))}. \quad (3.31)$$

The phase shift of E_c is given by

$$\psi(\omega) = \arctan \left(\frac{r(\omega) \sin(\frac{\omega}{c}L + \phi(\omega))}{1 - r(\omega) \cos(\frac{\omega}{c}L + \phi(\omega))} \right) + \arg t_1(\omega) \quad (3.32)$$

If r , ϕ and t_1 are for now assumed to be constant (or at least slowly varying in the sense of what follows), the enhancement factor (3.31) has a maximum if the argument of the cosine in

time independent, this map is diagonal in fourier space so that it is a multiplicative function of frequency. In section 3.2.5 an example will be given, were it is a (slightly) more complex map.

(3.31) is an integer multiple of 2π , which minimizes the denominator. On resonance the power enhancement is

$$P = \frac{|t_1|^2}{(1-r)^2}. \quad (3.33)$$

For a passive resonator r is always smaller than unity and for a given coupling $T_1 = |t_1|^2$, as $r < \sqrt{1-T_1}$ has to be true, the highest enhancement achievable is $P = 2/T_1$ (for $T_1 \ll 1$). The spacing between two such resonances is $\omega_{FSR} = 2\pi c/L$ and is frequently called the free spectral range (FSR). The full width half maximum (FWHM) width of these is (assuming $1-r \ll 1$)

$$\Delta\omega_{FWHM} = \frac{1-r}{\pi\sqrt{r}}\omega_{FSR} =: \omega_{FSR}/\mathfrak{F}. \quad (3.34)$$

This width sets the scale for a "slowly varying" $G(\omega)$. The quantity \mathfrak{F} is customarily called the cavity finesse.

Frequently the problem of maximal enhancement is posed differently: For a given resonator with certain intrinsic loss (determined by the mirror quality or other optical elements in the resonator), what is the best coupling mirror to maximize the enhancement inside the resonator? For that purpose it is convenient to split the round trip gain into the contribution from the coupling r_1 and the rest of the cavity r_r so that $G = r_1 r_r \exp(i(L\omega/c + \phi))$. If a lossless input coupler is assumed

$$G = \sqrt{1-|t_1|^2} r_r e^{i(\frac{L\omega}{c} + \phi)}, \quad (3.35)$$

the on-resonance enhancement factor becomes

$$P = \frac{|t_1|^2}{(1 - \sqrt{1-|t_1|^2} r_r)^2} \quad (3.36)$$

which has limits $P = 1$ for $|t_1| = 1$ and $P = 0$ for $t_1 = 0$. For

$$T_{max} := |t_1|^2 = 1 - r_r^2 \quad (3.37)$$

it has a maximum. The transmission T_{max} is often referred to impedance matched coupling. The enhancement as a function of the input coupler transmission T_1 is plotted in figure 3.8. The value of P at the maximum is

$$P_{max} = \frac{1-r_r^2}{(1-r_r^2)^2} = 1/T_{max} \approx \mathfrak{F}/\pi. \quad (3.38)$$

3.2.2 Femtosecond pulses in dispersive resonators

Because the response of the resonator described in section 3.2.1 is linear, its response to an arbitrary electric field $E_i(t)$ (skipping polarization effects for the moment) may be readily calculated via the Fourier transform

$$E_i(t) = \frac{1}{\sqrt{2\pi}} \int_{-\infty}^{\infty} \hat{E}_i(\omega) e^{i\omega t} d\omega \quad (3.39)$$

$$\hat{E}_i(\omega) = \frac{1}{\sqrt{2\pi}} \int_{-\infty}^{\infty} E_i(t) e^{-i\omega t} dt. \quad (3.40)$$

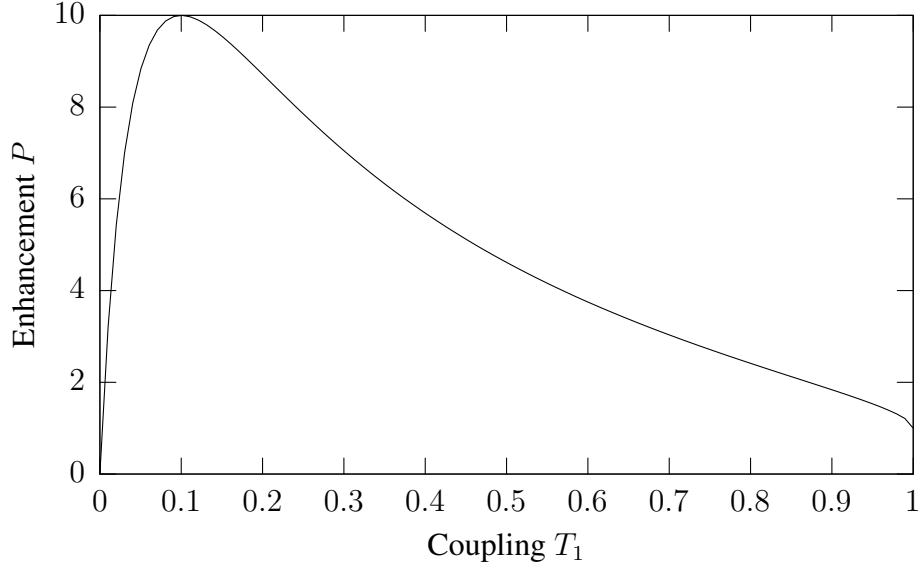


Figure 3.8: Enhancement factor in a resonator with a loss of 10% per round trip, i.e. a value of $r_r^2 = 0.9$.

The Fourier transform of the circulating field in the resonator is then given by (using eq. (3.29))

$$\hat{E}_c(\omega) = \frac{t_1(\omega)\hat{E}_i(\omega)}{1 - G(\omega)}, \quad (3.41)$$

from which the circulating field $E_c(t)$ may be calculated.

Let us first consider an incoming radiation with a broadband spectrum and no frequency comb structure. If the incident light has little structure on the scale of one free spectral range of the resonator, say between ω'_n and ω'_{n+1} in (3.44), we may approximate the total power $W_{i,n}$ of the incident field in that frequency bin by assuming constant power density across the bin:

$$W_{i,n} \propto \int_{\omega_n}^{\omega_{n+1}} |\hat{E}_i(\omega)|^2 d\omega \approx |\hat{E}_i(\omega_n)|^2 (\omega_{n+1} - \omega_n) \quad (3.42)$$

The power of the circulating field within the n^{th} bin $W_{c,n}$ is then

$$\begin{aligned} W_{c,n} &\propto \int_{\omega_n}^{\omega_{n+1}} |\hat{E}_c(\omega)|^2 d\omega \approx \frac{\omega_{n+1} - \omega_n}{2\pi} |\hat{E}_i(\omega_n) t_1(\omega_n)|^2 \int_0^{2\pi} |1 - r(\omega_n) e^{i\phi}|^{-2} d\phi = \\ &= |\hat{E}_i(\omega_n)|^2 \frac{|t_1(\omega_n)|^2}{1 - r^2(\omega_n)} (\omega_{n+1} - \omega_n) \leq |\hat{E}_i(\omega_n)|^2 (\omega_{n+1} - \omega_n) = W_{i,n} \end{aligned} \quad (3.43)$$

where t and r were also assumed to be slowly varying. This is always less than or equal to the incident power per bin, where equality occurs for lossless coupling ($|t|^2 = 1 - r^2$). Therefore a resonator is of no use for enhancing broadband radiation although it might be useful for filtering it.

For a the (broadband) output of a mode-locked laser whose spectral power is concentrated in the modes of a frequency comb with frequencies (2.8) however, the situation may be completely different. If the resonator is constructed such that each mode of the comb sits precisely on one resonance, each of the comb modes is enhanced like a harmonic wave so that the entire spectrum gets enhanced. The resonance condition of the resonator

$$\begin{aligned} 2n\pi &= \frac{L\omega'_n}{c} + \phi(\omega'_n) \\ \leftrightarrow \omega'_n &= n \frac{2\pi c}{L} - \frac{c\phi(\omega'_n)}{L} \end{aligned} \quad (3.44)$$

does not explicitly give the resonance frequencies ω'_n , because $\phi(\omega'_n)$ has first to be solved for ω'_n . Yet it already looks like a frequency comb as in (2.8), except that the "offset frequency" $c\phi(\omega'_n)/L$ is not independent of n . To make the expression (3.44) a real frequency comb with a regular mode spacing, $\phi(\omega)$ has to be of the form¹³

$$\phi(\omega) = -\phi'_{CE} + \tau'\omega \quad (3.45)$$

at least within the spectral region of interest, in which case

$$\omega'_n = \frac{n2\pi + \phi'_{CE}}{L/c + \tau'} =: n\omega'_r + \omega'_{CE} \quad (3.46)$$

with an effective repetition rate $\omega'_r = 2\pi/(L/c + \tau')$ and offset frequency $\omega'_{CE} = \phi'_{CE}/(L/c + \tau')$ for the resonator¹⁴. Given that condition, the output of a mode-locked laser can be tuned into resonance with the resonator by adjusting the repetition rate ω_r and carrier envelope offset frequency ω_{CE} to match ω'_r and ω'_{CE} respectively.

As any element, including dielectric mirrors and even air, inside an optical resonator will in general have a round trip phase contribution that differs from (3.45), it is important to understand, what impact a different round trip phase will have on the stored broadband frequency comb and how accurately the round trip phase will have to be controlled to achieve good performance of the resonator. The following discussion is similar to the treatment by Petersen and Luiten (2003).

If the resonator is driven by an electric field as in (2.4), with frequencies (2.8), the Fourier components of the circulating field (again using (3.29)) are then

$$\hat{E}_{c,n} = \frac{t(\omega_n)\hat{A}_n}{1 - G(\omega_n)} = \frac{t(\omega_n)\hat{A}_n}{1 - r(\omega_n)e^{i(\frac{L}{c}\omega_n + \phi(\omega_n))}}, \quad (3.47)$$

while components with other Fourier frequencies vanish. The A_n here have been appropriately renumbered, so that the second from of (2.8) with $\omega_{n=0} = \omega_{CE}$ is used. The round trip phase

¹³Other really pathological forms are possible where ϕ does ugly things between the resonances. But let's better not think about something like this. If the comb of resonances is required to be equidistant for any length L , the given form is the only possible one.

¹⁴with this, the names for the two coefficients ϕ'_{CE} and τ' find their natural explanation as the resonator's round trip to round trip carrier envelope phase slip and additional round trip time.

$\phi(\omega)$ may be expanded into a Taylor series around an arbitrary center frequency¹⁵ ω_c

$$\phi(\omega) = -\phi'_{CE}(\omega_c) + \tau'(\omega_c)\omega + \psi(\omega) \quad (3.48)$$

with appropriate coefficients ϕ'_{CE} and τ' so that the error term $\psi(\omega_c + \Delta\omega) = \mathcal{O}(\Delta\omega^2)$ is of second order around ω_c . By that, it is ensured that $\psi(\omega)$ is slowly¹⁶ varying in the vicinity of ω_c . In analogy to (3.46), we define

$$\begin{aligned} \omega'_r(\omega_c) &= \frac{2\pi}{\frac{L}{c} + \tau'(\omega_c)} \\ \omega'_{CE}(\omega_c) &= \frac{\psi'_{CE}(\omega_c)}{\frac{L}{c} + \tau'(\omega_c)}. \end{aligned} \quad (3.49)$$

With the definitions (3.49) the exponent in (3.47) takes the form

$$\frac{L}{c}\omega_n + \phi(\omega_n) = \frac{2\pi}{\omega'_r(\omega_c)}(n\omega_r + \omega_{CE} - \omega'_{CE}(\omega_c)) + \psi(\omega_n). \quad (3.50)$$

If the repetition rate of the driving laser is close to an integer multiple k of the effective repetition rate of the resonator at ω_c , it is sensible to exploit the periodicity of the exponential in the resonator response (3.47) and rewrite it using the definitions

$$\begin{aligned} \delta\omega_r &= \frac{\omega_r}{\omega'_r(\omega_c)} - k \\ \delta\omega_{CE} &= \frac{\omega_{CE} - \omega'_{CE}(\omega_c)}{\omega'_r(\omega_c)}, \end{aligned} \quad (3.51)$$

so that it reads

$$\begin{aligned} \exp\left(i2\pi\left[n(k + \delta\omega_r) + \delta\omega_{CE} + \frac{\psi(\omega_n)}{2\pi}\right]\right) &= \\ \exp\left(i\left[2\pi(n\delta\omega_r + \delta\omega_{CE}) + \psi(\omega_n)\right]\right) &= \exp(i\tilde{\psi}(\omega_n)) \end{aligned} \quad (3.52)$$

introducing the effective round trip phase

$$\tilde{\psi}(\omega) = 2\pi\left(\frac{\omega - \omega_{CE}}{\omega_r}\delta\omega_r + \delta\omega_{CE}\right) + \psi(\omega) = \quad (3.53)$$

$$= 2\pi\left[\omega\left(\frac{1}{\omega'_r(\omega_c)} - k\frac{1}{\omega_r}\right) + k\frac{\omega_{CE}}{\omega_r} - \frac{\omega'_{CE}(\omega_c)}{\omega'_r(\omega_c)}\right] + \psi(\omega) = \quad (3.54)$$

$$= \omega(T'(\omega_c) - kT) + k\phi_{CE} - \phi'_{CE}(\omega_c) + \psi(\omega). \quad (3.55)$$

The form (3.54) resubstitutes (3.51) while form (3.55) uses the (effective) periods $T = 2\pi/\omega_r$, $T'(\omega_c) = 2\pi/\omega'_r(\omega_c)$ and the (effective) pulse to pulse CE phase shifts $\phi_{CE} = 2\pi\omega_{CE}/\omega_r$ and $\phi'_{CE}(\omega_c) = 2\pi\omega'_{CE}(\omega_c)/\omega'_r(\omega_c)$. The effective resonator response is then

$$\hat{E}_{c,n} = \frac{t(\omega_n)\hat{A}_n}{1 - r(\omega_n)e^{i\tilde{\psi}(\omega_n)}}. \quad (3.56)$$

¹⁵not necessarily equal to one or the ω_n in (2.8)

¹⁶at most quadratically

The incident frequency comb will be close to resonance for spectral regions for which the effective round trip phase is sufficiently close to integer multiples of 2π , i.e., in the high finesse limit¹⁷

$$\tilde{\psi}(\omega) - n2\pi \ll \frac{\pi}{\mathfrak{F}}. \quad (3.57)$$

For $\delta\omega_r = \delta\omega_{CE} = 0$ the effective round trip phase is of second order around ω_c so that it may be written as

$$\tilde{\psi}(\omega) = \psi(\omega_c + \Delta\omega) = \frac{1}{2}\psi_2\Delta\omega^2 + \mathcal{O}(\Delta\omega^3). \quad (3.58)$$

Then the modes of the driving field in the vicinity of ω_c will be to first order precisely on resonance and tune out of resonance to second order in $\Delta\omega$. As the lowest repetition rate ω_r for which this condition may be fulfilled¹⁸ is $k = 1$, this once again justifies the names for $\omega'_r(\omega_c)$ and $\omega'_{CE}(\omega_c)$. If higher than second order contributions to $\tilde{\psi}$ can be neglected in the frequency range of interest, the enhancement of the modes of the incident frequency comb will have dropped to 1/2 of the maximum value once

$$\begin{aligned} \tilde{\psi}(\omega_c + \Delta\omega) \approx \frac{1}{2}\psi_2\Delta\omega^2 &= \frac{\pi}{\mathfrak{F}} \\ \leftrightarrow 2\Delta\omega &= 2\sqrt{\frac{2\pi}{\psi_2\mathfrak{F}}} =: \Delta\omega_{FWHM}, \end{aligned} \quad (3.59)$$

where (3.34) was used. This can be significantly larger than one FSR of the cavity. For instance, a cavity in air of 3 m round trip length (FSR about 100 MHz) and no other dispersive elements has a ψ_2 of about 30 fs². With a finesse $\mathfrak{F} = 100\pi$ it will have a FWHM bandwidth of¹⁹ $51/2\pi$ THz = 8.2 THz.

The quantity $\psi_2 = (d^2\tilde{\psi}/d\omega^2)(\omega_c) = (d^2\phi/d\omega^2)(\omega_c)$ is often referred to as the group delay dispersion (GDD) of an optical path (in this case the resonator round trip) at ω_c . This and higher order terms in the Taylor expansion of $\phi(\omega)$ cause a wave packet to change its shape while passing through the optical path. In the ultrafast community, it is customary to specify $d^2\phi(\omega)/d\omega^2$ instead of $\phi(\omega)$ or the Taylor coefficients. Of course the two quantities are related via

$$\phi(\omega) = \int \int \frac{d^2\phi(\omega)}{d\omega^2} (d\omega)^2 + C_0 + C_1\omega. \quad (3.60)$$

$d^2\phi(\omega)/d\omega^2$ is a convenient quantity²⁰ as the integration constants C_0 and C_1 are usually hard to measure, for many purposes not very important (as in this case where those may be set to

¹⁷Note that in (3.56) in fact only the values $\tilde{\psi}(\omega_n)$ are relevant. $\tilde{\psi}$ could mathematically do anything between these points without affecting the result. Luckily, in reality, it usually doesn't unless there is a nearby narrow resonance in some material in the cavity, which is not desirable for a low loss (high finesse) resonator. This means $\tilde{\psi}$ can be assumed to be slowly varying on the scale of ω_r . Therefore demanding $\tilde{\psi}(\omega_n)$ to be small is equivalent to requiring it to be small everywhere.

¹⁸ $k = 0$ is usually not practical ($L \approx 0!$) if no special tricks like electromagnetically induced transparency (EIT) are utilized as in the work of Wicht et al. (1997) where the light is stopped inside the resonator

¹⁹take care, not to confuse angular frequency, usually denoted by ω and cycles per second $\nu = \omega/2\pi$.

²⁰Note that $d^2\phi(\omega)/d\omega^2$ is universal in the sense that the second derivative of $\tilde{\psi}(\omega)$ yields the same function.

arbitrary values by tuning the laser) and depend on the choice of lower integration bounds (in our case for example ω_c for both integrations). On the other hand, starting from $d^2\phi/d\omega^2$, if this function is complicated (or from a noisy measurement, i.e. looks complicated) it is hard to tell if $\tilde{\psi}(\omega)$ will be sufficiently linear over the region of interest and condition (3.57) can be fulfilled.

Another interesting "resonance condition" for a frequency comb in a cavity exists if the repetition rate of the laser is tuned to small rational fractions of the resonator repetition rate so that $\omega_r/\omega'_r(\omega_c) = k/l$, k and l again integer. Then by inspecting (3.52) it can be easily seen that every l^{th} mode of the incident frequency comb will be resonant with the cavity if ω_{CE} is tuned appropriately. This means that about the l^{th} fraction of the total incident power can be made resonant. In the high finesse limit, the circulating power of the nonresonant modes can be neglected. Therefore one may define an (now approximate) effective round trip phase as in (3.53) with only k replaced by k/l . The circulating power is l times reduced compared to the case $l = 1$. As the spacing of the resonant modes of the incident comb is now l times larger, at the same time the repetition rate of the circulating pulse train is also l times higher than the incident repetition rate. This can of course be understood in the time domain, as under these conditions the round trip time of the resonator is such that each of the pulses circulating in the resonator meets again a pulse from the laser after l round trips. The high finesse limit (and therefore the modified ψ) is valid in this case, as long as all the intermediate modes are sufficiently suppressed with respect to the resonant modes, i.e. that the adjacent mode of a resonant mode of the incident frequency comb is sufficiently far off resonance that it can be neglected. This means that $l \ll \mathfrak{F}$. For higher values of l , the distances of the driving modes to their next resonance become so dense, that the resonator response can not separate them anymore and the situation will be similar to that described in (3.43) and the total power that is circulating approaches $|t|^2/(1 - r^2)$ independent of $\delta\omega_r$ and $\delta\omega_{CE}$.

The last step in describing the resonator response to a mode-locked laser pulse train is to reconstruct the electric field as a function of time, circulating inside the resonator. For that we only have to perform the inverse Fourier transformation

$$E_c(t) = \sum_{n=-\infty}^{\infty} \hat{E}_{c,n} e^{i(n\omega_r + \omega_0)t} + c.c.. \quad (3.61)$$

As the phase distortion²¹ (3.32) of the Fourier components is bounded by $\pm\pi/2$, the resulting pulse will not acquire a strong chirp, even if the round trip phase varies severely. That means that if the driving pulse train is Fourier limited, the circulating pulse train will be essentially Fourier limited (neglecting again the input coupler). The amplitudes, however, can change by many orders of magnitude as modes move from resonance to off resonance, changing the shape of the intracavity spectrum significantly. This in turn will increase the Fourier limited pulse duration of the stored pulse, as (compared to resonant modes) the intensity of nonresonant modes is always *reduced*, which narrows the spectrum.

Depending on the shape of the input field E_i and optimization criteria, setting $\delta\omega_r = \delta\omega_{CE} = 0$ is not the only sensible choice. For example it might be of interest to maximize the total power

²¹excluding the input coupler transmission

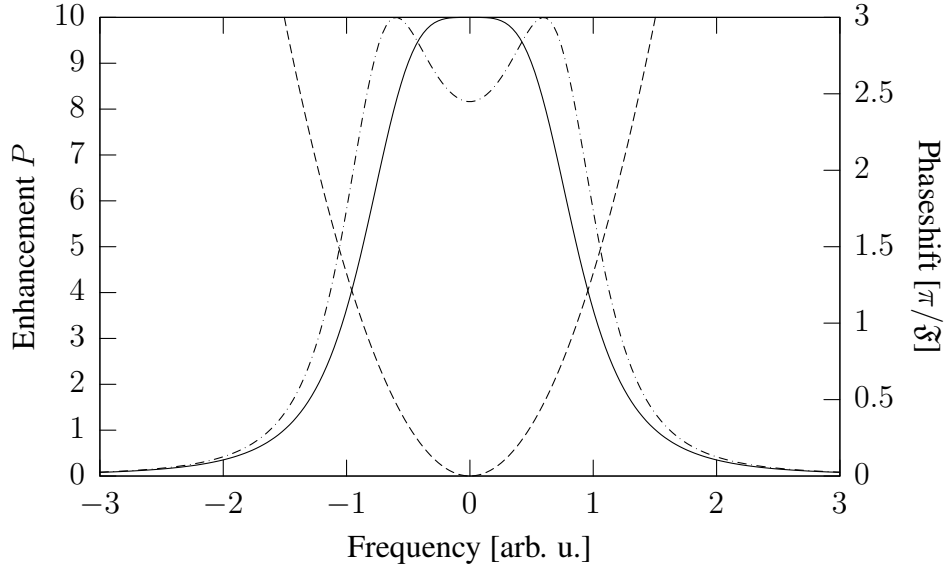


Figure 3.9: Enhancement (solid) of a tuned comb in a resonator with $r = 0.9$, effective round trip phase shift (dashed) and enhancement for a slightly shifted phase (dash-dotted) so that the enhanced range is broader. This illustrates that setting $\delta\omega_r = \delta\omega_{CE} = 0$ may be not the only sensible choice.

stored in the resonator, the Fourier limited peak power of the stored pulse and so on. Figure 3.9 tries to illustrate that by showing that the FWHM bandwidth of the resonator may be increased by setting a slightly different offset frequency at the laser, shifting $\tilde{\psi}$ to slightly more negative values. Solving such an optimization problem generally depends on the input light field and the resonator parameters and has to be solved numerically or experimentally. An approximation to maximizing the average intracavity power is to minimize the quadratic distance of $\tilde{\psi}$ to 0, as the power enhancement also decreases quadratically (to lowest order) with that distance. As enhancing spectral regions with no incident power will not increase the circulating power, it seems to be sensible to weight the quadratic distance of $\tilde{\psi}$ with the value of the incident power. Therefore let's try to minimize the figure of merit

$$F = \int |\hat{E}_i(\omega)|^2 \tilde{\psi}^2(\omega) d\omega. \quad (3.62)$$

As $\tilde{\psi}$ depends linearly on the parameters to optimize ($\delta\omega_r$ and $\delta\omega_{CE}$) in (3.53), this has an analytic solution that can be easily calculated. Figure 3.10 shows an example for such a calculation.

3.2.3 Dispersion control

As was seen in the previous section, dispersion control is most critical for achieving the highest resonant bandwidth for a high finesse resonator, i.e. for achieving the highest peak power inside such a resonator. Therefore methods are required for diagnosing and controlling the dispersion

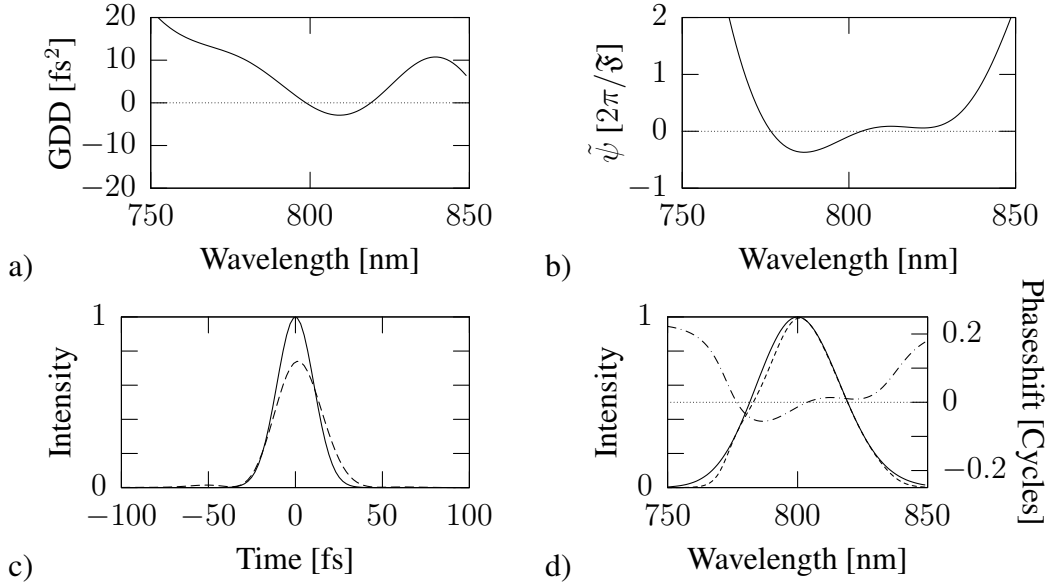


Figure 3.10: Steps in a response calculation for a resonator of $\mathfrak{F} = 100\pi$: a) $d^2\phi/d\omega^2$ input data, b) $d^2\phi/d\omega^2$ integrated twice to yield ψ plotted in units of resonance width, integration constants determined using minimization of equation (3.62), c) Fourier limited input pulse envelope (solid) and intracavity envelope (dashed), d) Input power spectrum (solid line), normalized steady state circulating power (dashed) and phase shift (dash-dotted)

inside it. Many fancy methods have been developed in the ultrafast and coherent control communities, among which a few shall be described here. But first let's look at a formal definition of dispersion, how it affects pulse propagation and how it relates to other material characteristics like refractive index.

When solving the electromagnetic wave equation (and many other wave equations) one frequently ends up with solutions of the form

$$E(t, \mathbf{x}) = A(x, y)e^{i(\omega t - k(\omega)z)} + c.c., \quad (3.63)$$

where the function $k(\omega)$ is determined by the wave equation, the boundary conditions and the polarization response of the medium in which the wave is to travel (here we assume homogeneous conditions along propagation direction z , so that k does not depend on z). k is called the wave vector and the function $k(\omega)$ is often referred to as the *dispersion relation*. The dispersion relation may be determined by many different factors. First, the most fundamental factor is the vacuum wave equation²². The interaction with other particles or fields changes the dispersion relation, which in the case of the electromagnetic fields in dielectric media leads to the refractive index $n(\omega) = k(\omega)c/\omega$. Boundary conditions (like in optical fibers) may also change the dispersion relation. For ultrafast optics in general and, as was seen in the previous section, enhancement resonators for short pulses in particular it is important to have techniques available to

²² $k = \omega/c$ for the electromagnetic field and other massless fields

control the function $k(\omega)$ to a high degree of accuracy in order to achieve highest possible peak power (or other specific pulse shapes).

For a given optical path it is customary to integrate the propagation through the medium (which may be heterogenous) and specify the phase shift of the wavefront from input ($z = 0$) to output ($z = z_0$) of the optical path along the optical axis

$$\phi(\omega) = \int_0^{z_0} k(\omega, z) dz. \quad (3.64)$$

The effect of a dispersive medium on a pulse may be estimated in the following way: Let's assume a pulse with a Gaussian amplitude profile

$$E(t) = e^{-\frac{t^2}{2\delta^2} + i\omega_0 t} + c.c. \quad (3.65)$$

where δ is half the $1/e$ intensity duration of the pulse, then the Fourier transform of the pulse before the dispersive path is

$$\hat{E}(\omega + \omega_0) = \delta e^{-\frac{1}{2}\delta^2\omega^2}. \quad (3.66)$$

If $\phi(\omega)$ can be approximated by a Taylor expansion of second order around ω_0 in the range of non-negligible power of the incident light, then after passage through the optical path the Fourier components will be $\hat{E}'(\omega + \omega_0) = \exp(i(\phi_0 + \phi_1\omega + \phi_2\omega^2/2))\hat{E}(\omega + \omega_0)$ so that the pulse electric field is

$$E'(t) = \frac{1}{\sqrt{2\pi}} \int \hat{E}'(\omega) e^{i\omega t} d\omega = \frac{\delta}{\sqrt{\delta^2 - i\phi_2}} e^{-\frac{(\phi_1+t)^2}{2(\delta^2 - i\phi_2)}} e^{i(\phi_0 + \omega_0 t)} + c.c.. \quad (3.67)$$

One can see immediately that $\phi_0 = \phi(\omega_0)$ is a global phase shift, called phase delay, $\phi_1 = d\phi/d\omega(\omega_0)$ is a time delay of the pulse envelope peak and is therefore called group delay. As the change in group delay as a function of frequency is given by $\frac{d^2\phi}{d\omega^2}(\omega_0)$, it is called group delay dispersion (GDD) at the frequency ω_0 . Higher order terms in the Taylor expansion of ϕ are frequently called higher order dispersion (e.g. ϕ_3 : third order dispersion (TOD), ϕ_4 fourth order dispersion (FOD)). The duration of the distorted pulse is

$$\delta' = 2\sqrt{\delta^2 + \phi_2^2/\delta^2}, \quad (3.68)$$

as can be read off the real part of the exponent in (3.67) and starts to change considerably as soon as $\delta^2 \sim \phi_2$. For very large ϕ_2 the pulse duration grows as ϕ_2/δ . The so-called instantaneous frequency in the pulse is the time derivative of the imaginary part of the exponent in (3.67). It turns out to be

$$\omega_{inst} = \omega_0 + \phi_2 t / 2(\delta^4 + \phi_2^2) \quad (3.69)$$

and varies linearly with time, which is why such a pulse is called linearly chirped (see Figure 3.11). As the global phase ϕ_0 and the time delay of the pulse ϕ_1 do not affect the pulse intensity shape, and the latter can be easily adjusted using an appropriate delay line in most circumstances, they are of minor interest. If $\phi(\omega)$ is a complicated function, it is usually not very convenient to use a Taylor expansion as there are many terms required and the overall shape is hard to read out

Material	GDD [fs ² /mm]			reference
	800nm	1024nm	1500nm	
Fused Silica	36	16	-22	Ghosh (1999)
BK7 Glass	45	22	-19	Schott (1984)
Sapphire	58	29	-25	Malitson (1962)
Air (20°, 10 ⁵ Pa)	0.21	0.16	0.11	Bonsch and Potulski (1998)
TOD [fs ³ /mm]				
Fused Silica	27	44	133	
BK7 Glass	32	49	138	
Sapphire	42	65	176	
Air (20°, 10 ⁵ Pa)	0.10	0.09	0.09	

Table 3.2: Some GDD (in [fs²/mm]) and TOD (in [fs³/mm]) values for typical dielectric media used in optics for typical ultrafast laser wavelengths.

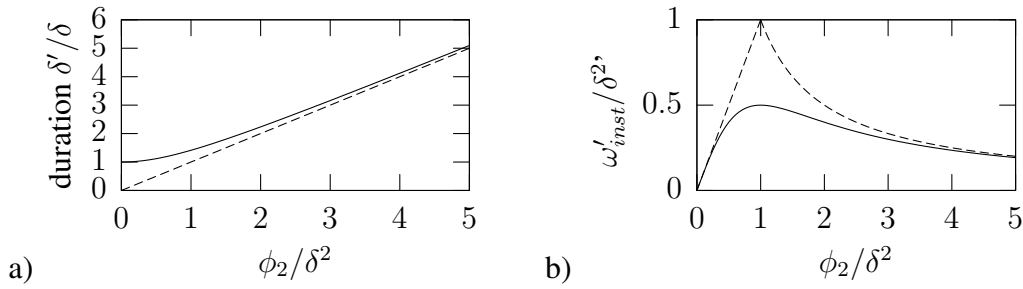


Figure 3.11: Influence of the GDD ϕ_2 on a) pulse duration δ (solid) with asymptote ϕ_2/δ (dashed) and b) chirp speed $d\omega_{inst}/dt$ (solid) and asymptotes ϕ_2/δ^4 and $1/\phi_2$ for small and high GDD respectively (dashed)

of the Taylor coefficients. For these two reasons, it is customary to give the second derivative $\phi''(\omega)$ instead of specifying $\phi(\omega)$ itself. In this way using a specific reference frequency ω_0 as necessary in the Taylor expansion, is also avoided. $\phi''(\omega)$ is related to the refractive index of bulk media via

$$\phi''(\omega) = \frac{d^2}{d\omega^2} k(\omega)l = \frac{d^2}{d\omega^2} \frac{\omega n(\omega)l}{c} = \frac{2n'(\omega) + \omega n''}{c}. \quad (3.70)$$

The refractive index as a function of frequency may frequently be obtained from empirical formulas (at least in the case of transparent media)²³, so that the GDD function may be calculated. In Table 3.2 are listed GDD values for some typical dielectric media.

The simplest form of dispersion control is to use a material of appropriate dispersion properties and thickness adjusted to the required amount of dispersion in the beam path. The advantage of this method is that it is very simple and inexpensive and it can provide huge dispersion values. The disadvantage is that there is only a limited choice of optically transparent media available to

²³So-called Sellmeier formulas as can be found in the work of Ghosh (1999) or other types as in the catalogue of Schott (1984).

choose from, and the only continuous parameter that can be varied is the length of the material. These two facts limit the freedom of choice for a specific dispersion function. Moreover, for Ti:Sapphire laser wavelengths around 800 nm, there is no transparent dielectric medium that has negative GDD. To compensate for the dispersion of glass and other media in an optical path, other techniques resulting in negative GDD are therefore necessary.

Another class of techniques for dispersion control rely on spatially dispersing the frequency components in the optical path and putting different phase delays on each of these components. The simplest versions of this class of dispersive arrangements is shown in figure 3.12. It consists of a system of 4 identical prisms (or gratings). The first prism (or grating) angularly disperses the incoming (broadband) radiation. The second makes the different colors propagate collinearly. The other two prisms (or gratings) reverse the spatial dispersion but as different colors have traveled different paths, the light will remain temporally dispersed. It was shown by McMullen (1979) that such an arrangement with gratings can produce large amounts of negative GDD. Later Fork et al. (1984) realized that a prism arrangement of this type can provide negative GDD with high transmission (which is not possible with gratings), if Brewster-cut prisms are used. Both of these simple arrangements have two continuous parameters to adjust: (i) the distance between the two prisms (gratings) in both halves of the setup and (ii) the distance of the beam from the prism apex or the grating line density. This fact allows one to independently adjust two scalar parameters of the resulting dispersion relation (e.g. GDD and TOD at some center wavelength). Frequently the arrangement shown in figure 3.12a) is folded up by using a mirror at the location of the dashed line, saving two prisms (or gratings) and lots of space.

To gain even more control over the precise functional dependence of $\phi''(\omega)$ one can introduce a programmable phase mask (e.g. a liquid crystal array (Weiner et al. 1992) or a deformable mirror (Heritage et al. 1991)) in the plane marked by the dashed line in figure 3.12a) and arrange imaging optics around it to produce a focus in that plane too, to provide a Fourier plane at the phase mask. Another programmable dispersion control technique introduced by Tournois (1997) uses an acousto-optic modulator with an appropriate (programmable) acoustic waveform from which the light is being scattered in the forward direction. This method has the advantage over the other programmable techniques in that it does not introduce a spatial chirp that has to be canceled and therefore is robust against misalignment of the system. The disadvantage of all of these techniques is that the insertion loss is relatively high and in the percent range.

Last but not least we would like to mention that there is also the method of so-called chirped mirrors proposed and demonstrated by Szipocs et al. (1994), the idea of which is depicted in figure 3.12b). The dielectric coating of such mirrors is designed such that different frequencies have different penetration depths into the layer stack. As the number of layers in such a layer stack can be on the order of 50, the freedom of designing specific dispersion properties is similar to that of a programmable pulse shaper. While dielectric mirrors can have extremely low insertion loss ($\approx 10^{-4}$) and are intrinsically immune against misalignment, they lack the flexibility to adjust the dispersion properties in the experiment and state-of-the-art coating systems have limited precision in control of the layer thickness, so that considerable errors in dispersion may occur on the scale relevant for high finesse resonators as described earlier in this chapter.

Because of the low insertion loss, chirped mirrors are the only sensible choice for dispersion control in high finesse optical resonators (apart from minimizing contributions from dispersive

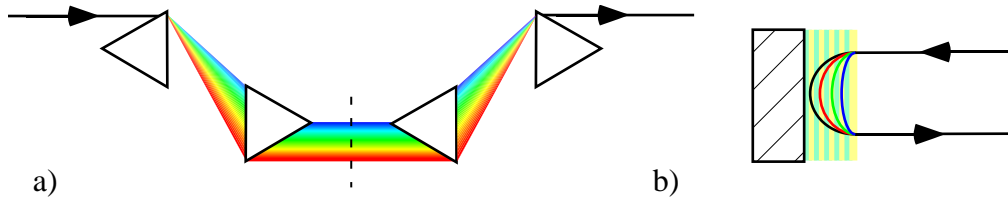


Figure 3.12: a) Simple example of a dispersive beam path using spatially different paths for different frequency components. The dashed line shows a symmetry plane at which a mirror may be placed to fold the system and reduce the number of prisms needed. See text for explanation. b) basic idea of a chirped mirror: The dielectric coating structure permits different penetration depths for different colors so that they acquire different group delays.

media). But because of the limited production accuracy of chirped dielectric mirrors and the high accuracy level required for such resonators, it is necessary to be able to characterize the dispersion inside such a system with high accuracy. The following section will describe a method that was developed during this work and which surpasses other common techniques like white light interferometry in accuracy and robustness.

3.2.4 Precise dispersion characterization

The most common methods for determining dispersion properties of dielectric mirrors and other resonant structures, which have a complicated spectral phase evolution, rely on a Michelson interferometer (Michelson 1891). Such a device produces a well known interference signal

$$I(x, k) = \frac{1}{4}(I_i(k) + T(k)I_i(k) + 2I_i(k)\sqrt{T(k)}\cos(kx + \phi(k))) \quad (3.71)$$

where $I(k, x)$ is the transmitted intensity as a function of wave vector k and delay x , $I_i(k)$ is the incident power from the light source and $\phi(k)$ and $T(k)$ are the phase and absorption²⁴ coefficients of the test sample placed in one arm of the interferometer. There are several ways to extract the quantities of interest $T(k)$ and $\phi(k)$ from equation (3.71). One possibility is to take the integrated output over all frequencies (by simply putting a photodiode at the output port) and record it as a function of the delay x . Taking the Fourier transform of this trace reveals $I_i(k)\sqrt{T(k)}$ and $\phi(k)$. As it is hard to determine x in absolute terms (using interferometric methods), $\phi(k)$ and $d^1\phi/d\omega^1(k)$ are ambiguous but $d^2\phi/d\omega^2(k)$ is not. As already said, this is usually not a problem because the ambiguous quantities can be easily adjusted in an experiment. It is also possible to detect $I(x, k)$ at a fixed delay using a spectrometer at the output of the interferometer (see for example in Sáinz et al. 1994), a method frequently called spectral interferometry, or do both to measure the entire function $I(x, k)$ (Kovács et al. 1995). Any of these is sufficient (under certain conditions) to extract the samples dispersion data.

²⁴more general: loss

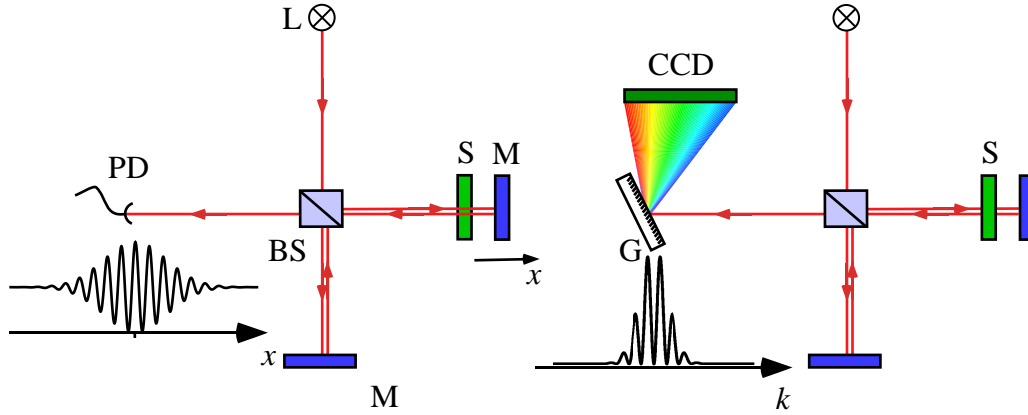


Figure 3.13: Two possible Michelson interferometer setups to make a spectral phasemeter. a) Scanning the length of one arm of the Michelson and observing the interference pattern (as seen by a broadband detector) as a function of the end mirror position. Fourier Transformation yields amplitude and relative spectral phase information. b) With fixed geometry and a spectrally resolving detector at the output. At finite relative delay between the arms a spectral interference pattern is observed that contains the relative spectral phase information.

Because the phase $\phi(k)$ is encoded in the \cos part of equation (3.71), which has a slope < 1 everywhere, high signal to noise ratio (SNR) is required to extract the phase with small error. Additionally, the arms of the Michelson have to be accurately balanced (in terms of dispersion), so that small beam path changes do not lead to unstable measurement results. On the other hand it is well known and we have seen in chapter 3.2.1, that optical cavities can provide extremely narrow resonances with signal slopes $\gg 100$ which relaxes the requirement regarding SNR, and it has been shown, that a mode-locked laser can provide a completely dispersion free reference signal (i.e. perfectly equidistant comb (Udem et al. 1999a)). Therefore it seems to be a good idea to try to use an optical resonator together with a mode-locked laser for dispersion characterization. In this section a method, developed during this work will be explained, that tries to exploit these advantages for characterizing GDD properties of entire resonators and single optical elements using such resonators. In section 4.1.7 data obtained with this method will be presented

Let's look at the transmission through one of the mirrors (transmission $t_1(\omega)$) of the resonator (not the input coupler) using a spectrometer. The signal that can be observed there is the circulating field (3.56) that is transmitted through the mirror

$$I_{t,n} \propto |t_1(\omega_n)E_{c,n}|^2 = \left| \frac{t(\omega_n)t_1(\omega_n)\hat{A}_n}{1 - r(\omega_n)e^{i\tilde{\psi}(\omega_n)}} \right|^2. \quad (3.72)$$

We would like to determine the function $\psi(\omega)$ as in equation (3.48) from this transmission signal. This signal is strongly peaked at $\tilde{\psi}(\omega) = 2j\pi$, j integer, and has little structure in between these resonances. Therefore it seems to be advantageous to find the position of these peaks for each optical frequency ω as a function of repetition rate $\omega_r = 2\pi/T$ and offset frequency

$\omega_{CE} = \phi_{CE}\omega_r/2\pi$ (which can be easily measured) and to extract $\psi(\omega)$ from that. For such a peak, the condition

$$\tilde{\psi}(\omega, T, T', \phi_{CE}) = \omega(T' - kT) + k\phi_{CE} - \phi'_{CE} + \psi(\omega) = 2j\pi \quad (3.73)$$

holds true, where (3.55) was used. In order to solve for $\psi(\omega)$, T' , ϕ'_{CE} and the integers k and j need either to be determined or eliminated. The integer k can easily be found by comparing the length of the resonator to the laser's repetition rate²⁵. The integer j as well as ϕ'_{CE} do not play an important role as they only add a constant offset to $\psi(\omega)$. But resonator round trip time at T' is an unknown in (3.73) and cannot be measured easily with high accuracy. Moreover small changes in T' usually lead to an enormous change in $\tilde{\psi}(\omega)$. For example with a 100MHz cavity for near infrared Ti:Sapphire radiation at 375 THz the product $\omega T'$ is on the order of 10^7 so that changes in T_r on the order of 10^{-7} exhibit a huge effect on the solution of (3.73). To remedy this situation additional constraints on $\tilde{\psi}(\omega)$ can be introduced. For example, one may simultaneously require that

$$\tilde{\psi}(\omega_{fix}) = 2l\pi \quad (3.74)$$

for a fixed frequency ω_{fix} . Then by plugging this condition into (3.73) the term $T' - kT$ may be eliminated and (3.73) can be solved for $\psi(\omega)$

$$\psi(\omega) - 2j\pi = \frac{\omega - \omega_{fix}}{\omega_{fix}}(k\phi_{CE} - \phi'_{CE} - 2l\pi + \psi(\omega_{fix})) + \psi(\omega_{fix}). \quad (3.75)$$

The second derivative of this is

$$\frac{d^2\psi}{d\omega^2} = k \left[\frac{2}{\omega_{fix}} \frac{d\phi_{CE}}{d\omega} + \left(\frac{\omega}{\omega_{fix}} - 1 \right) \frac{d^2\phi_{CE}}{d\omega^2} \right], \quad (3.76)$$

which depends on derivatives of $\phi_{CE}(\omega)$ only. Here $\phi_{CE}(\omega)$ is the solution of (3.73) under the constraint (3.74). Figure 3.14 tries to illustrate equation (3.75).

A simplified schematic of a possible implementation of such a measurement is shown in figure 3.15. Using an electronic feedback loop on the laser resonator length, the comb is kept on resonance with the cavity at frequency ω_{fix} . By tuning the laser offset frequency ω_{CE} , the transmission signal is modified according to (3.72) under the constraint imposed by the lock. The circulating spectrum and laser repetition rate are recorded for different offset frequencies. The result $I(\omega, \phi_{CE})$ should look as in figure 3.16. Each slice of this function at fixed ω looks as in figure 3.7 with the frequency axis replaces by $(\omega - \omega_{fix})\phi_{CE}/\omega_{fix}$ and ω_{FSR} replaced by 2π . It is then easy to find $\phi_{CE}(\omega)$ for which the slice at ω has a maximum (which is not unique). Once $\phi_{CE}(\omega)$ is determined for all slices by choosing maxima in each slice so that $\phi_{CE}(\omega)$ has no jumps (at least locally), equation (3.76) may be evaluated to give the desired GDD function $d^2\psi/d\omega^2$. If the resonator length is tuned appropriately, the lock is placed on an appropriate resonance and the dispersion function $\psi(\omega)$ does not vary too wildly, the spectrometer does not need to have high resolution as $\tilde{\psi}(\omega)$ can be made very slowly varying. Especially a resolution

²⁵and, especially important for very high finesse resonators, make sure that no "rational" resonance with $\omega_r/\omega'_r = k/l$ is present. This can e.g. be done by checking the coupling efficiency.

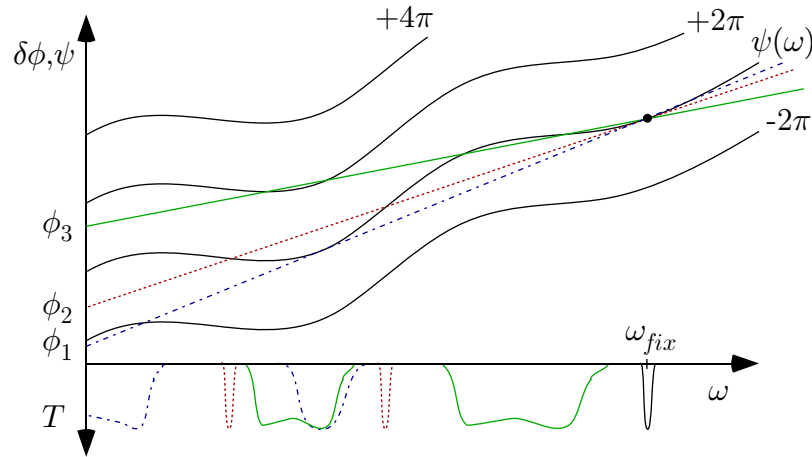


Figure 3.14: Illustration of the meaning of equation (3.75). On the positive vertical axis the left hand side (i.e. $\psi(\omega) - 2j\pi$) of (3.75) is plotted in black and the right hand side is shown for different values of the intercept $\delta\phi = k\phi_{CE} - \phi'_{CE}$ is shown in grey, dotted and dash-dotted respectively. On the negative vertical axis a sketch of the corresponding relative transmission T of the resonator is shown with corresponding line styles. Maxima in T are observed where the right and left hand side coincide.

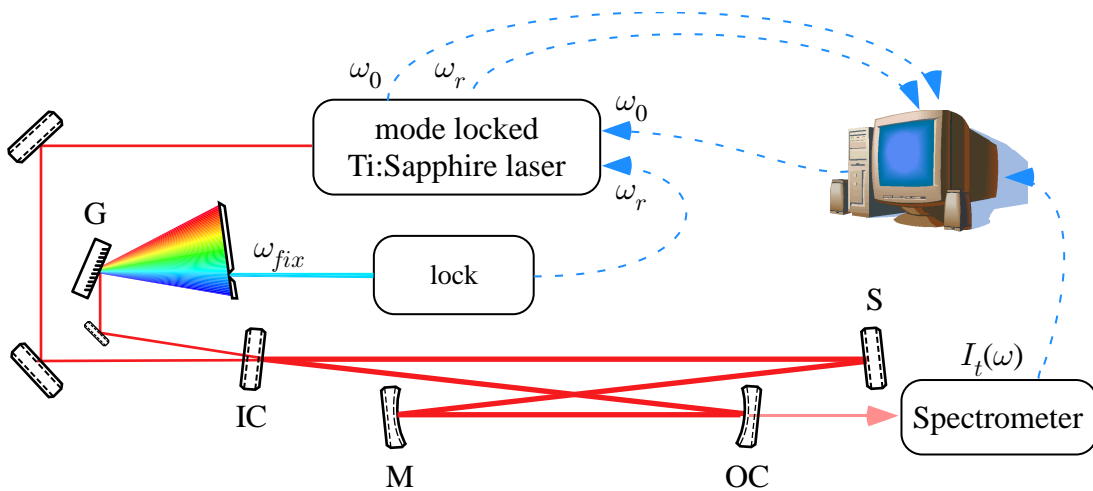


Figure 3.15: Intracavity dispersion characterization setup. The frequency comb from a mode-locked laser is sent to a resonator. The reflected beam from the input coupler (IC) is filtered around ω_{fix} using a grating (G) and a slit and an error signal is generated to electronically feed-back onto the laser repetition rate and keep the resonator on resonance in that range. Offset frequency ω_{CE} is tuned, and ω_r, ω_{CE} and $I_t(\omega)$ are recorded by a computer. S indicate places where sample mirrors may be placed.

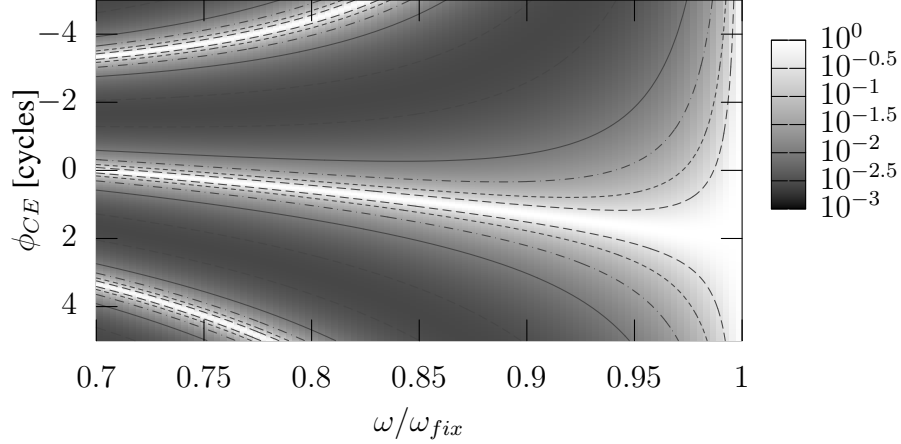


Figure 3.16: Transmission of a lossless (i.e. $T = 1 - R$) resonator of finesse $\mathfrak{F} = 10\pi$, driven by a mode-locked laser whose repetition frequency is constrained by (3.74) that maintains resonance condition at ω_{fix} , as a function of optical frequency ω and offset frequency $\phi_{CE} = 2\pi\omega_{CE}/\omega_r$. In each slice of this function at fixed ω sharp peaks are observed for certain values of $\phi_{CE}(\omega)$.

of ω_r is absolutely unnecessary. As long as the observed transmission patterns (at fixed ϕ_{CE}) are broader than the spectral resolution, the instrument's point spread function essentially has no influence on the result. As the resonance condition at ω_{fix} is forced by the electronic feedback loop, the transmitted intensity at this point will not change as the offset frequency is tuned. Indeed the round trip phase change as a function of pulse to pulse phase shift ϕ_{CE} is

$$\frac{d\tilde{\psi}}{d\phi_{CE}} = \frac{\omega_{fix} - \omega}{\omega_{fix}}, \quad (3.77)$$

so that it is convenient to locate the anchor point ω_{fix} as far away from the spectral region of interest as possible to reduce the required scanning range.

3.2.5 Mirror reflectance measurement

Another important aspect, apart from dispersion, of optics for broadband optical resonators for mode-locked lasers are losses. It was shown earlier that the maximum power enhancement inside a resonator is equal to the inverse of the net round trip loss in the resonator. When aiming for enhancement factors of 1000 and more as in this work, this means that every intracavity element's loss has to be on the order of 10^{-4} in order not to make the loss larger than 10^{-3} per round trip. Mirror reflectivities so close to unity are usually hard to measure directly by, e.g. shining light onto the mirror and measure how much is reflected.

A common and well know technique to determine small absorption (scatter, transmission) losses with high accuracy is cavity ring down spectroscopy (O'Keefe and Deacon 1988). The

basic idea of this method is to place the object under study into the mode of an optical resonator of high finesse. If the round trip loss due to the object is comparable to or larger than the round trip loss of the resonator, a significant reduction in resonator finesse may be observed. So if it is possible to determine the finesse of the resonator with and without the sample the (small) absorption of the sample may be determined. If the round trip loss of a resonator is on the order of 10^{-4} or even smaller, it becomes hard to determine the resonator finesse by measuring the resonance width compared to the free spectral range, as suggested by (3.34), because of the steady state condition for which (3.34) is valid. Steady state here means that the spectral bandwidth of the driving field is much smaller than the width of one resonance, i.e. $\Delta\omega \ll \Delta\omega_{FWHM}$ and that the resonator is sufficiently stable in effective length. All the calculations for passive resonators performed so far in this work assumed a time independent round trip gain G , but as G depends on the resonator length, it is coupled to acoustic and thermal fluctuations of the environment. Therefore we need to find a criterion under which conditions a time dependent G is sufficiently slowly varying as to fulfill the steady state condition that is assumed for all statements in section 3.2.1.

If we assume that there is a circulating electric field $E_c(t)$ inside the resonator whose spectral content (i.e. Fourier transform) is narrow enough that dispersion may be neglected (i.e. $\delta\omega \ll 2\sqrt{\pi}/\phi_2\mathfrak{F}$ as in (3.59)) and centered at ω_c , the electric field inside the resonator after one (group) round trip time of the resonator T_r will be given by

$$E(t + T_r) = rE(t)e^{i\psi_0} \quad (3.78)$$

with ψ_0 as in (3.48) and $r = r(\omega_c)$ assumed to be constant across the spectrum of the field. If there is no driving field coupled to the resonator, the circulating power after n round trips is obtained by iterating (3.78) and taking the square modulus of the result

$$I(t + nT_r) \propto |E(t + nT_r)|^2 = r^{2n}|E(t)|^2 := |E(t)|^2 e^{-(nT_r)/\tau} \quad (3.79)$$

and an exponential decay of the circulating field may be observed. The decay constant τ is related to the round trip reflectance via

$$R := r^2 = e^{-\frac{T_r}{\tau}} \approx 1 - \frac{T_r}{\tau}, \quad (3.80)$$

with the last approximation valid in the low loss, high finesse limit. This decay constant sets the time scale on which the resonator system can respond to changed conditions, i.e. for example a length change of the resonator so that it moves out of resonance or into resonance and still show steady state response, i.e.

$$\frac{dL}{dt} \ll \frac{\lambda}{\mathfrak{F}\tau} \approx \frac{\lambda 2\pi}{\mathfrak{F}^2 T_r}, \quad (3.81)$$

with λ being the driving field wavelength and the high finesse limit being used for the second form. For a Fabry-Perot resonator with a free spectral range $\omega_{FSR} = 2\pi \times 3$ GHz (i.e. 5 cm length) and a finesse of $\mathfrak{F} = 10^4\pi$, the decay constant is about 3 μ s and for the steady state condition to hold true, the laser has to be narrower than 300 kHz and the length of the resonator may

not change faster than $\dot{L} \ll 30 \mu\text{m/s}$, parameters which already require some effort concerning acoustic and thermal isolation.

On the other hand, the quantity of interest here (i.e. the round trip reflectance R of the cavity) is already contained in (3.80). So if this decay constant can be measured, the cavity loss can be determined too, without the necessity to determine the steady state resonance width of the resonator. No resonance conditions have been employed to derive (3.79) and therefore the requirements on the stability of the resonator length are only determined by the requirement that a change in length does not significantly change T_r in (3.80). Therefore the method for determining the finesse of a low loss resonator usually follows the procedure: the resonator is driven by a (relatively, compared to the expected scale on which R changes) narrow band source, centered at ω_c . Once a certain threshold of circulating power in the resonator is achieved (high enough to observe a clear decay signal leaking through one of the mirrors of the resonator), the driving field is quickly (faster than the decay time τ) shut off and the resonator decay ("ring down" hence the name of the method) is recorded to determine $\tau(\omega_0)$. The only requirements that have to be fulfilled to make the method usable are a sufficiently strong transmission signal to observe the decay and the ability to switch off the source quickly. The first requirement usually means that the driving source is not too broadband (compared to the cavity resonance width, it doesn't have to be narrower though) and sufficiently mode matched. A grating stabilized diode laser (Ricci et al. 1995, and references therein) can provide a relatively clean mode with MHz bandwidth without too much hassle, so this is relatively simple to achieve. The second condition means typically, a switch working on the ns time scale is required. This can be achieved using Pockels cells though it is a little bit demanding. Therefore a method was developed during this work²⁶ to avoid the use of a fast switch and still determine the decay constant of a resonator, which will be described in the following.

The steady state response of a high finesse resonator (i.e. circulating or transmitted intensity) varies rapidly with resonator length as may be seen from the fact that the intensity ratio of the steady state circulating field on resonance and out of resonance (just between two resonances) is about $4\mathfrak{F}^2$. Therefore already a relatively slow length change may trigger a non-steady state-transition of the resonator. This should exhibit the decay constant τ . Therefore, the idea is to sweep the resonator length across a resonance sufficiently fast so that such a transient may be seen and the resonator decay constant can be extracted. However, because the driving field is still on during the transition, the signal leaving the resonator (circulating power multiplied by mirror transmittance) does not have the simple form as in (3.79) but exhibits some oscillation due to interference between the stored and the driving field. Therefore it is necessary to model the scanning resonator driven by a constant frequency field to see how to extract the resonator lifetime from such a signal.

Let's consider a resonator, consisting of two mirrors as depicted in figure 3.17, where the input mirror M_1 with complex transmission and reflectance amplitudes $t_1(\omega), r_1(\omega)$ respectively at the fixed position $x = 0$ and mirror M_2 moving at constant velocity $x_2(t) = vt$ and having (rest frame) amplitudes $t_2(\omega), r_2(\omega)$. Between the mirrors shall be vacuum, so that the complex

²⁶Later it was found, that there exists a publication by An et al. (1995) that treats the same problem in a similar way.

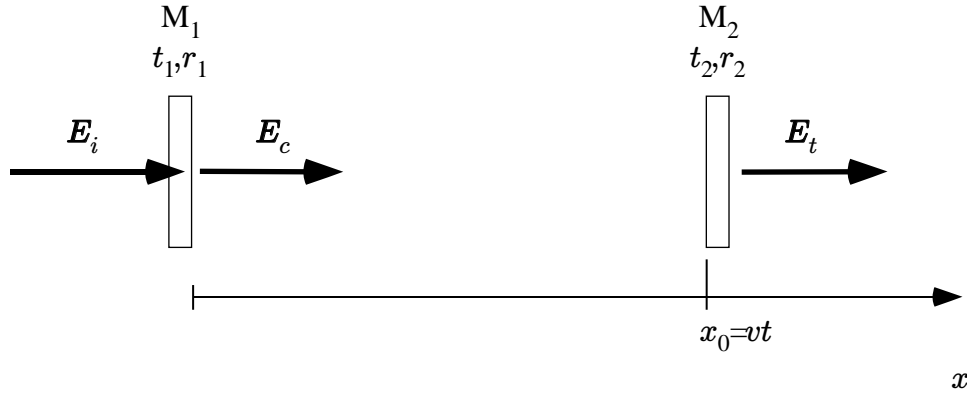


Figure 3.17: Simplified scheme of a scanning Fabry-Perot cavity with incident wave E_i , that gets transmitted through mirror M_1 with transmission t_1 and reflection r_1 , circulating wave E_c that bounces back and forth between the mirrors and gets transmitted through mirror M_2 , which moves at velocity v . E_t : transmitted wave.

field amplitude of the forward travelling wave $E_c(t, x)$ may be expressed in terms of its Fourier components

$$E_c(t, x) = \frac{1}{\sqrt{2\pi}} \int \hat{E}_c(\omega) e^{i(\omega t - kx)} d\omega \quad (3.82)$$

and $k = \omega/c$ obeys the vacuum dispersion relation. The associated reflected wave from mirror M_2 , has to be calculated in the mirrors rest frame. To do that, let's perform a Lorentz boost

$$ct' = \gamma(ct - \beta x) \quad (3.83)$$

$$x' = \gamma(-\beta ct + x), \quad (3.84)$$

where $\beta = v/c$ and $\gamma = (1 - \beta^2)^{-1/2}$. Upon this boost, each plane wave transforms into the boosted version

$$e^{i(\omega t - kx)} \mapsto e^{iu(\omega t' - kx')}, \quad (3.85)$$

where $u = (1 - \beta)\gamma$ is the Doppler shift. As the moving mirror is at rest in the boosted frame at $x' = 0$ the reflected plane wave in this frame is

$$e^{i(\omega t' - kx')} \mapsto r_2(u\omega) e^{iu(\omega t' + kx')}, \quad (3.86)$$

and has acquired the phase and amplitude of the mirror. An inverse boost yields the laboratory frame reflected wave

$$r_2(u\omega) e^{iu(\omega t' + kx')} \mapsto r_2(u\omega) e^{iu^2(\omega t + kx)}. \quad (3.87)$$

which is then transformed by mirror M_1 into a forward direction plane wave. Therefore the electric field after one round trip through the resonator is given by

$$\tilde{E}_c(t, x) = \frac{1}{\sqrt{2\pi}} \int r_1(u^2\omega) r_2(u\omega) \hat{E}_c(\omega) e^{iu^2(\omega t - kx)} d\omega = \quad (3.88)$$

$$=: \frac{1}{\sqrt{2\pi}} \int \tilde{\hat{E}}_c(\omega) e^{i(\omega t - kx)} d\omega. \quad (3.89)$$

From this one can see immediately that the spectrum is transformed by one cavity roundtrip, using again vacuum dispersion relation

$$\hat{E}_c(\omega) \mapsto \tilde{\hat{E}}_c(\omega) = \frac{1}{u^2} r_1(\omega) r_2 \left(\frac{\omega}{u} \right) \hat{E}_c \left(\frac{\omega}{u^2} \right) + t_1(\omega) \hat{E}_i(\omega), \quad (3.90)$$

where we added the transmitted portion of the Fourier transform of the incident field $\hat{E}_i(\omega)$. The factor $1/u^2$ is the result of the transformation of the spectral density $\hat{E}_c(\omega)d\omega$ by the variable substitution $u^2\omega \mapsto \omega$.

As the Fourier transform uniquely determines the field for all times, the notion "before or after one round trip" has no meaning for this function, whatsoever. Therefore the only sensible choice for the circulating spectrum is such that "before" and "after" is identical. Similar to (3.28) the condition

$$\hat{E}_c(\omega) = t_1(\omega) \hat{E}_i(\omega) + \frac{1}{u^2} r_1(\omega) r_2 \left(\frac{\omega}{u} \right) \hat{E}_c \left(\frac{\omega}{u^2} \right), \quad (3.91)$$

has to be imposed. The solution to this equation can simply be found by iterating (3.91). If $r_1(\omega)r_2(\omega/u) = r = \text{const}$, $t_1(\omega) = t_1 = \text{const}$ is assumed, the solution takes the form

$$\hat{E}_c(\omega) = t_1 \sum_{n=0}^{\infty} E_i \left(\frac{\omega}{u^{2n}} \right) \left(\frac{r}{u^2} \right)^n. \quad (3.92)$$

In the simplest case, where the driving field is a monochromatic wave $\hat{E}_i(\omega) = E_{i0} \delta(\omega - \omega_0)$ with frequency ω_0 , $\delta(\omega)$ being the Dirac delta distribution, the circulating spectrum is

$$\hat{E}_c(\omega) = t_1 E_{i0} \sum_{n=0}^{\infty} \delta(\omega - u^{2n} \omega_0) r^n, \quad (3.93)$$

where the identity $\delta(ax) = (1/a)\delta(x)$ was used. The inverse Fourier transformation of this spectrum yields the forward travelling complex field amplitude $E_c(t, x)$. For sake of simplicity, from now on the spatial coordinate will be set to zero, so that all fields are evaluated at mirror M_1 . Then the circulating field amplitude becomes

$$E_c(t) = \frac{1}{\sqrt{2\pi}} t_1 E_{i0} \sum_{n=0}^{\infty} r^n e^{i\omega_0 u^{2n} t}. \quad (3.94)$$

Depending on the parameters r and u , this may have a very complex shape as a function of time. However, we shall now be interested in the case where the velocity of the mirror is small and therefore u is close to unity. Let us therefore expand u^{2n} into a Taylor series in β

$$u^{2n} = 1 - 2n\beta + \frac{1}{2}(2n\beta)^2 - \frac{2}{3}n(1 + 2n^2)\beta^3 + \mathcal{O}(\beta^4). \quad (3.95)$$

For very small velocities (to be specified later) it is sufficient to keep only the first two terms in (3.95) and then $E_c(t)$ may be directly summed to yield

$$E_c(t) \approx t_1 E_{i0}(t) \sum_{n=0}^{\infty} r^n e^{-i2n\beta\omega_0 t} = \frac{1}{\sqrt{2\pi}} \frac{t_1 E_{i0} e^{i\omega_0 t}}{1 - r e^{i2\beta\omega_0 t}}, \quad (3.96)$$

with $E_0(t) = \frac{1}{\sqrt{2\pi}} t_1 E_{i0} e^{i\omega_0 t}$. This looks identical to (3.29) with $\omega L/c$ replaced by $2\beta\omega_0 t$. This means that one may observe peaks in the circulating field power, identical in shape to those shown in figure 3.7 (only as a function of time instead of frequency) with positions $t_n = n\pi/\omega_0\beta$ (assuming now r to be real, otherwise there will be a time offset t_0 that may be subtracted), that is when the separation of the mirrors is $x_n = x(t_n) = vt_n = n\lambda/2$ as expected for a resonator that operates close to steady state.

If we now take the next higher order contribution to u^{2n} into account, and offset time to the time where the m^{th} quasistatic resonance would appear $t = t_m + t'$, then the exponent in (3.94) takes the form

$$\omega_0 u^{2n} t \approx \left(-2n\beta + \frac{1}{2}(2n\beta)^2 \right) \omega_0 t = -2nm\pi + 2(n\beta)^2 \omega_0 t_m + (-2n\beta + 2(n\beta)^2) \omega_0 t'. \quad (3.97)$$

If we now additionally assume that $|t'| \ll t_m$, if we look for example around the 10000th longitudinal resonance, then the term $2(n\beta)^2 \omega_0 t'$ can be neglected²⁷ compared to $2(n\beta)^2 \omega_0 t_m$ and the electric field amplitude at $t_m + t'$ can be approximated by

$$E_c(t_m + t') \approx E_0(t_m + t') \sum_{n=0}^{\infty} r^n e^{i(2\pi n^2 m\beta - 2n\beta\omega_0 t')}. \quad (3.98)$$

As the amplitudes of the contributing components in the sum drop exponentially as r^n , the sum converges after $N = -1/\ln r$ steps. this shows, that the steady state approximation (3.96) is valid as long as $N^2 m\beta \ll 1$. With the realization that $\mathfrak{F} = -\pi/\ln r$ in the high finesse limit, the steady state condition becomes $v \ll \pi^2 \lambda / \mathfrak{F}^2 T_r$, which is consistent with (3.81) (up to some factors of π). If we now further assume that $2N\beta m \ll 1$ and $|2\beta\omega_0 t'| \ll 2\pi$ (no rephasing), so that the phase changes only little between adjacent terms in the sum in (3.98), we may approximate the sum by an integral²⁸

$$E_c(t_m + t') \approx E_0(t_m + t') \int_0^{\infty} \frac{d\omega}{2\beta\omega_0} r^{\frac{\omega}{2\beta\omega_0}} e^{i\left(\frac{\omega^2 t_m}{2\omega_0} - \omega t'\right)}, \quad (3.99)$$

with the substitution $\omega = 2n\beta\omega_0$, which can be evaluated to yield

$$E_c(t_m + t') \approx E_0(t_m + t') \sqrt{\frac{i}{8\beta m}} e^{g^2(t')} (1 + \operatorname{erf}(g(t'))) \quad (3.100)$$

$$g(t') = \sqrt{\frac{-i}{8\pi\beta m}} \left(2\pi \frac{\omega_0 \beta t'}{\pi} + i \ln r \right). \quad (3.101)$$

²⁷strictly speaking, because the phase of an oscillatory function is approximated, it is also required, that $2(n\beta)^2 \omega_0 t' \ll 2\pi$ for all relevant terms in the fourier sum. Indeed it turns out, that this is the case for the validity range of the second order Taylor expansion in (3.95).

²⁸The continuum approximation will not exhibit the quasiperiodic structure that appears when the scan is extended over many resonances. The "no rephasing" condition means that we stay so close to one resonance that the adjacent resonances do not lie in the interval.

The square modulus of $E_c(t_m + t')$, corresponding to the circulating intensity in the resonator, is shown in figure 3.18. It can be split into two factors. The first is the square modulus of the exponential term in (3.100) which is explicitly given by

$$\exp\left(\frac{\omega_0 \ln(r)t'}{2\pi m}\right) = \exp\left(\frac{2 \ln(r)t'}{T_r}\right) = \exp\left(-\frac{t'}{\tau}\right) = \exp\left(-\frac{\pi t'}{\mathfrak{F}T_r}\right) \quad (3.102)$$

which exhibits the decay²⁹ time introduced in (3.79). The last form, which contains the finesse, is valid in the high finesse limit only. The second factor in (3.100) contains the complex error function erf defined as

$$\text{erf}(z) = \frac{2}{\sqrt{\pi}} \int_0^z e^{-z'^2} dz'. \quad (3.103)$$

The argument of it in (3.100) as a function of t' describes a straight line close to the $\sqrt{-i}$ diagonal of the complex plane, offset by the non vanishing contribution of $\sqrt{i} \ln r$. For vanishing $\ln r$, this term is a Cornu spiral (also termed Fresnel integral) and its square modulus is plotted for this case in figure 3.19. It has an asymptote for $\sqrt{\beta/\pi m \omega_0 t'} \gg 1$ given by (using an appropriately normalized time)

$$|1 + \text{erf}(\sqrt{-i}t)|^2 \approx 4 + \frac{1}{2t^2} + \frac{2}{t} \sin\left(t^2 - \frac{\pi}{4}\right). \quad (3.104)$$

The small contribution of $\ln r$ to $g(t)$ adds an exponentially growing oscillatory term to the square modulus. However this additional term has zero average and can be neglected in amplitude as long as $t' \ll -\frac{2m\beta}{\ln r} \ln \sqrt{\frac{m\beta}{2\pi}}$. Therefore the exponential decay time may be extracted from such a transmission by averaging over the oscillatory part of the pulse and fitting an exponential function to the tail of the pulse starting after say the second oscillation or so.

If we now require, that the signal has not dropped by more than $1/e$ at the second fringe of the oscillating envelope, in order to be able to get a good estimate of the decay constant, then the minimum scan speed is determined by

$$-\frac{\ln r}{\sqrt{8\beta m \pi}} = 1. \quad (3.105)$$

The circulating intensity can be observed behind the mirror M_2 . If the reflected intensity is accessible, this may also be used for measuring the photon lifetime of the cavity: The reflected intensity is given by the square modulus of the reflected incident wave plus the circulating wave transmitted through the mirror M_1 , i.e.

$$\begin{aligned} I_r(t_m + t') &= | -r_1 E_i(t_m + t') + t_1 E_c(t_m + t') |^2 = \\ &= \left(I_0 R_1 + T_1 I_c(t_m + t') + I_0 2 \text{Re} \left(r_1 t_1^2 \sqrt{\frac{i}{8\beta m}} e^{g^2(t')} (1 + \text{erf}g(t')) \right) \right) \approx \\ &\approx I_0 \left(1 + 4 \text{Re} \left(r_1 t_1^2 \sqrt{\frac{i}{8\beta m}} e^{g^2(t')} \right) \right), \quad \sqrt{\frac{\beta}{\pi m}} \omega_0 t' \gg 1 \end{aligned} \quad (3.106)$$

²⁹note that $\ln r$ is negative.

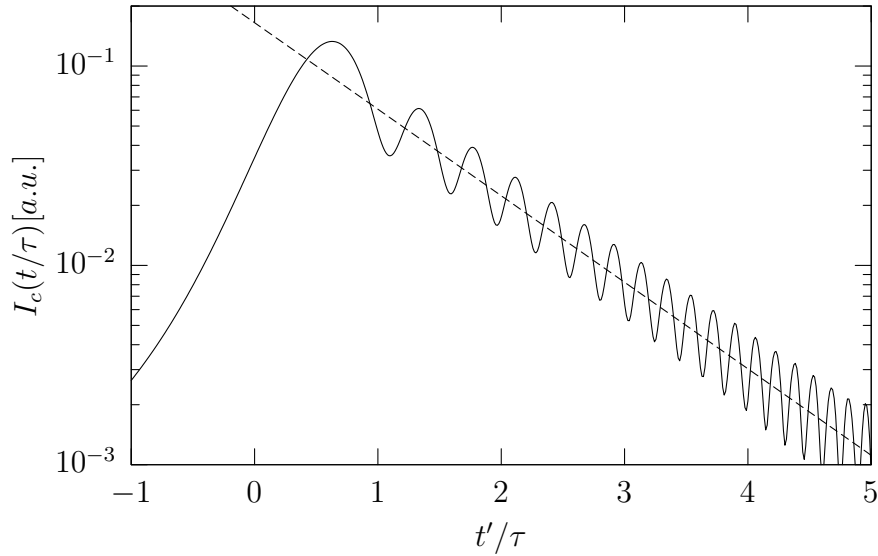


Figure 3.18: Square modulus of the circulating field (i.e. power) versus time normalized to the cavity lifetime τ (solid). $t' = 0$ is where the steady state fringe is expected. β is chosen such that the first oscillation lies within one decay time. An exponential decay as $\exp(-t'/\tau)$ is shown as a dashed line.

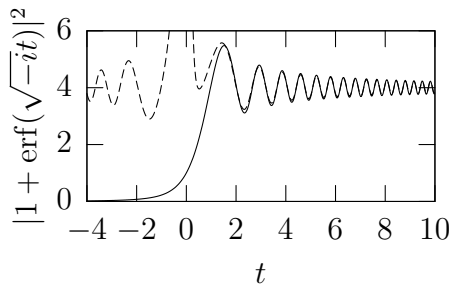


Figure 3.19: Square modulus of the Fresnel integral of (3.100) (solid, $r = 1$) and its asymptote as in (3.104) (dashed) using an appropriately normalized time.

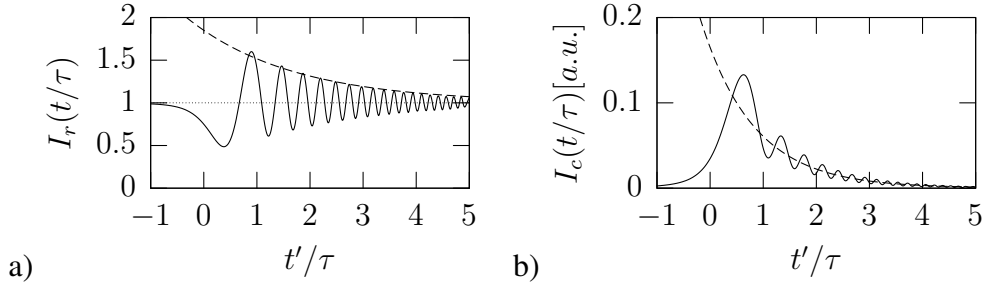


Figure 3.20: a) Reflected non steady state intensity (solid) normalized to ingoing intensity as a function of time normalized to decay time. The dashed line shows an exponential according to $1 + \exp(-t'/2\tau)$. Note that the decay time is twice as large as the resonator decay time τ . b) same plot as in 3.18 on linear scale for comparison. $t' = 0$ is the time where the steady state maximum is expected.

where $I(\omega_0) \propto |E_i(\omega_0)|^2$ is the incoming intensity, R_1 and T_1 the reflectance and transmittance of the mirror M_1 respectively and $I_c(t_m + t')$ is the square modulus of $E_c(t_m + t')$. For writing down the approximated version for large times in the second line of (3.106), the approximations $1 + \text{erf}(g(t')) \approx 2$ and $R_1 I_0 + T_1 I_c(t_m + t') \approx I_0$ (energy conservation) which should be fulfilled on average³⁰, were made. With

$$\exp(g^2(t')) = \exp\left(\frac{\ln r}{T_r} t' + i \frac{\ln^2 r}{8\beta n \pi} - i \left(\frac{\omega_0^2 \beta t'^2}{2\pi n}\right)\right) \quad (3.107)$$

one can quickly see (figure 3.20) that for large t' , $I_r(t')$ will perform damped oscillations with a damping constant twice as large as in the transmitted case and a linearly increasing frequency. The resonator damping constant can be extracted from this by taking half the damping constant of the oscillation.

Summarizing this section, the decay constant of a resonator may be measured not only by driving the resonator and then quickly switching off the drive, but is also observable when scanning the resonator across a resonance with a velocity much larger than in (3.81). Then in transmission after a peak, an exponential decay with a superimposed oscillation is observed. The decay time is the resonator decay time τ defined in (3.79) which relates to the round trip reflectance via (3.80) from which in turn the resonator finesse can be calculated via (3.34). The scan speed is high enough if the oscillations are clearly offset from zero (i.e. don't go down to zero), otherwise the drive completely cancels the stored oscillation, driving it up again afterwards, which increases the effective decay time. If the observations are made in reflection, an exponentially decaying oscillation around the off-resonant reflected intensity can be seen, stemming from interference between the Doppler-shifted stored light and the driving field. The decay constant is twice the resonator decay time τ (as the interference intensity is proportional to the stored *field* instead of the intensity). Looking at the reflection has the advantage that the decay

³⁰This is of course not true at any instant of time, as the resonator can store Energy for a certain amount of time and moreover will transmit half of the energy inside the resonator through mirror M_2 .

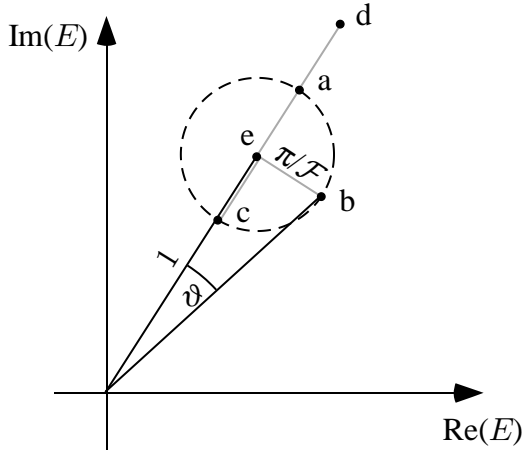


Figure 3.21: Phasor diagram of the normalized circulating field. a: steady state (Field $E_c = E_i \sqrt{\mathfrak{F}/\pi}$), e: after one round trip (without drive), field has dropped by a factor (π/\mathfrak{F}) , b: $\pi/2$ phase jump, c: π phasechange, d: amplitude doubled

time is longer and therefore the decay is observable with smaller scanning speeds. The transmitted intensity function has the advantage, that the decay is not only in the oscillating signal but in an offset as well. Therefore it will still be visible even if the driving radiation is broader in bandwidth than the steady state resonance. This is not true for the reflected signal, as the phase of the oscillation will be different for each driving component (because resonance occurs at different times), and therefore the signal will be washed out by a broadband driving field.

3.2.6 Resonators as noise filters

As explained in the section 3.1.3, there are quite a few mechanisms that convert amplitude and phase noise of the fundamental frequency comb into phase noise in the upconverted frequency comb in the XUV. For this reason, special measures have to be taken to provide a low noise fundamental frequency comb for the conversion so that the XUV frequency comb is not buried in broad band noise. In this section it will be shown that the use of a (sufficiently stable) enhancement resonator may improve the noise properties of the driving frequency comb.

In an impedance matched resonator of finesse \mathfrak{F} , the input coupler has a transmission of π/\mathfrak{F} , while on resonance in steady state the circulating field power is \mathfrak{F}/π stronger than the driving field. Therefore, if the driving amplitude or phase changes from one round trip to the next (in the mode-locked case, possibly from one pulse to the next), as illustrated in figure 3.21, the amplitude of the circulating field can at most change by a factor $2\pi/\mathfrak{F}$ (phase jump of π), and the phase (in a high finesse limit) may change by π/\mathfrak{F} (phase jump of $\pi/2$). Pure intensity noise can change the circulating amplitude (again round trip to round trip) by at most by a factor π/\mathfrak{F} if amplitude change from one pulse to the next is restricted to 100%, i.e. dropping to zero or doubling from the average value. In intensity (amplitude squared) the change is even smaller, on the order of $(\pi/\mathfrak{F})^2$. Of course, fluctuations that happen on a slower time scale, have a larger impact on the circulating field. That is in the other extreme, where the phase and amplitude changes are on a time scale long compared to the photon decay time (3.80), the stored field follows all changes adiabatically.

From these considerations, one can learn that the resonator effectively acts as a low pass fil-

ter on phase and amplitude fluctuations in the driving field (that don't have the same period as the resonator). In the frequency domain this fact can be seen immediately by looking at the response spectrum of the resonator (see 3.7): If the driving comb is tuned on resonance, that is, the comb modes are centered on resonance peaks, noise frequency components between these comb modes are suppressed. Pulse to pulse changes in amplitude or phase correspond to frequency components just in the middle between two comb teeth. These components are suppressed by $1/(2\mathfrak{F})^2$ in intensity, which is consistent with the considerations from the preceding paragraph. For slower fluctuations, the corresponding Fourier components lie closer to the comb teeth and the suppression is reduced until the noise component frequency is much smaller than $\omega_{FSR}/\mathfrak{F}$ where the full component is resonant and the circulating field follows adiabatically. The cutoff frequency of the lowpass is therefore $\omega_{FSR}/\mathfrak{F}$ and stopband suppression is $1/(2\mathfrak{F})^2$. Moreover, a servo that locks the driving laser to the resonator can significantly suppress noise components that are within the servo bandwidth, so that the low frequency components that are not suppressed passively by the resonator may be strongly reduced by an appropriate feedback loop.

Of course the given analysis only considers a time-independent resonator without dispersion. A real resonator will have moving mirrors due to acoustic vibrations and thermal expansion. These will even add phase noise to the pulse train (at the target). So, special attention is required to minimize acoustic and thermal fluctuations of the resonator.

3.2.7 "Solitonic" resonators

During the implementation of an enhancement resonator for fs laser pulses, it was found that one of the biggest difficulties was to have a resonator that was well compensated in terms of dispersion. On the other hand, mode-locked lasers, to a very high accuracy (Udem et al. 1999a), emit a periodic pulse train, so that the spectrum of that pulse train forms a frequency comb. This means that the pulse circulating in the laser resonator has the same shape, round trip after round trip and the effective dispersion in the resonator has to be exactly zero. The existence of such steady state operation is due to a complicated interplay between resonator dispersion and several nonlinearities in the resonator. In Kerr-lens mode-locked lasers, the dominant nonlinearities are the gain of the laser medium, the self amplitude modulation provided by self focusing and the self phase modulation, both occurring in the laser medium. The latter effect is well known from nonlinear fiber propagation to provide a soliton wave equation, which has a solution that does not change its shape during propagation and is stable against perturbations.

From that observation, the idea arose that introducing an appropriate nonlinearity in an enhancement resonator for fs pulses, could provide a similar mechanism, so that it becomes possible to achieve an increased bandwidth of the cavity and thereby higher circulating peak powers compared to a resonator with the same dispersion and no nonlinearity. As there is no gain medium in the resonator, and as it is known (Chen et al. 1999) that the most important nonlinear effect for sub-50 fs mode-locked lasers pulse shaping is self phase modulation (SPM), a resonator was modeled (and simulated numerically), that in addition to dispersion included self phase modulation. This work was published by Kalashnikov et al. (2005).

In detail the model used was a distributed model where the dispersion and SPM nonlinearity was distributed uniformly across the entire length of the resonator. It leads to a driven nonlinear

Schrödinger equation

$$\begin{aligned} & i \frac{\partial A(x, t)}{\partial x} - \frac{\phi_2}{2} \frac{\partial^2 A(x, t)}{\partial t^2} - i \frac{\phi_3}{6} \frac{\partial^3 A(x, t)}{\partial t^3} + \frac{\phi_4}{24} \frac{\partial^4 A(x, t)}{\partial t^4} + \delta_{NL} |A(x, t)| A(x, t) = \\ & = \Delta\phi_{CE} A(x, t) + i\Delta T \frac{\partial A(x, t)}{\partial t} - i\gamma A(x, t) + i \operatorname{sech}(t)^{1+i\rho}, \end{aligned} \quad (3.108)$$

which describes the propagation of an ultra short pulse (with complex field envelope $A(x, t)$) within a resonator with effective round trip phase

$$\tilde{\psi} = \Delta\phi_{CE} + \Delta T(\omega - \omega_0) + \frac{1}{2}\phi_2(\omega - \omega_0)^2 + \frac{1}{6}\phi_3(\omega - \omega_0)^3 + \frac{1}{24}\phi_4(\omega - \omega_0)^4. \quad (3.109)$$

with $\Delta\phi_{CE}$, ΔT , ϕ_2 , ϕ_3 and ϕ_4 being the pulse to pulse carrier phase change difference, the round trip delay mismatch, GDD, third and fourth order dispersion respectively. The round trip loss is modeled by the factor γ , the driving pulse was modeled to be a sech function with chirp ρ . The strength of the Kerr nonlinearity is given by δ_{NL} . In writing down equation (3.108), the time t was implicitly normalized to the pulse duration, x to the resonator round trip length and the intensity to the driving pulse power. All parameters have to be normalized accordingly.

For a numerical study of such a resonator, the damping parameter was chosen in agreement with the existing setup (see section 4.1) round trip damping to be 1%, i.e. $\gamma = -\ln(1 - 0.01)$. Now for different values of the dispersion parameters ϕ_3 and ϕ_4 , a global optimization of the remaining free parameters of the model $\Delta\phi_{CE}$, ΔT , ϕ_2 , and δ_{NL} with respect to peak power was performed. To compare the results to the case without nonlinearity the same optimization was performed while fixing δ_{NL} to zero, effectively switching off the nonlinearity during that run. This optimization corresponds quite well to an experimental scenario where $\Delta\phi_{CE}$ and ΔT are controlled optimally using electronic feedback. ϕ_2 can be controlled using either atmospheric pressure in the resonator, or the thickness of the Brewster plate, that is inserted into the resonator to control the SPM coefficient δ_{NL} . δ_{NL} may then be controlled by moving the plate with respect to a focus, thereby changing the beam cross section in the plate.

The resulting optimized peak powers are shown in figure 3.22. In these plots it is clearly observable that the parameter range for which an enhancement of more than 95 may be achieved is much larger in the nonlinear case than in the linear one. A remarkable fact is that in the nonlinear case the maximum achievable peak power enhancement is higher than for the impedance matched linear case. This is due to the fact that the SPM broadens the circulating spectrum, which is then compressed by the dispersion. In that way the circulating power is concentrated in a shorter pulse than the driving pulse, resulting in higher peak power. Of course the spectral overlap between the driving pulse and the circulating pulse becomes worse in that case, so that arbitrarily short pulses can not be created.

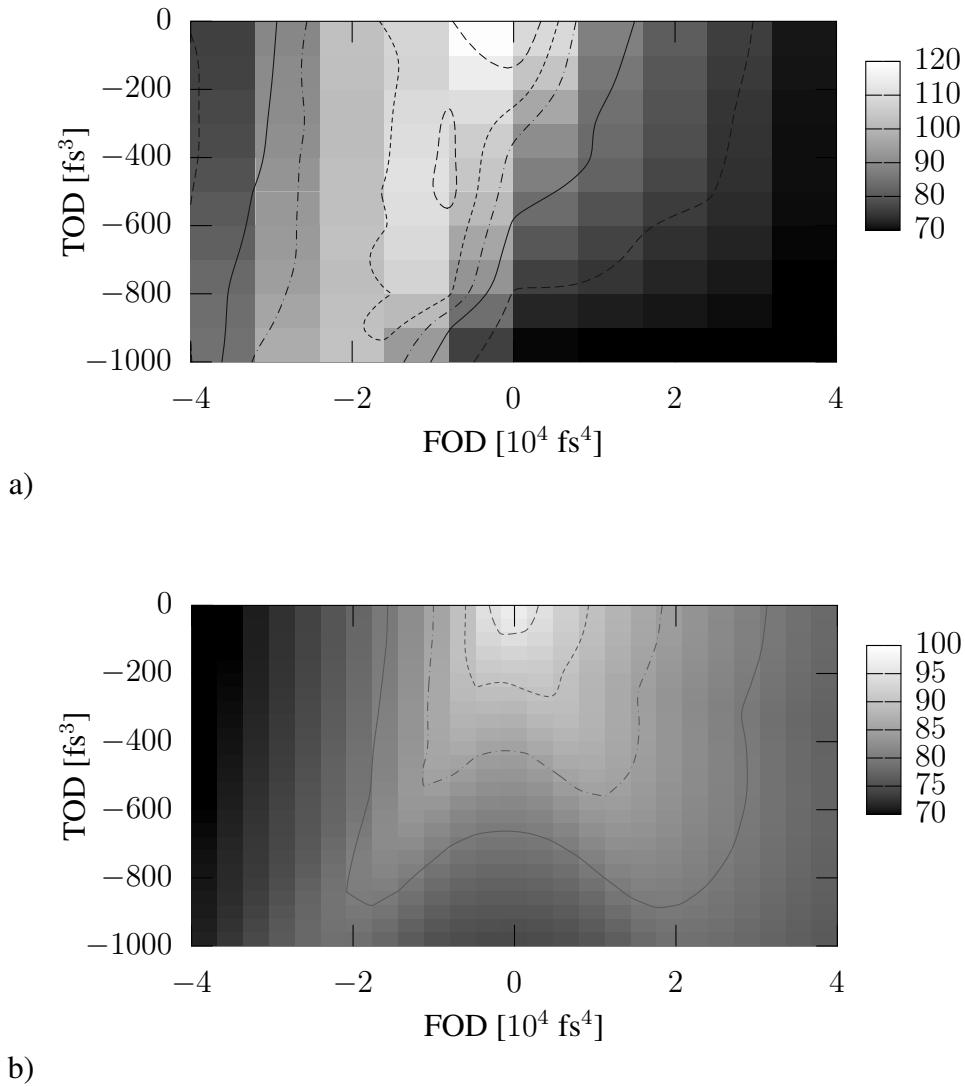


Figure 3.22: Optimized peak powers for the a) nonlinear and b) the linear case. The area including an peak power enhancement factor of 95 or larger, is clearly larger in the nonlinear (dash-dotted contour) than in the linear case (long dashes). Also remarkable is the fact that in the nonlinear case the circulating peak power can be higher than in the linear case.

Chapter 4

Experimental realization of an XUV frequency comb

4.1 Implementation of a fs-enhancement resonator

Section 3.2 discussed the prerequisites for enhancement resonators for broadband frequency comb light. To implement such a resonator in the real world, some technical issues have to be addressed and design decisions have to be made to build a system that satisfies the experimental requirements. In the following sections, a system designed for generating a frequency comb source in the extreme ultraviolet, that can be used for high resolution spectroscopy, including all the necessary components, will be described. An overview of the setup is given in figure 4.1.

The first sections will describe the laser system that was used to drive the resonator. Then it will be explained how the resonator is constructed so that the resonator mode profile enables maximal intensity at a focus in the mode and how the driving laser's mode profile is matched to that resonator mode to maximize the coupling efficiency. This follows a description of the mechanism controlling the temporal shape of the driving electric field as to minimize the pulse duration of the stored (enhanced) pulse inside the focus of the resonator mode in order to maximize the peak power of the pulse. To make the resonator work (in the intended way) it is also necessary to maintain the resonance condition between driving field and resonator. The electronic feedback loop that takes care of that will be explained. Finally an overview over the employed diagnostic methods will be given and operational parameters of the complete system will be shown.

4.1.1 The laser system

The laser system employed in this work is a commercial Kerr-lens mode-locked Ti:Sapphire laser¹ (Femtolasers FS20). It consists of a Ti:Sapphire crystal as a gain medium, pumped by a frequency doubled Nd:YVO₄ laser (Coherent Verdi) that delivers an output power of 5.5 W. The pump radiation is focused into the gain medium to produce inversion there. A schematic of the laser resonator that is built around the gain medium is shown in figure 4.2. It is a linear resonator

¹see for example in the work of Kasper (1997) for an overview on these type of lasers.

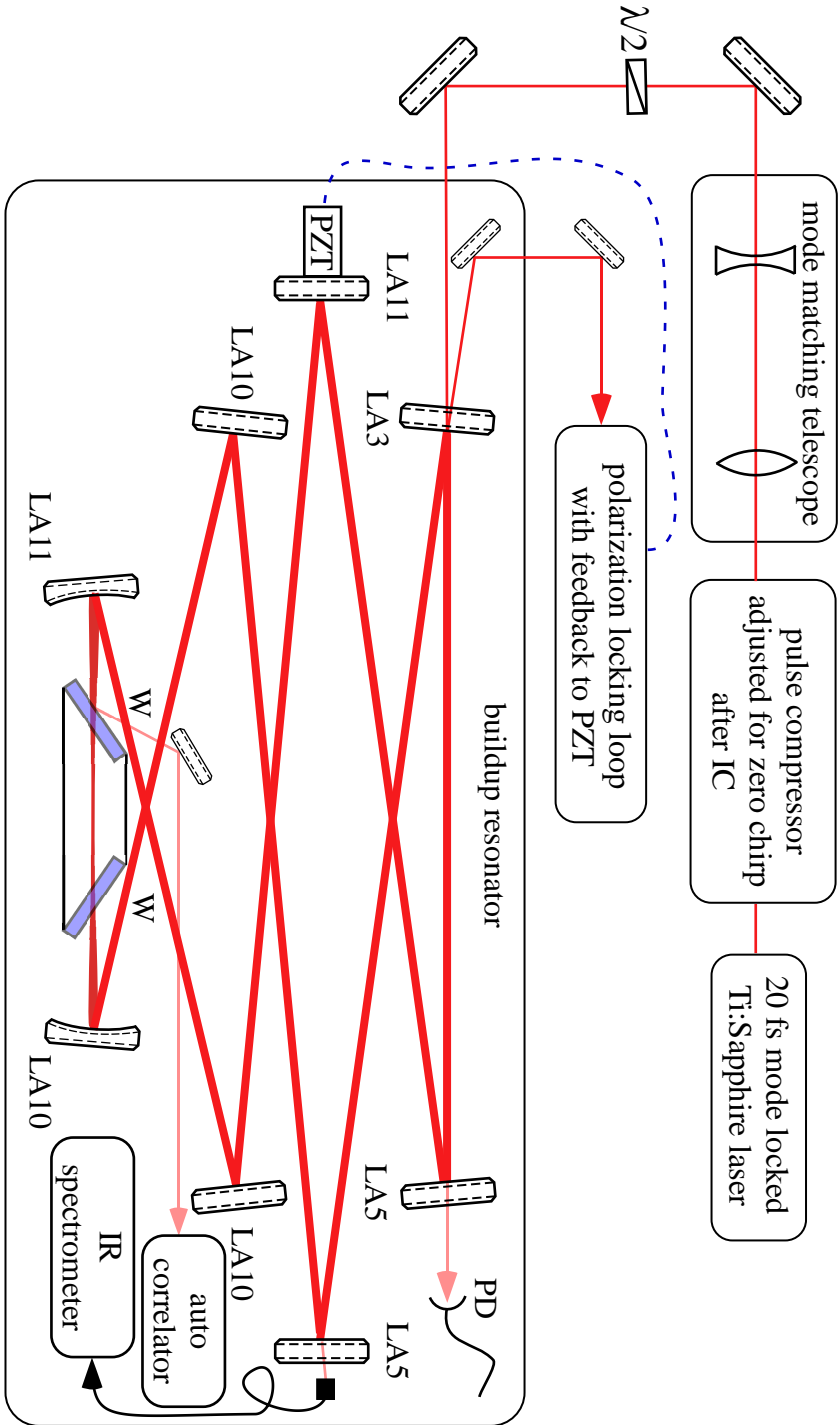


Figure 4.1: An overview over the setup developed in this work. Components are described in detail in the corresponding subsections. Legend: LAX: different mirror types (internal numbering). refer to 4.6 for details, PD: photodiode, W: vacuum Brewster windows, PZT: piezoelectric transducer

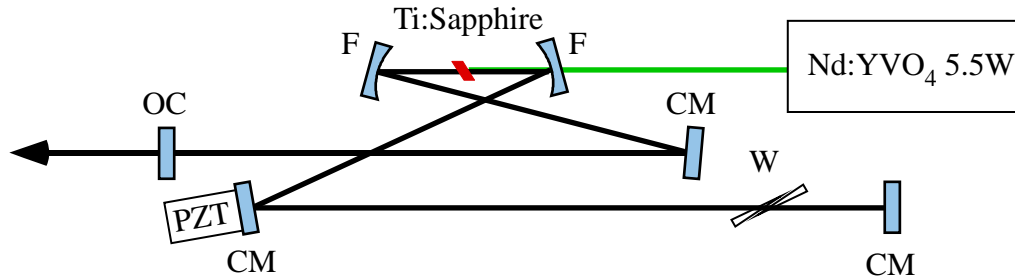


Figure 4.2: Schematic of the laser system. Nd:YVO₄: frequency doubled pump laser 5.5 W at 532 nm, Ti:Sapphire: laser gain medium, F: focusing mirrors 25 mm focal length, CM: chirped plane mirrors, OC: output coupler, PZT: piezoelectric transducer for controlling resonator length, W: fused silica wedges to control the carrier envelope offset frequency.

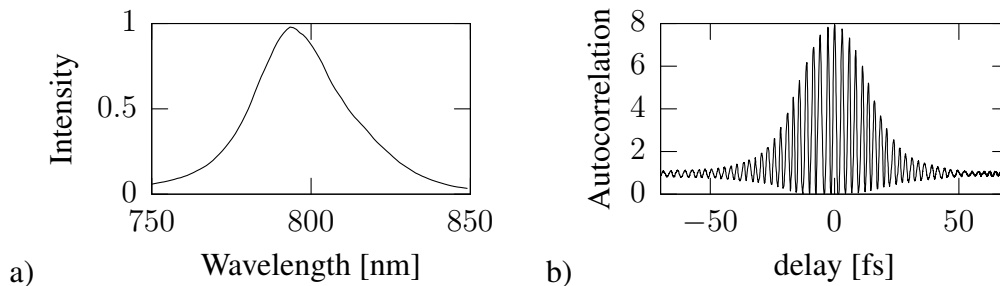


Figure 4.3: a) Typical output spectrum of the laser system with a FWHM width of 30 nm centered at 795nm. b) Measured interferometric autocorrelation trace corresponding to a pulse duration of about 20 fs.

that has two 25 mm focal length spherical mirrors that create a tight focus in the resonator mode inside the Ti:Sapphire crystal to make the mode overlap with the pump laser mode, to maximize gain. There are two "collimated" arms in the resonator with unequal length. The length of these arms as well as the folding angle between the focused arm and the two collimated arms is determined in order to enable and optimize Kerr-lens mode locking. These arms also contain plane folding mirrors with specially designed coatings to provide the negative dispersion necessary for the mode locking of the laser and one end mirror in each arm. The end mirror of one arm is partially transmitting to couple the laser radiation out of the laser resonator. In the other collimated arm one of the folding mirrors is mounted on a piezo electric transducer for electronic control of the resonator length and thereby the repetition rate. Additionally this arm contains a pair of thin wedges made from fused silica that allow fine adjustment of the dispersion inside the resonator that enables control of the carrier envelope offset frequency of the laser.

The laser produces about 850 mW average output power with a mode locked repetition rate of 114 MHz, a center wavelength of 793 nm and a pulse duration of 20 fs. A typical spectrum and autocorrelation trace of the laser output is shown in figure 4.3.

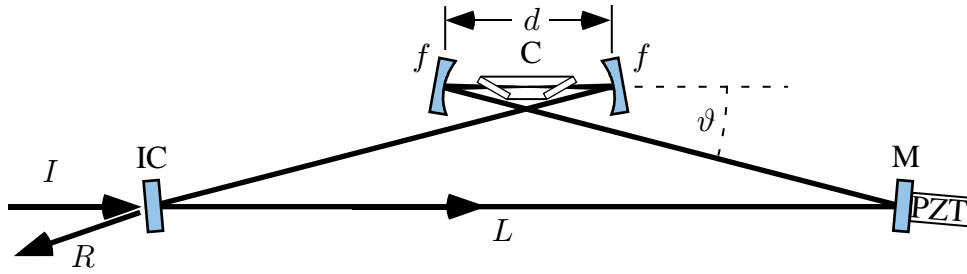


Figure 4.4: Sketch of the bowtie resonator design. A ring resonator with a long "collimated" arm of length L (starting from the left focusing mirror f through mirror M and IC to the right focusing mirror) and a "focused" arm of length d between the two focusing mirrors with focal length f . The folding angle between the focused and collimated arm is ϑ . IC is the input coupler through which the driving field is coupled to the resonator. M is a piezo (PZT) mounted mirror to control the resonator length electronically. Note that there is also a reflected beam R from IC in addition to the driving beam I , which is used to create an error signal for the electronic feedback. The target is placed in the focused arm. Frequently this is a nonlinear medium for second or third harmonic generation. In our case it is a vacuum chamber that contains the nonlinear medium and is sealed by Brewster windows.

4.1.2 Resonator mode and mode matching

A common design for enhancement resonators in nonlinear optics is the so-called bowtie resonator, which is sketched in figure 4.4. A ring resonator is used as this simplifies the separation of the beam reflected from IC from the incoming beam, which is useful for generating an error signal for electronic feedback on cavity length (or laser repetition rate) and laser offset frequency. The bowtie resonator design makes it possible to produce a very tight focus between the focusing mirrors and still have a large round trip length (long round trip time) to match up with the laser repetition rate, which is necessary as discussed in section 3.2.2. The focused arm contains the nonlinear medium. In our case this is a noble gas jet placed inside a vacuum chamber that is sealed with Brewster-angled windows made from sapphire. Brewster-angled windows are chosen as this provides a simple means of minimizing reflection losses on the windows while maintaining a large optical bandwidth.

To appropriately choose the focal length f of the focusing mirrors, the folding angle ϑ and the distance between the focusing mirrors, the resonator mode has to be calculated and the parameters have to be adjusted to meet the requirements. This was done using the "ABCD" matrix formalism for Gaussian beams, that may be found in the work of Kogelnik and Li (1966). This formalism is capable of treating diffractive optics (in the paraxial approximation) using a simple 2×2 matrix formalism. Such a resonator has a stable mode only if the separation between the focusing mirrors d is within certain limits, that will be called the stability range. For a bowtie resonator this is a single interval in the mirror separation with upper and lower stability limits. The above mentioned paper only considers the cylindrically symmetric case, whereas in our case this symmetry is broken by the focusing mirrors that are used at an angle and the Brewster windows. However, as long as the planes of incidence for both are parallel, the problem boils down to two

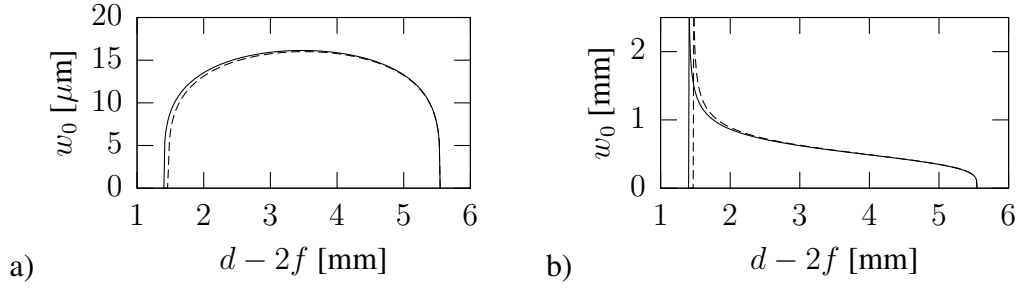


Figure 4.5: a) Focused arm focus size for $f = 50$ mm, $L = 2.53$ m and window thickness $d_{00} = 1$ mm (two windows). The upper stability limits of sagittal and tangential plane coincide for a folding angle $\vartheta = 10.34^\circ$. b) Collimated arm focus size for the same parameters (solid lines: sagittal plane, dashed: tangential plane). For symmetry reasons these foci lie in the center of the respective arms.

decoupled mode equations for the beam in the plane of incidence (tangential plane) and the plane that contains the mode axis and is perpendicular to the plane of incidence (sagittal plane). The effective focal length of the focusing mirrors is given by

$$\begin{aligned} f_s &= f / \cos \vartheta \\ f_t &= f \cos \vartheta \end{aligned} \quad (4.1)$$

in the sagittal and tangential planes respectively. The effective optical path through the Brewster windows with refractive index n is given by

$$\begin{aligned} d_{0s} &= d_0/n \\ d_{0t} &= d_0/n^3, \end{aligned} \quad (4.2)$$

where d_0 is the geometrical path through the window of thickness d_{00} given by

$$d_0 = d_{00} \sqrt{(1 + n^2)/n^2}. \quad (4.3)$$

By choosing the folding angle of the resonator appropriately, the upper (or lower) stability limits of the sagittal and tangential plane can be made to coincide. Then the resonator mode remains essentially circular when approaching the upper (lower) stability limit so that the achievable focal size is only limited by the aperture size of the focusing mirrors. Figure 4.5 shows the focus sizes ($1/e$ amplitude radius w_0) in the focused and collimated arm as a function of focusing mirror separation for a resonator with the parameters $f = 50$ mm, $L = 2.53$ m to match the repetition rate of the laser, $d_{00} = 1$ mm and a folding angle $\vartheta = 10.34^\circ$. It can be seen, that at the chosen folding angle, the upper stability limit for sagittal and tangential plane coincide so that when approaching this limit from below, the focus size in the focused arm shrinks without bound. Of course in this calculation, finite aperture sizes have been neglected and at some point the beam diameter at the focusing mirrors will exceed the size of the mirrors, so that effectively the minimal focus size is limited by the numerical aperture of the focusing mirrors.

Now that the resonator mode is known, in order to maximize the coupling efficiency, the laser mode has to be matched to the resonator mode. For this purpose, we have to transform the laser beam (using lenses) to have the same focus size and position as the resonator mode. For this purpose a telescope consisting of a focusing lens ($f = 150$ mm) and a defocusing lens ($f = -50$ mm) were used and the position and separation of these were optimized, using ABCD matrix formalism, to image the focus of the laser mode at the output coupler onto the focus of the resonator mode in the middle of the resonator's collimated arm.

4.1.3 Dispersion control and losses

The vacuum windows, the air as well as the dielectric mirrors produce non-negligible dispersion in the resonator. This dispersion has to be compensated for, as discussed in section 3.2.2. The method of choice for this purpose is dispersive dielectric mirrors. These can provide tailored dispersion across the entire laser spectrum while keeping the loss low. The drawback of this type of dispersion control is that the dispersion is not continuously adjustable as in the case of prism- or grating-based systems. Such systems however exhibit a relatively large intrinsic loss, which is intolerable in the context of enhancement resonators, where the maximum achievable enhancement factor is the inverse of the round trip loss.

The net dispersion of the resonator, excluding mirrors, is given by the dispersion of air (10.64 fs²/m at 793 nm) inside the resonator and the sapphire vacuum windows (58.99 fs²/mm at 793 nm). Therefore the total GDD due to these contributions is 164 fs² per round trip. It is not possible to compensate such a dispersion with a single dispersive mirror, as the dispersion achievable with a single mirror with sufficient bandwidth is around -40 fs². Therefore, it is necessary to have several (4-5) reflections off dispersive mirrors per round trip. For this reason the collimated arm of the resonator is folded six times. This gives a total of 8 reflections per round trip, which in turn allows a few mirrors not to be dispersive, so that they can be optimized by other means. For example the mirror IC has a spectrally flat transmission, which is usually not the case for dispersive mirrors, to achieve a spectrally homogeneous impedance-matched coupling.

Production tolerances of the mirror coating layer thicknesses lead to dispersion properties deviating from the design goal; therefore several different coatings have been produced and used in the resonator. Each of these have been characterized in terms of their dispersion properties using either of two white light interferometers developed in the work of Nebel (Tobias 2005) or one developed by Takao Fuji at our Institute, which works similar to what was published by Knox et al. (1988). The results are summarized in figure 4.6. The mirror "LA17" is included in this figure as to show that quite some improvement in reflectivity has been achieved in the collaboration with the coating company, by using super-polished substrates. When the contributions of air, the windows and all the mirrors are summed up, where empirical formulas for the sapphire (Malitson 1962) and air (Bonsch and Potulski 1998) refractive index were used, the total dispersion is close to zero. Figure 4.7 shows dispersion data of the cavity using a zero dispersion input coupler with coupling of 1% similar to LA3, two mirrors of type LA5, two mirrors of type LA11 (one of them on a 1/4" substrate mounted on the piezoelectric transducer) and three LA10 mirrors.

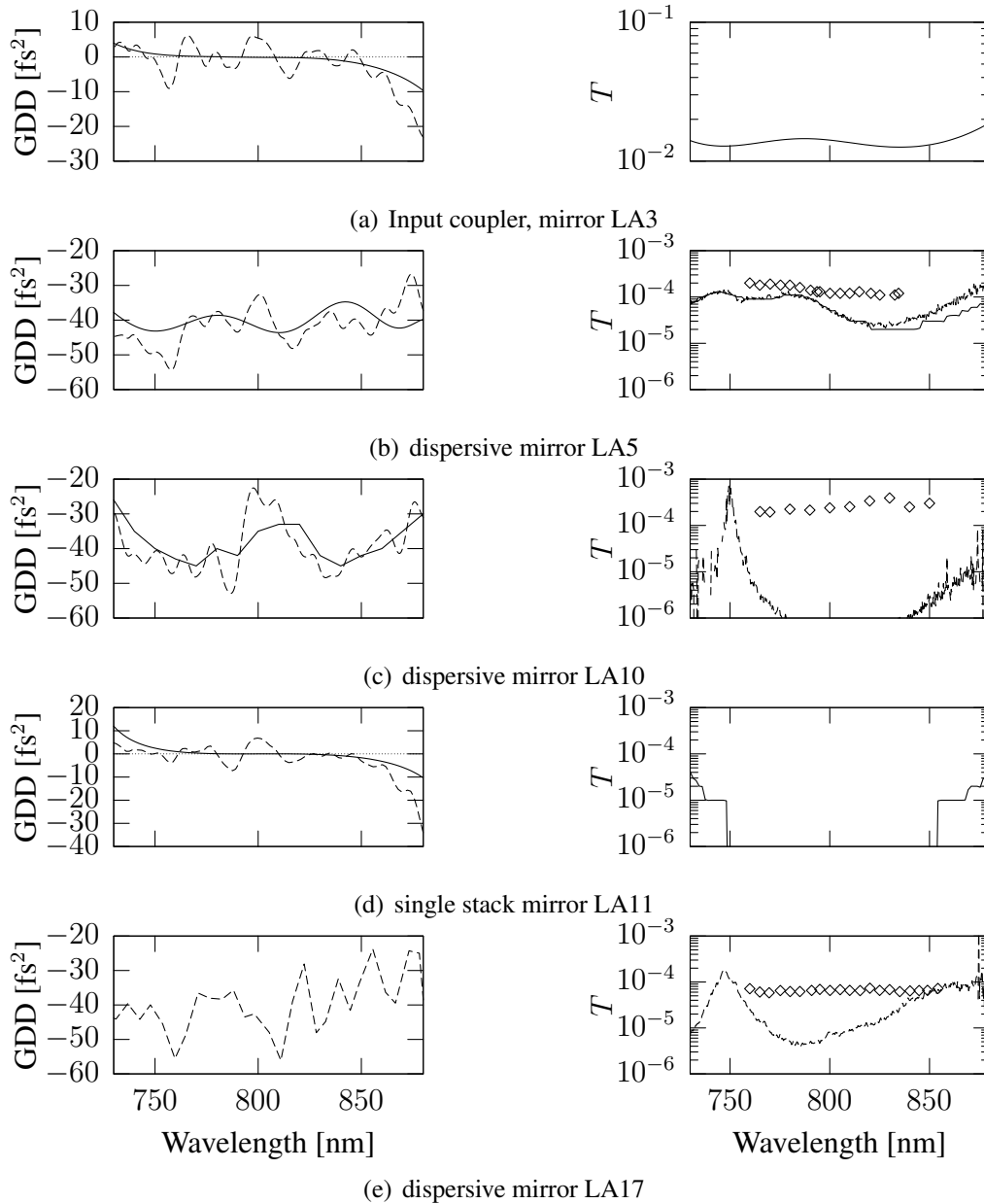


Figure 4.6: Dispersion and transmission (T) data for some of the mirrors used in the enhancement resonator. Solid curves correspond to design curves (where available), dashed are measured dispersion (using the white light interferometer described in the work of Nebel (Tobias 2005)) and transmission respectively. Diamonds show $1 - R$ where R is the measured reflectance obtained using the method described in section 3.2.5. Exceptions to these are figure 4.6(c) where the reflectance was determined by measuring the finesse (i.e. steady state resonance width) and figure 4.6(e) where the dispersion was measured using a scanning white light interferometer designed by Takao Fuji. The difference between T and $1 - R$ are additional losses due to absorption and scattering.

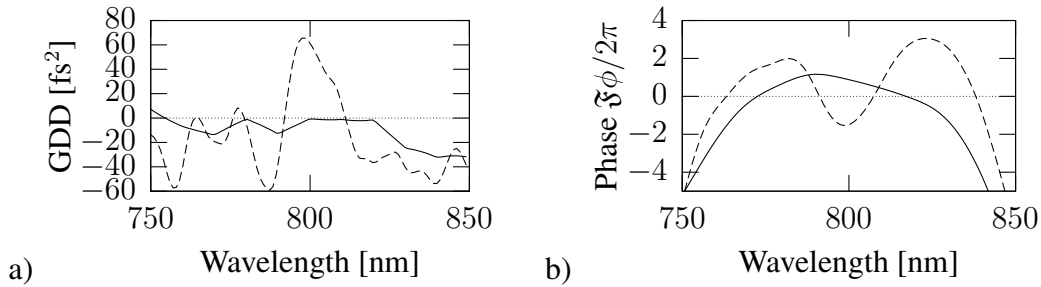


Figure 4.7: Round trip a) GDD and b) phase for the resonator (2.671 m air, 2.3 mm sapphire, one LA3, two LA5, three LA10 and two LA11) that was built during this work. Solid lines show the sum of the design curves and dashed is the sum of measured dispersion properties. The finesse assumed for scaling the phase is $\xi = 100\pi$.

The sum of mirror losses excluding the input coupler is much smaller than 1%. Still it turns out that the resonator is nearly impedance-matched, from which it can be concluded that other losses dominate. A very probable candidate for these losses are reflection and scattering losses from the Brewster windows. Reflection losses come from the Brewster windows being in a strongly focused beam, so that Brewster's condition is only satisfied for one spot in the spherical wavefront. Therefore with optimized alignment, where that spot is in the center of the beam, an annular reflected beam can be observed, that is estimated to contain about 5×10^{-4} of the circulating power per surface, resulting in a total loss (four surfaces) of about 0.2%, a broad band loss that dominates all the other losses. Therefore, as the input coupler has a flat reflectance and the rest of the round trip losses are dominated by a flat loss from the Brewster windows, the resonator finesse is essentially flat across the wavelength range of interest and estimated to be 100π .

4.1.4 Temporal pulse shaping

To maximize peak power in the interaction region (in the focus of the resonator mode inside the vacuum chamber), a pulse compressor based on fused silica prisms was employed (see figure 3.12a). A double pass arrangement was used with a mirror at the symmetry plane. The distance between the Prism apexes was about 1.8 m. This was chosen such that GDD of the total beam path, including laser output coupler substrate, mode matching telescope, retarder plate and resonator input coupler substrate was compensated. The amount of prism material inserted into the beam was then optimized to first shorten the autocorrelator trace (see section 4.1.6) and later to maximize the XUV output.

4.1.5 Electronic feedback loop

The resonance conditions discussed in the sections 3.2.1 and 3.2.2 have to be fulfilled for the resonator to work as it should. As said in section 3.2.2, the effective round trip phase $\tilde{\psi}$ as in

(3.53) should be zero² for the entire spectral range of the driving laser, i.e. from 750 nm to 850 nm. Dispersion can not be easily controlled inside the resonator (if no programmable pulse shaper is inserted, which would have intolerably high losses). Therefore the only controllable parameters in $\tilde{\psi}$ are $\delta\omega_r$ and $\delta\omega_{CE}$ defined in (3.51), which may be controlled by changing laser cavity or enhancement resonator length (using the piezo-mounted mirrors) and laser dispersion (using the wedges inside the laser) respectively. Because $\omega_0 T'$ is a very large number (in our case $2\pi \times 375 \times 10^{12} / 114 \times 10^6 \approx 20 \times 10^6$) and a change in $\delta\psi_0$ of the order of $2\pi/\mathfrak{F} = 0.02$ causes a change from "on resonance" to "off resonance", the length of the resonator has to be controlled on the 10^{-9} level (i.e. a few nanometers in our case), which is not easily achieved in a passive manner³. Therefore an electronic feedback loop is employed to actively stabilize the resonator length. This electronic feedback is based on the polarization technique introduced by Hänsch and Couillaud (1980). This method uses the phase shift of the circulating field compared to the incident field (see figure 3.7) to create an error signal. The phase shift has a very high slope as a function of detuning, with a "zero" on resonance; therefore it can be used for making an offset-free feedback loop.

In more detail, the incident beam is slightly rotated in polarization using a half-wave plate, to contain a small amount of s-polarization (with respect to the Brewster window's plane of incidence). Then the part of this component reflected from the input coupler effectively experiences no phase shift due to the resonator because of low finesse and poor impedance matching of the resonator for s-polarization, whereas the reflected p-polarization component will be phase shifted by

$$\theta = \arg(r_1 E_i + t_1 E_c). \quad (4.4)$$

This phase shifted p-component adds to the unshifted s-component to give a circular component proportional to the phase shift. A circular polarization analyzer is used to extract the phase information and create an electronic signal accordingly. This signal is then fed into a proportional-integrator (PI) loop filter, whose output is amplified to drive a piezoelectric transducer to control the resonator length. In the setup described here the entire spectrum was polarization analyzed, so that the error signal was zero if the resonance condition was fulfilled on average (weighted by the power in the spectral components). This should maximize the total circulating power as a function of resonator length.

The other degree of freedom was not fed back electronically but optimized manually using the wedges in the laser resonator. It was stable enough to run the system for an hour or so without readjustment.

In a final version of the setup it would be desirable to electronically feedback both degrees of freedom. For that purpose, it is possible to use two different spectral components of the reflected beam to create two error signals, pass them through an orthogonalization matrix and feed those signals to wedges and resonator length. In such a setup, the best position of the two spectral components to lock on is determined by the dispersion of the resonator. For zero dispersion any pair will do the same job.

²or an integer multiple of 2π of course

³Thermal expansion coefficients are typically on the order of $10^{-6}/\text{K}$, so that thermal isolation on the mK level would be required, not to mention acoustic isolation.

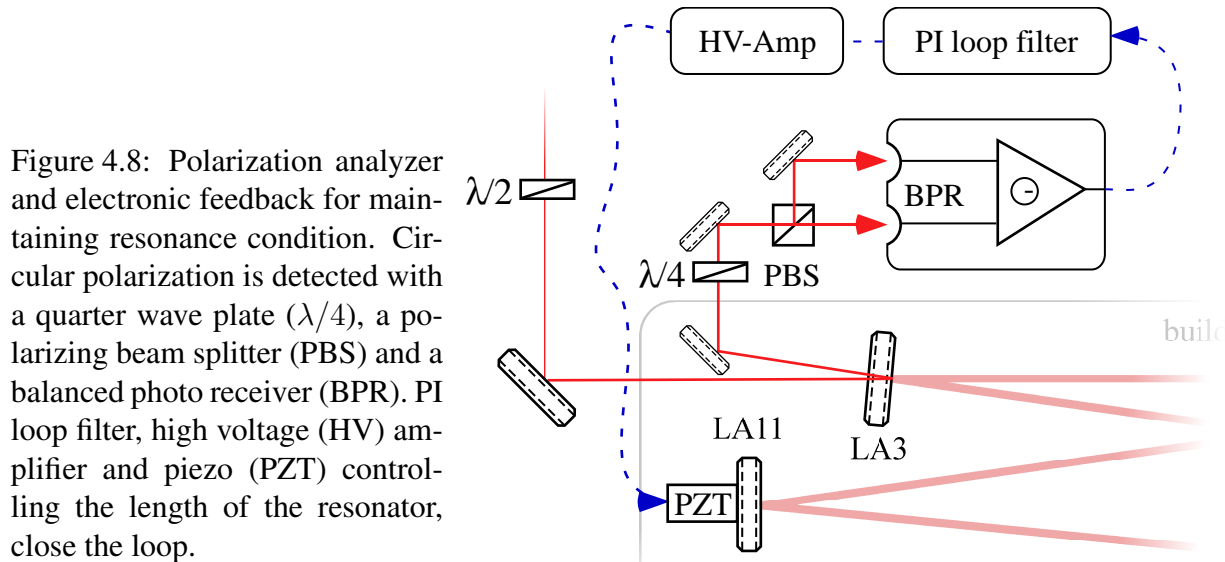


Figure 4.8: Polarization analyzer and electronic feedback for maintaining resonance condition. Circular polarization is detected with a quarter wave plate ($\lambda/4$), a polarizing beam splitter (PBS) and a balanced photo receiver (BPR). PI loop filter, high voltage (HV) amplifier and piezo (PZT) controlling the length of the resonator, close the loop.

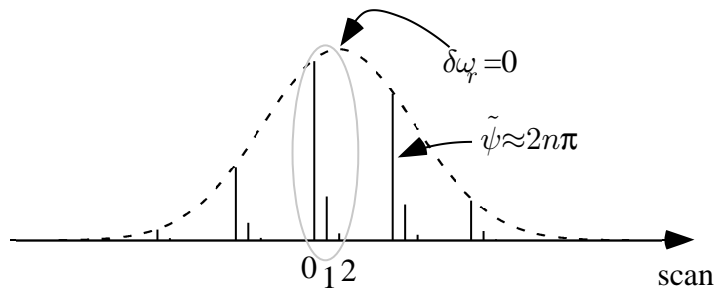


Figure 4.9: Cartoon of the photodiode signal that may be observed once coarse alignment is performed. The groups of resonances (vertical lines) correspond to $\delta\omega_{CE} = 0$ and different resonances in that group (designated by 1,2 and 3) to different transversal modes. The envelope (dashed) over the groups has a maximum at $\delta\omega_r = 0$. The width of the envelope gives a hint on the resonant bandwidth and resonator finesse.

4.1.6 Diagnostics

To determine the operating parameters of the resonator, several different diagnostic tools were attached to the resonator. For the coarse alignment of the resonator, the spectrally integrated transmission through it was monitored using a photodiode while scanning the resonator length. A cartoon version of what signal can be observed on the photodiode vs. piezo voltage is shown in figure 4.9. This signal can be used to get information on mode matching, offset frequency matching and some first indication of the dispersion/finesse.

In this spectrally integrated signal, a peak is observed, whenever $\tilde{\psi}$ is close to an integer multiple of 2π across a major fraction of the incident spectrum. Changing the resonator length by one wavelength at the (center) frequency ω_c will change $\tilde{\psi}(\omega_c)$ by 2π and the resonance pattern repeats itself. Because changing the resonator length also changes $\delta\omega_r$, the slope of $\tilde{\psi}$ will vary. As a result, the size of the spectral region that can simultaneously resonant will also change. By

inspection of (3.53) it is quickly seen that it is largest, if $\delta\omega_r$ is close to zero. This means, that the periodic resonance structure acquires an envelope, which has a maximum at $\delta\omega_r = 0$. A resonance can be observe at this maximum only if $\delta\omega_{CE}$ also vanishes. For zero dispersion, it can easily be estimated that the envelope is approximately

$$l = \omega_c / 2\pi\Delta\omega\mathfrak{F} \quad (4.5)$$

resonance fringes wide. Here $\Delta\omega$ is the width of the laser spectrum. The shape of the envelope is of course dependent on the detected spectrum. If the dispersion is not zero, the envelope will be broadened. This broadening will be relevant once dispersion induces significant spectral filtering even for the condition $\delta\omega_r = \delta\omega_{CE} = 0$. For the case, where only GDD plays a role a criterion for that is that $\Delta\omega_{FWHM}$ as in (3.59) is comparable or smaller than the laser bandwidth $\Delta\omega$.

To get more information about the circulating spectrum and power, a simple commercial grating spectrograph (Ocean Optics S2000) was used to observe the transmitted spectrum behind one of the resonator mirrors (type LA5). The transmittance of that mirror was determined accurately so that the observed spectra could be normalized to yield the circulating spectrum. In conjunction with a pyroelectric power meter (Ophir model "2A-5H") behind the same mirror, the circulating power could be determined by first normalizing the observed spectrum to the transmitted total power and dividing it by the transmission curve of the mirror afterwards. The transmitted spectrum as a function of ϕ_{CE} was also used to determine the resonator dispersion, using the method discussed in 3.2.4.

To get some idea about the circulating pulse duration, autocorrelation measurements were performed using a simple autocorrelator (APE model "Micro"). As input for this device, the residual reflection from the first of the Brewster windows was used. There are two reflection, one from the outer (first) surface and one from the inner (second). To get as close as possible to the target (in terms of chirp), the inner reflection was used, collimated by a focusing chirped mirror which simultaneously compensated for the second passage through the window.

4.1.7 Results and discussion

In the following results obtained with the described setup will be shown. These results (including high order harmonic generation using the setup) have been described in an article that was published during this work in Nature (Gohle et al. 2005). Similar work has also been performed by Jones and Ye (2004), who switched the pulses out of the resonator using an acoustooptic modulator, after reaching steady state. In this way they obtained amplified pulses without using an amplifier.

When the feedback loop is turned on to lock the resonator to the highest resonance observed (the highest peak in figure 4.9) and the wedges in the laser are adjusted appropriately to move that resonance to the center of the envelope, so that the circulating power is maximized, a circulating spectrum as shown in figure 4.10a can be observed. After adjusting the prism compressor to minimize the autocorrelation signal duration, we observe an autocorrelation trace as shown in 4.10b. The total circulating power was determined to be 38 W on average, with 700 mW power just before the input coupler. This is an average power enhancement of 54, which compares

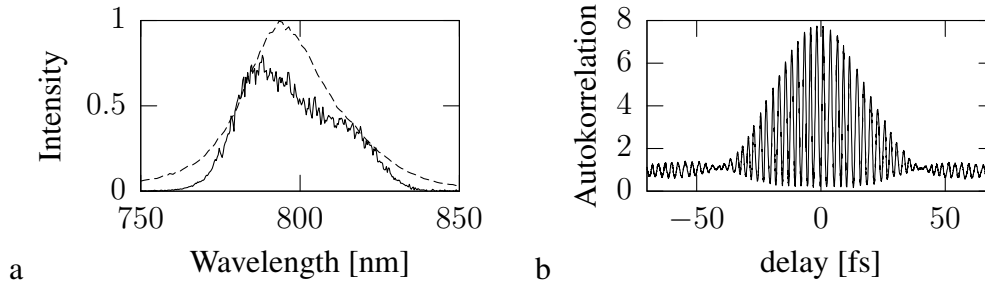


Figure 4.10: a: Locked resonator spectrum (solid) and driving laser spectrum (dashed), b: measured intracavity second-order autocorrelation shows a nearly Fourier limited pulse corresponding to 28 fs pulse duration if a sech pulse shape is assumed.

well to the impedance matched enhancement factor, which is 100 given the 1% coupling. The circulating pulse energy is then $E_0 = 38 \text{ W}/114 \text{ MHz} = 333 \text{ nJ}$.

The missing factor of two in the power enhancement can be almost completely attributed to spectral filtering due to residual dispersion. If we normalize the circulating power by the incident power (figure 4.11), a double peak structure is obtained. Because these two maxima are approximately of the same height and it is almost certain that the resonator finesse does not change much in the relevant spectral region, it is now sensible to assume that these two maxima correspond to points of zero effective round trip phase $\tilde{\psi}$. Then by attributing a power enhancement factor of 100 to these points in the spectrum and calculating the integral, we would arrive at about 48 W circulating total power with the given spectral filtering. The observed value is about 79% of the expected enhancement. If we now assume that this 79% is due to impedance and mode mismatch, the enhancement factor could be 79 for the same resonator without dispersion.

Due to spectral filtering, the observed autocorrelation trace has changed its shape compared to the laser pulse autocorrelation. It exhibits side lobes (stemming from the almost rectangular circulating spectrum) and a longer FWHM duration. If a sech pulse shape is assumed (which is obviously a not very good approximation), a FWHM pulse duration of 28 fs can be estimated from this autocorrelation trace, compared to 20 fs for the laser pulse. This increase in pulse duration leads to a reduction in power enhancement, if it is calculated as the circulating *peak* power compared to the driving peak power, instead of the average power. Then the peak power enhancement factor is about 38, i.e. a factor of 2 smaller than it could be without dispersion. The absolute peak power (assuming a Gaussian pulse with the given FWHM duration) is 11.2 MW.

The resonator was operated quite close to the outer stability limit and therefore the size of the focus inside the vacuum chamber was rather small. It was estimated by measuring the spot size of the (mode matched) driving laser beam on one of the focusing mirrors inside the resonator. It was determined to be $w = 2.4$, where w is the $1/e$ amplitude radius of the Gaussian mode at this spot, with a focal length of 50 mm and an almost collimated beam coming in (the other focus is more than 1 m away), the waist size is $w_0 = 5.3 \mu\text{m}$. In the focus, the peak intensity can therefore be estimated to be $2.5 \times 10^{13} \text{ W/cm}^2$.

As mentioned earlier in this section, spectral filtering is a dominant effect in the reduction

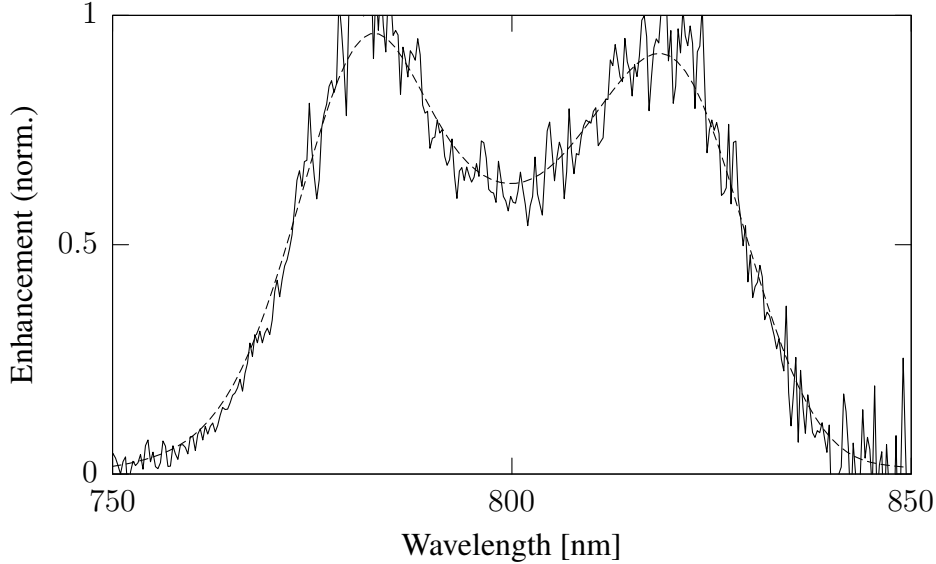


Figure 4.11: Circulating spectrum normalized to incident spectrum (solid) and an averaged version using Hanning low pass Fourier filter at $1/30$ of the data point resolution (dashed).

of the power enhancement of the demonstrated resonator. It especially prevents going to higher finesse resonators, as the dispersion will become more important then and the higher finesse will not lead to a higher peak power enhancement. To correct that, the dispersion inside the resonator has to be characterized accurately and an improved mirror design has to be employed. For this, the method described in 3.2.4 was employed. Figure 4.12 shows the transmitted spectrum normalized to the spectrum of the driving laser⁴ as a function of the lasers pulse to pulse phase slip $\phi_{CE} = \omega_{CE}/\omega_r$. During the acquisition of this data set, the resonator length was stabilized such that the driving laser was always resonant at 839.15 nm. This was achieved by filtering the light reflected from the resonator using a grating and a slit before it was fed to the polarization analysis of the feedback loop. For each column in the data matrix displayed in figure 4.12, corresponding to a fixed optical frequency ω , the position of the transmission maximum $\phi_{CE}(\omega)$ was determined. To do that, an Airy function (3.31) was fit to that column where the phase in the cosine function in the denominator of that expression was replaced by $(\omega/\omega_{fix} - 1)(k\phi_{CE} - \phi_{CE}(\omega))$. The fit model therefore reads

$$\frac{T(\omega)}{T_0(\omega)} = \frac{A(\omega)(1 - r(\omega))^2}{1 + r^2(\omega) + 2r(\omega) \cos\left(\frac{\omega - \omega_{fix}}{\omega_{fix}}(k\phi_{CE} - \phi_{CE}(\omega))\right)}. \quad (4.6)$$

Here k has to be taken to be one⁵ and the fit parameters are $A(\omega)$, $r(\omega)$ and $\phi_{CE}(\omega)$. As an example the data of one column at 770 nm and the resulting fit is shown in figure 4.13. The result of these fits is summarized in figure 4.14. From $\phi_{CE}(\omega)$ the round trip phase $\psi(\omega)$ and

⁴Actually the transmission through the resonator while blocking the resonator mode right after the transmitting mirror was used. In this way the transmission functions of the input and output coupler were readily taken care of.

⁵as the resonator has approximately the same length as the laser resonator.

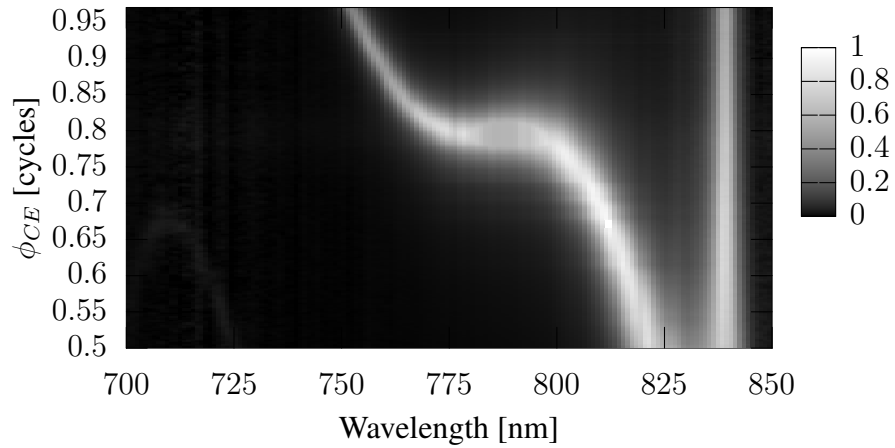


Figure 4.12: Spectrally resolved transmission of the resonator through one of the high reflecting mirrors as a function of the driving lasers pulse to pulse phase shift ϕ_{CE} . The transmission data was normalized by the driving laser spectrum to improve the visual display. This normalization is not necessary for analysis.

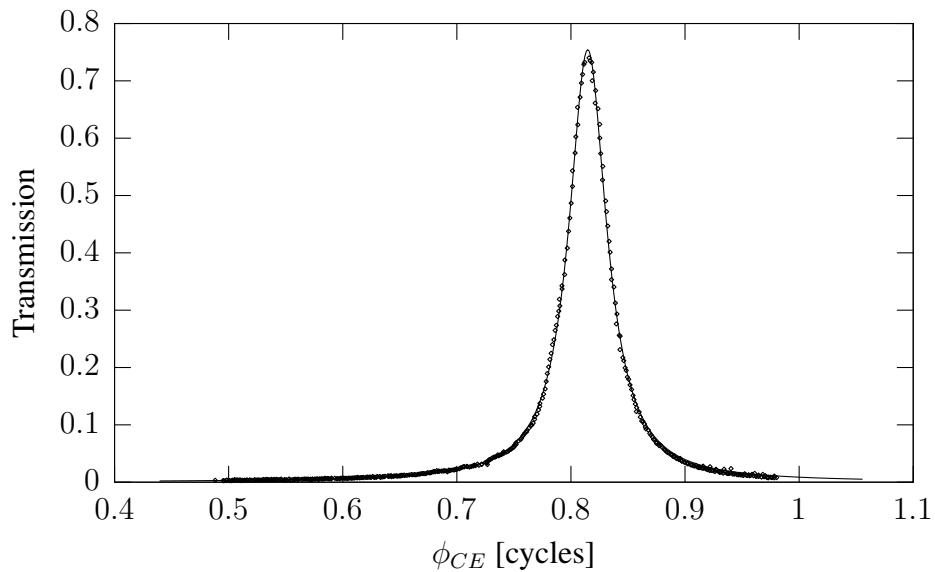


Figure 4.13: Transmission of the resonator at 770 nm. Measured points (diamonds) and fit model (solid line) agree quite well.

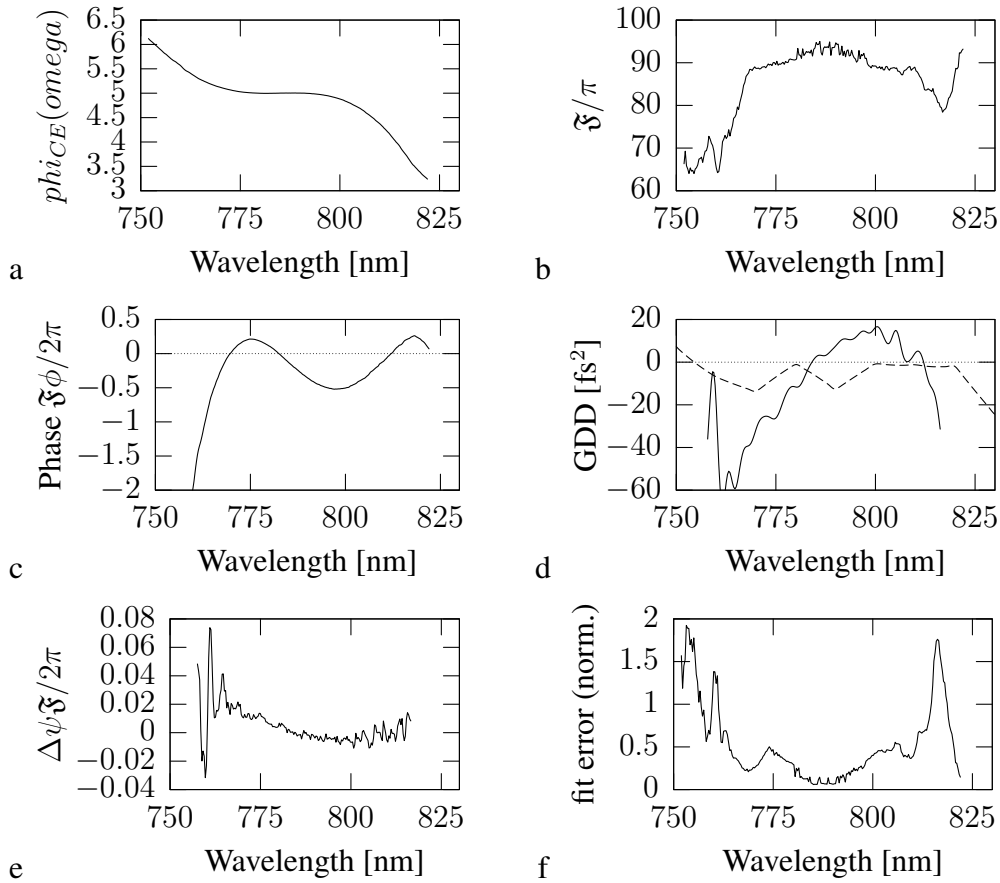


Figure 4.14: Results from fitting the transmission data with model (4.6). (a) The center of the fringe $\phi_{CE}(\omega)$, (b) The resonator finesse (divided by π) as calculated from the fitted round trip gain r using (3.34), (c) The effective round trip phase $\psi(\omega)$ from expression (3.75), where the unknown constants ϕ'_{CE} and $\psi(\omega_{fix})$ were chosen such that the spectrum in figure 4.10 would be the result. (d) Second derivative of $\psi(\omega)$ obtained like this. To get a nice plot the data phase data was low pass filtered with a cutoff frequency of about 1.5 THz, corresponding to a resolution of about 3 nm. (e) The phase rejects of the smoothing low pass filter. As this is small compared to the relevant scale for this resonator, no important information is removed by the filter. (f) square sum of the residuals of the fit normalized to the fitted model integral. The fit become less accurate in the wings of the spectral range covered.

hence the resonator dispersion may be calculated using (3.75) and (3.76). In addition to that, the resonator finesse as a function of wavelength can be determined from the width of the Airy fringes $r(\omega)$, provided the resonator lock that ensures (3.74) is tight enough so that the observed fringe is not broadened by lock fluctuations. In the present case, these fluctuations were on the order of 30% of the resonance width so that the observed finesse is slightly reduced compared to the real value. The impedance matched enhancement factor calculated from the measured r values is around 90 within the spectral range of the driving light. For calculating the GDD function from the measured round trip phase data, a low pass filter was applied to the result in order to make it readable. This is because calculating the GDD involved taking the second derivative of the round trip phase. This differentiation amplifies fast fluctuations in the measured phase with a factor proportional to the square of the fluctuation frequency. Hence these fast components would dominate the GDD function, obscuring the relevant slow changes. To check that the low pass filter has not removed important information about the round trip phase, the filter rejects (i.e. the difference between the filtered and the unfiltered phase data) was analyzed and is shown in figure 4.13e. In this case the low pass filter was chosen to be a Gaussian filter with a bandwidth of about 3 nm. The resulting filter rejects are on the order of a few percent of the resonator linewidth, so that no important information is lost. The resulting GDD function has two zero points at about 785 nm and 810 nm, so that the driving spectrum is neatly centered with respect to these zero crossings. However the magnitude of the GDD in between is with about 10 fs^2 on average, relatively large compared to separation of the zero points and the resonator finesse⁶. Hence the observed strong spectral filtering, which leaves room for optimizing the resonator dispersion.

4.2 High harmonics in a resonator

Now that it has been shown that the peak power of an ultrafast oscillator can be enhanced by a considerable amount using a suitable resonator, in the following sections some results on high order harmonic generation inside such a resonator will be given, as they were published in Nature (Gohle et al. 2005). A very similar result was published almost simultaneously by Jones and Ye (2005b). The achieved peak intensity inside the resonator of about $2.5 \times 10^{13} \text{ W/cm}^2$ is sufficient to get considerable nonlinear response, at least from the noble gas with the lowest ionization potential: xenon⁷. To avoid reabsorption of the generated XUV radiation, the xenon target was injected into the interaction region (one Rayleigh length⁸ around the focus position) with a small glass capillary with about $50 \mu\text{m}$ placed right above the focus in the vacuum chamber.

As the main interest in this investigation lies in coherently upconverted radiation, due to the tight phase link between fundamental, this high order harmonic radiation will be emitted collinearly with the fundamental beam. To analyze the radiation and make it accessible for other

⁶i.e. the spectral separation of the zeros and $\Delta\omega_{FWHM}$ from (3.59) are comparable.

⁷Of course there is also radon, which has an even lower ionization potential but as it is radioactive, it was not chosen for this experiment.

⁸The Rayleigh length b of the focus of a Gaussian beam of radiation with wavelength λ and focus radius w_0 is given by $b = 2\pi w_0^2/\lambda$.

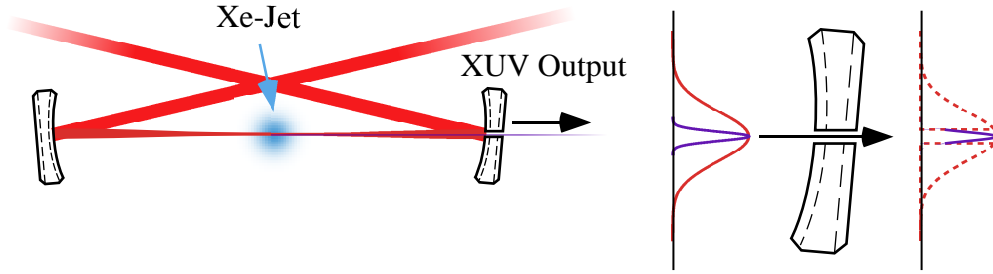


Figure 4.15: Schematic for hole coupling in a resonator. A small aperture at the center of one cavity mirror transmits the narrow XUV beam while most of the wider fundamental is reflected.

experiments, a way has to be found to get the radiation out of the resonator. The XUV wavelength range is especially problematic in that context, as there is essentially no solid state material that is not strongly absorbing. Therefore, the technique conventionally used with nonlinear conversion resonators, using a mirror that is highly reflecting for the fundamental and highly transmissive for the converted light, is not an option. The mirror substrate and the dielectric coating would absorb the generated light. The following section discusses some solutions to that problem, including the one employed during this work. After that the observed harmonic spectrum and the experiments performed to show the coherence of the generated light will be described. Finally some discussion of these results will be given.

4.2.1 Coupling

The probably tightest restriction in the search for possible coupling mechanisms of the generated light is, that it has to have the lowest possible loss for the light circulating inside the resonator, in order not to spoil the finesse of the resonator and keep the circulating power high. One method to separate fundamental and high order harmonics from each other, that is well known in the HHG community, uses the fact that the high harmonics exhibit a much smaller divergence angle than the fundamental beam. Then by aperturing the emerging beam (in the far field) using a hole of appropriate size, most of the generated XUV is transmitted, while almost the entire fundamental is blocked and only the central part will be transmitted (see figure 4.15). If the fundamental beam is annular in shape, even the entire fundamental can be blocked.

For a Gaussian beam with a $1/e$ field radius in the focus of w_0 , the divergence angle θ (i.e. the angle between the $1/e$ radius as a function of distance and the propagation axis) of the beam in the far field (i.e. many Rayleigh lengths away from the focus) is given by

$$\theta = \frac{\lambda}{\pi w_0}. \quad (4.7)$$

Neglecting phase-matching for the moment, the focus size of the generated harmonics in the plateau can be estimated by the following argument. If a power law is assumed for generated intensity I_h as a function of fundamental I_f : $I_h \propto I_f^{a_h}$, then the profile of the focus of the harmonic beam will be a Gaussian function, with a radius that is $\sqrt{a_h}$ times smaller than the

fundamental radius. Therefore the ratio between the divergence of the harmonic of order n (having an n times shorter wavelength than the fundamental) and the fundamental divergence is

$$\frac{\theta_h}{\theta_f} = \frac{\lambda\sqrt{a_h}\pi w_0}{n\pi w_0\lambda} = \frac{\sqrt{a_h}}{n}. \quad (4.8)$$

In the perturbative regime, where a_h is equal to the harmonic order, the beam divergence of the generated harmonic decreases as $1/\sqrt{n}$. For high order harmonics, the power law has to be independent of the harmonic order (otherwise there would be no plateau) and therefore the beam divergence decreases as $1/n$. Therefore the ratio between the beam diameter of the fundamental and the plateau harmonics in the far field increases as n , and an aperture with two beam radii for the harmonic will transmit 98% of the harmonic, while transmitting $1 - \exp(-(2\sqrt{a_h}/n)^2)$ of the fundamental. This is 1% for $n/\sqrt{a_h} \approx 20$ and 10^{-3} for $n/\sqrt{a_h} \approx 60$. If the aperture is a mirror with a hole in the center, where the harmonics are transmitted, while the fundamental is reflected around the hole, this means, that to keep the losses below a percent for the fundamental and still transmit most of the generated harmonic, relatively high order harmonics ($n > 40$ or so) have to be used.

The numbers above assume fundamental Gaussian modes. While these modes are the resonator eigenmodes that provide the highest peak intensity inside a focus (and therefore the most efficient harmonic generation), in the context of coupling harmonics through a hole, they are bad as they have their intensity maximum on the axis, where the hole in the mirror is located. To get around that it was proposed by Jones and Ye (2005a) to use a higher order Gaussian mode instead. For example the TEM₀₁ mode has a intensity minimum in the center of the beam. This could make the coupling through a hole available for lower order harmonics as well.

An alternative to transmissively coupling the XUV radiation out of the cavity, is to reflect it out at an interface where the fundamental is transmitted. Such a place could be a Brewster window that has very low reflection loss for the fundamental. Here it comes handy, that the absorption of the XUV radiation is high in most materials. If the absorption resonance lies on the red side of the incident radiation, the refractive index for that radiation can be much smaller than one and the Fresnel reflection from such an interface can be rather high. As an example in figure 4.16, the Fresnel reflectance of sapphire (Al_2O_3) is shown in the XUV wavelength range for p-polarized light incident on a Brewster surface for radiation at 800 nm (incidence angle 60.4°) and using refractive index data taken from Palik (1991). Many materials show a similar behavior with relative high reflectance just below 100nm. In table 4.1, a summary of reflectance values at 60 nm is given for several materials for p-polarized light at an incidence angle corresponding to Brewsters angle for 800 nm radiation. The most interesting materials in the table given are diamond and silicon carbide (SiC). Diamond however has the problem that it is quite expensive and hard to get in optical quality especially as mono crystalline diamond of appropriate size and purity is only available from natural sources and frequently exhibits stress induced birefringence. Quick experiments performed with chemical vapor deposition (CVD) produced diamond showed that the XUV reflectance at normal incidence, where it should be above 40% at 60 nm according to the tabulated refractive index data showed a reflectance of strength equal to gold (10%). This is probably due to the fact that the samples used by Palik (1991) had quite some nitrogen impurities. Moreover CVD diamond is not well qualified as an

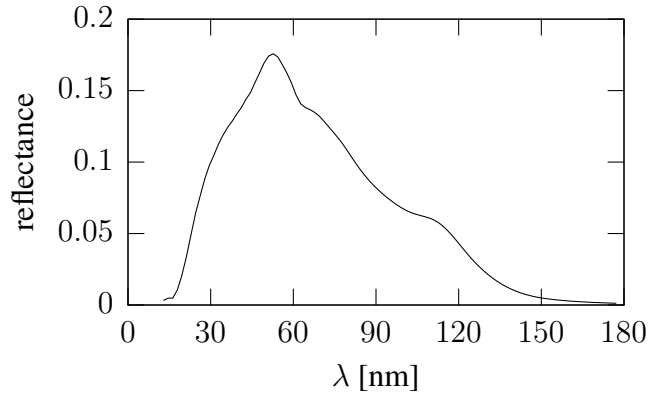


Figure 4.16: Fresnel reflectance of sapphire for p-polarized radiation at an incidence angle of 60.4° (Brewster's angle for 800nm), determined using tabulated refractive index data from Palik (1991).

Material	$n(800 \text{ nm})$	$a [\text{mm}^{-1}]$	$n(60 \text{ nm})$	$R(60 \text{ nm})$
SiO ₂ (crys.)	$1.54 - < 10^{-4}i$	< 0.8	$0.79 - 0.65i$	12%
fused silica	$1.46 - < 10^{-6}i$	$< 10^{-2}$	$0.86 - 0.5i$	7%
ZnS	$2.31 - 3 \times 10^{-6}i$	2×10^{-2}	$0.78 - 0.28i$	24%
MgO	$1.73 - < 10^{-7}i$	$< 10^{-3}$	$0.68 - 0.71i$	21%
C (diamond)	$2.39 - < 10^{-6}i$	$< 10^{-2}$	$0.50 - 1.3i$	48%
SiC	$2.60 - < 10^{-4}i$	< 1	$0.347 - 0.53i$	63%
Al ₂ O ₃	1.76		$0.805 - 0.725i$	15%

Table 4.1: Complex refractive index at 800 nm and 60 nm wavelength for various materials. a is the absorption length at 800 nm and R the Fresnel reflectance at 60 nm for p-polarized radiation at an incidence angle of $\arctan(\text{Re}(n(800 \text{ nm})))$ (Brewster's angle at 800 nm). Refractive index data taken from Palik (1991)

Figure 4.17: Scheme for output coupling the generated XUV radiation. The fundamental laser mode is transmitted through the brewster plate with small losses while the XUV is reflected due to the material having a refractive index smaller than one, resulting in total external reflection.

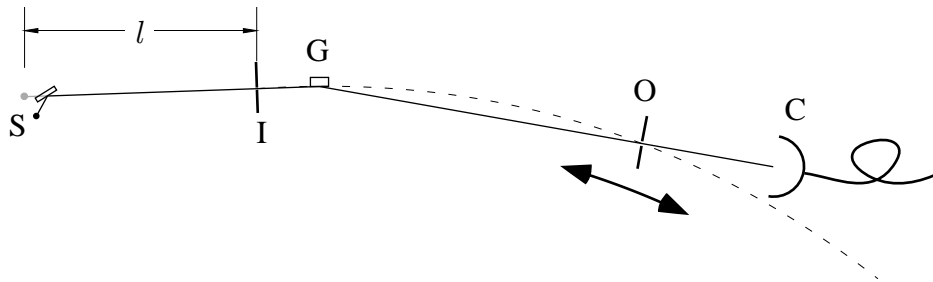
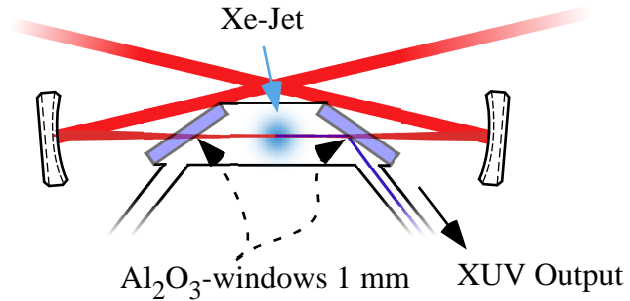


Figure 4.18: Monochromator geometry. S: XUV source, I: input slit (2° incidence angle), G: Grating (1 m focal length), O: output slit moveable on a rowland, C: channeltron detector. The distance from source to entrance slit is marked as l . circle (dashed line)

optical material in the visible and near infrared because of its large grain size⁹. Silicon carbide on the other hand should be a really good candidate, as it should be available with low absorption and scatter. This material is also interesting for beam steering applications and normal incidence (focusing) mirrors as the normal incidence reflectivity should be larger than 34%. However, no SiC sample was available during our experiments and we had to resort to sapphire as an output coupler.

Figure 4.17 shows the arrangement used in the setup. The Brewster windows that seal the interaction vacuum chamber are made from sapphire and simultaneously used as the XUV beam splitter. The XUV output port may be connected to an experimental vacuum chamber.

4.2.2 Harmonic spectrum and coherence

The generated XUV output was analyzed using a grazing incidence monochromator (McPherson Model 248/310G) whose geometry is shown in figure 4.18, that was attached to the output port. The monochromator was equipped with a channeltron detector (BURLE CEM4751G). This detector has the nice property that it is sensitive below 160 nm only. Therefore no special measures had to be taken to remove the strong (10 mW average) fundamental from the extracted beam to avoid detector saturation.

The monochromator was first set to zero order, where the entire spectrum was transmitted. After putting the resonator into lock, so that the circulating field had the characteristics described

⁹Very recently, mono crystalline CVD diamond became available in relevant sizes, so maybe this is worth a test.

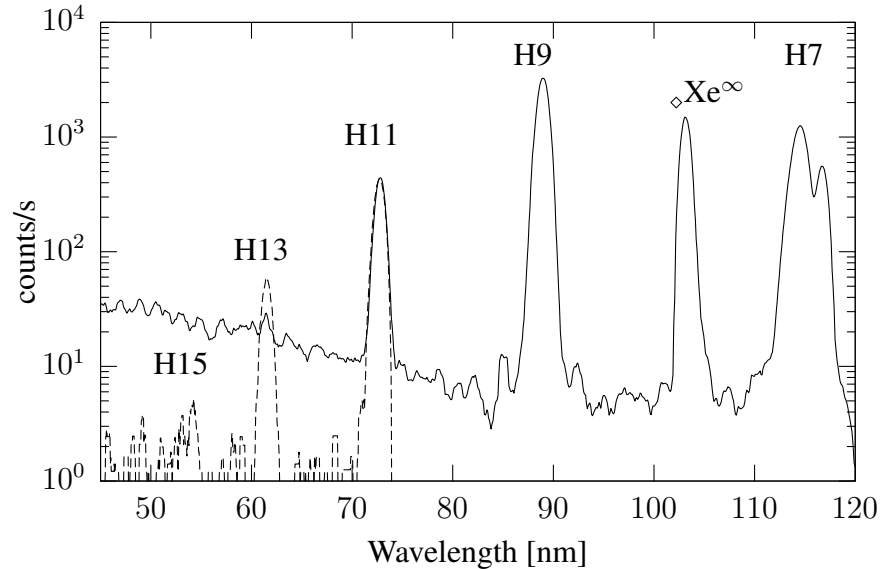


Figure 4.19: Typical harmonic spectrum observed. In solid is the signal observed, when looking directly into the output beam, while the dashed curve is taken with a 1000 Å thick aluminum foil with an absorption edge just below 90 nm in the beam path. This filters away the strongest components in order to reduce the stray light that would otherwise bury the weaker peaks. The dashed signal has been rescaled to have the same magnitude at the 11th harmonic. The harmonics are labeled Hx, and the ionization limit is marked by a point labelled Xe[∞].

in 4.1.7, and xenon was fed to the nozzle with one bar of pressure before the nozzle¹⁰, a clear photocurrent was seen on the channeltron. This photocurrent was maximized by readjusting the nozzle position with respect to the focus, resonator alignment, the driving pulse chirp and the laser offset frequency.

Then the monochromator was scanned and the channeltron signal was recorded using a gated pulse counting device (Stanford Research SR400 photon counter) with a threshold set such that the electrical noise on the signal was mostly rejected. It has to be mentioned, that the channeltron that was used, is not a saturated gain device suitable to generating a signal for photon counting but is merely a proportional mode device. For this reason, the count rates observed are only proportional to the photon count rate, with an unknown proportionality constant depending on the counter threshold and channeltron gain. A typical spectrum recorded like this, is shown in figure 4.19. Harmonics up to 15th order are clearly observed. The cutoff energy¹¹ is at 17 eV, which explains the exponential drop of the harmonic power starting at H11. In addition to the laser harmonics a spectral feature at 103 nm is observed, which lies just below the ionization energy of xenon and corresponds to no integer harmonic of the fundamental laser frequency. This feature has not been observed in previous experiments on high harmonic generation. Its

¹⁰The pressure in the focus is hard to determine in this geometry, as the nozzle is not very well characterized in shape.

¹¹The ponderomotive energy at 2.5×10^{13} W/cm² is 1.5 eV. The ionization potential of xenon is 12.13 eV.

Feature	P_{out} [pW]	P_{gen} [nW]	Efficiency
H7	480	9.6	1×10^{-8}
Xe $^{\infty}$	290	4.5	6×10^{-9}
H9	820	9.8	1×10^{-8}
H11	90	0.8	1×10^{-9}
H13	10	0.07	1×10^{-10}

Table 4.2: Estimated power in different spectral components. P_{out} is the power reflected out by the sapphire, P_{gen} is the estimate of the generated power using the calculated reflectance of the sapphire window. The last column shows the conversion efficiency from driving laser average power to generated XUV power.

possible origin will be discussed in section 4.2.3.

To get an estimate of the power in each of the harmonics, the monochromator was removed from the beam path (as its transmission was unknown) and the channeltron was placed directly into the XUV beam. The total photo current at a channeltron bias of 1.36 kV was measured using a 1 M Ω load resistor and a voltmeter. A total photo current of about 1 μ A was measured like this, which according to the manufacturer's specification converts into 0.85×10^9 photons per second. From the measured spectrum (assuming constant transmission), it is known that the major contribution to the signal comes from the three spikes at between 80 and 120 nm and each of these peaks is approximately of the same height. Therefore the total power can be estimated using an average photon wavelength of 100 nm or 12 eV energy. Then the total power leaving the setup is about 1.6 nW. If again a constant quantum efficiency of the detector and constant spectral transmission of the monochromator is assumed, the measured spectrum can be used to assign powers to each spectral feature by normalizing the spectrum to 1.6 nW. The result is shown in table 4.2. The total conversion efficiency, i.e. the ratio between generated and incident fundamental power is estimated to be on the order of 10^{-8} .

The dependence of different spectral features generated powers as a function of peak intensity is shown in figure 4.20. Both the H9 and H11 line show high exponents (close to the values from perturbation theory) for intensities below 1.5×10^{13} W/cm 2 and a slight decrease for intensities above that intensity to an exponent of about 7. This indicates that the intensities are approaching the strong field limit, where simple lowest order perturbation theory does not produce valid results anymore. No saturation is seen for the odd harmonics up to the investigated intensity. The line just below the xenon ionization limit on the other hand exhibits an extremely high exponent of 11.5 for lower power, while a quick saturation is observed around 1.8×10^{13} W/cm 2 after which the yield even decreases.

Spatial coherence has been investigated with a very simple method. The entire monochromator assembly was shifted transverse to the beam axis. This allowed the entrance slit (300 μ m width) to sample different positions in the beam, 260 mm away from the source and the transmitted power was recorded as a function of the transverse translation. The Xe $^{\infty}$ feature was found to have an almost constant intensity if the monochromator was *rotated* about the source point, indicating a relatively large beam divergence. When shifting the monochromator, the limited viewing angle of the device introduced a varying aperture that could be quantified by recording

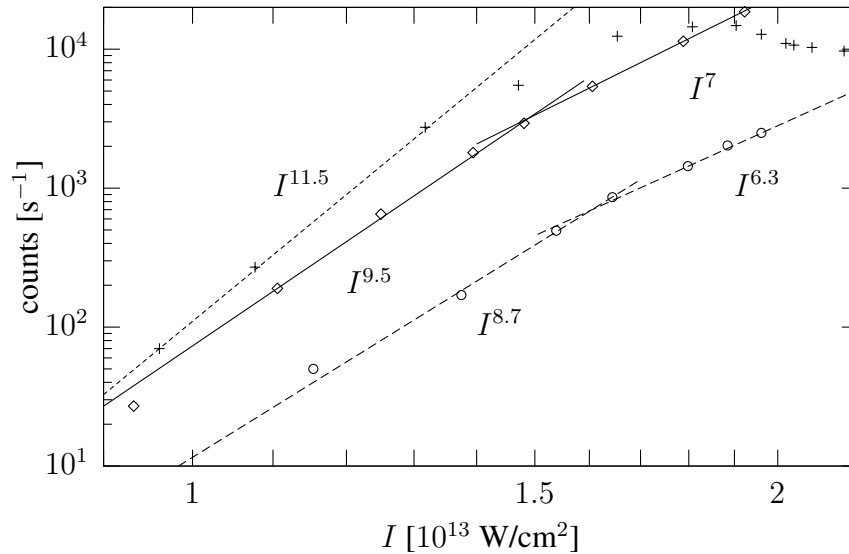


Figure 4.20: Power scalings of different features in the spectrum. Diamonds indicate values for H9, circles correspond to H11 and crosses to Xe^∞ . Lines are power law fits to H9 (solid) data with exponents 9.5 and 7, H11 (dashed) with exponents 8.7 and 6.3, and to Xe^∞ (dash dot) with exponent 11.5. Saturation of the Xe^∞ feature is observed for high intensities.

the Xe^∞ intensity. By normalizing beam profiles of the other features with the Xe^∞ data, this effect was eliminated. The results are shown in figure 4.21. The diameters obtained by fitting a Gaussian profile to the taken data shows a ratio between fundamental and harmonic divergence angle θ_f/θ_h of 4.5, 6 and 6.4 for H7, H9 and H11, respectively. Table 4.3 compares the measured values to expected ones.

The most important property of the generated radiation is the temporal coherence, i.e. that the frequency comb of the fundamental is actually transferred into the generated harmonic radiation. The typical way to proceed in this context, is to generate a beat signal between a single frequency or frequency comb source and the light under investigation. As during this work there was no second XUV frequency comb available, as a first test a beat experiment was performed that involved H3 from the described setup. The wavelength of H3 is at 265 nm, which is still accessible by conventional lasers and solid state harmonic generation. Figure 4.22 shows the optical setup. The third harmonic from the enhancement resonator (at 265 nm) is overlapped with the fourth harmonic of a mode-locked Nd:YVO₄ laser running at 1064 nm with repetition rate $f_r = 76$ MHz. The two lasers are synchronized using a phase locked loop feeding back on the Nd:YVO₄ laser repetition rate and using the second harmonic of repetition rate of the HHG system and the third harmonic of the repetition rate of the Nd:YVO₄ laser as inputs. Like this, if the phase between the two is adjusted appropriately, every second pulse from the Nd:YVO₄ laser coincides with every third pulse from the HHG output, so that the beat signals between different comb modes can add up in phase and result in a measurable electronic signal on the photo multiplier tube.

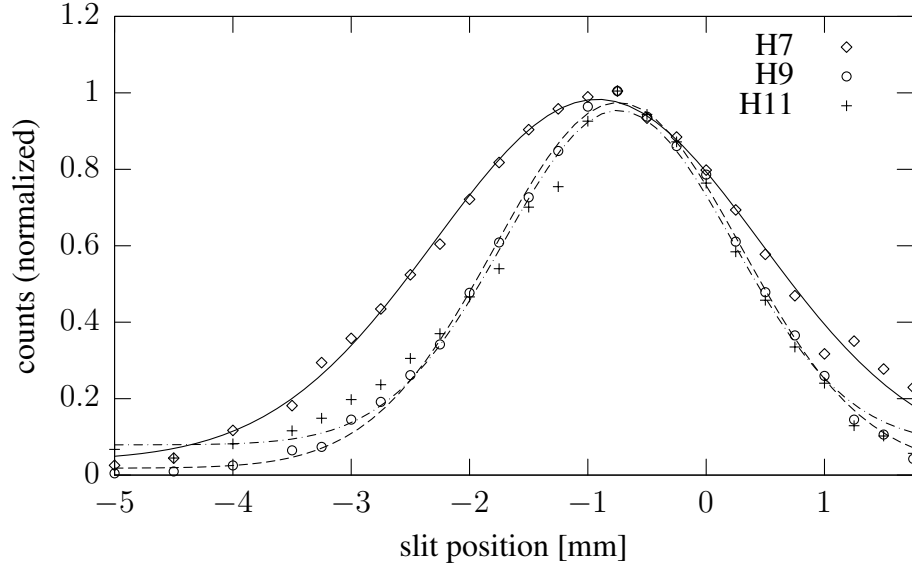


Figure 4.21: Beam profiles for different spectral features. Symbols show the measured profiles (normalized by the data taken at the Xe^∞ feature to eliminate the effect of changing apertures due to the limited viewing angle of the device). The fits give the following diameters H7: 2.75 mm, H9: 2.08 mm and H11: 1.94 mm, 260 mm away from the generating focus.

Feature	θ_f/θ_h	$n/\sqrt{a_{meas}}$	$n/7 * 4.5$
H7	4.5		4.5
H9	6	3.4	5.8
H11	6.4	4.4	7.1

Table 4.3: Comparison of the measured beam divergences θ_f/θ_h with the result (4.8) using the measured exponents a_{meas} for high intensities and with an expected scaling for the plateau region (assuming constant a), where the ratio should be proportional to the harmonic order n . The observed divergences are smaller than (i.e. bigger ratio) than expected from the measured exponents. This may be due to phase-matching and/or saturation on the beam axis, leading to a larger focus. The scaling of the ratios with harmonic order is rather compatible with plateau harmonics.

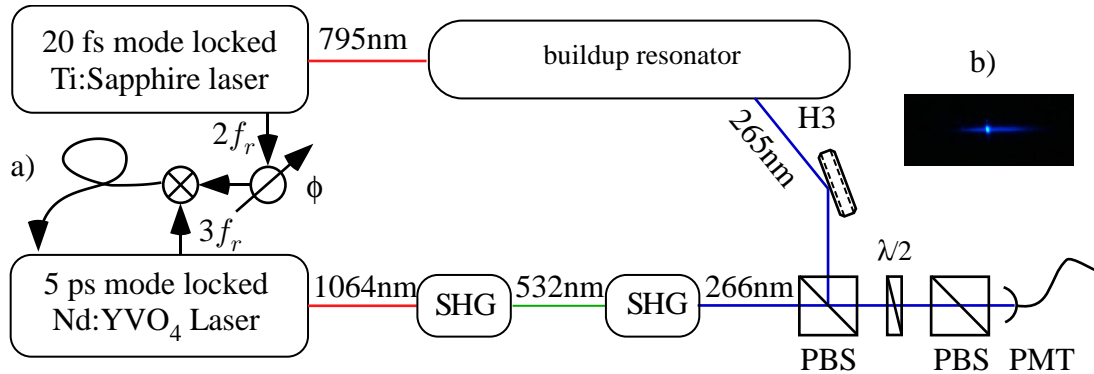


Figure 4.22: The setup for the beat experiment. a) Optical schematic, the H3 component of the HHG setup is overlapped with the fourth harmonic of a mode-locked Nd:YVO₄ laser with repetition rate $f_r = 76$ MHz. The two lasers are synchronized with a phase locked loop with adjustable phase delay. b) Grating image of the overlapped beams. The broad faint line is the H3 spectrum while the small bright spot is the fourth harmonic of the Nd:YVO₄ laser. SHG: second harmonic generation, PBS: polarizing beam splitter, $\lambda/2$: half wave plate for polarization rotation, PMT: photomultiplier tube. ϕ phase shifter.

With $1.6 \mu\text{W}$ of H3 and $0.5 \mu\text{W}$ of fourth harmonic of the Nd:YVO₄ going onto the detector, a beat signal as shown in figure 4.23 could be observed. This signal was recorded for $100 \mu\text{s}$ using a digital oscilloscope in conjunction with a FFT algorithm. The resolution of the Fourier transform is 100 kHz and the beat signal is Fourier limited as illustrated in 4.24. The signal to noise ratio (SNR) of the beat is determined from this data to be 16 dB in 100 kHz bandwidth. The spectral bandwidth of the Nd:YVO₄ laser is about 200 times smaller than the H3 output. Therefore, only 1/200th of the H3 power contributes to the beat signal. The shot noise limited beat signal should be 35 dB in 100 kHz bandwidth from these considerations. The missing 20 dB in the observed signal is most probably due to poor mode matching and excess noise from the photo multiplier.

4.2.3 Discussion

In this chapter it was shown that high order harmonics can be generated from a mode-locked laser directly with an extremely high repetition rate exceeding 100 MHz, if a suitably designed enhancement resonator is used. The generated radiation contained photons up to the 15th harmonic of the fundamental. The cutoff energy for high order harmonic generation lies at 17 eV, at the estimated peak intensities in the focus. This is consistent with the exponential roll off of the harmonic power starting at H11. It was shown that the beam profile exhibited a nice Gaussian shape with very small divergence angles, indicating a well-behaved wavefront, suitable for tightly focussing the generated light into a small area, although the test results are quite preliminary in that respect.

Power scaling of the generated light was investigated, yielding high exponents for both harmonics that were under consideration. This shows that the process is not very close to saturation

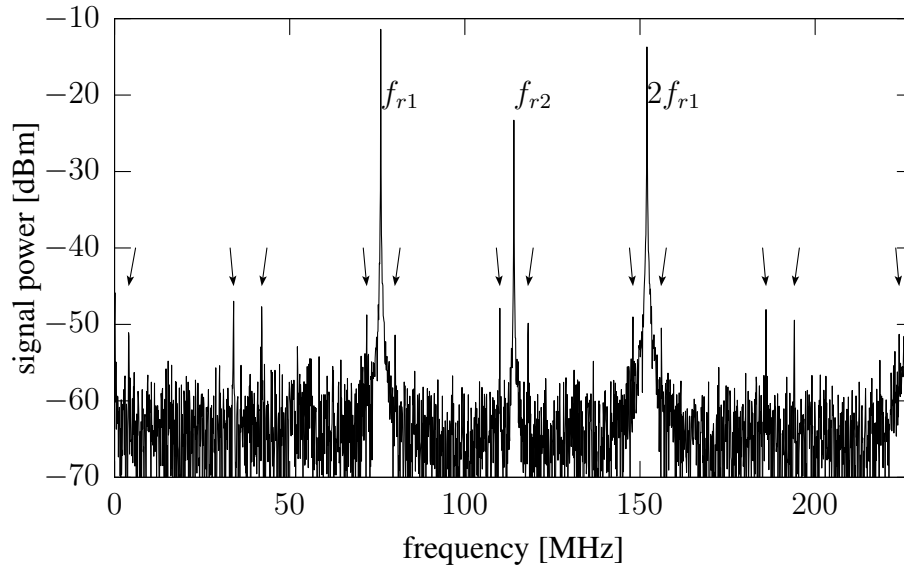
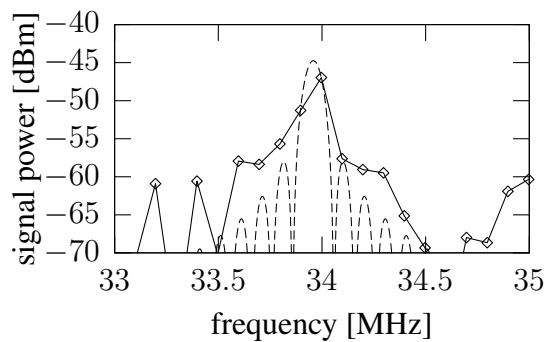


Figure 4.23: RF spectrum of the signal from the photomultiplier tube. f_{r1} marks the repetition rate of the Nd:YVO₄ laser (76 MHz), f_{r2} the repetition rate of the HHG system (114 MHz) and arrows mark the beat signals between the two frequency combs with respective repetition rates.

Figure 4.24: The beat signal at 34 MHz (solid) and the point spread function of the Fourier transform (dashed, with center frequency and amplitude fit to the data). This shows that the beat is Fourier limited.



up to the peak intensities that were available in the setup, so that scaling up the peak intensity by using a stronger pump laser and/or going to a higher finesse resonator can be expected to tremendously increase the output power of the system. Saturation due to ionization is expected to occur in xenon at the pulse duration used once the intensity approaches 10^{14} W/cm². Therefore if an exponent of 6 is assumed for the plateau harmonics, then increasing the peak intensity by a factor of 4 should increase the XUV output by more than three orders of magnitude. This should already yield several μ W output power for H9. The higher peak intensity would also push the cutoff energy to 30 eV. As H13, which is the main target for future experiments in our laboratory, was very close to the cutoff in the described experiments an even stronger scaling can be expected for that harmonic.

It was shown that the H3 component of the generated radiation exhibited a frequency comb structure that showed Fourier limited linewidth at 100 kHz resolution. In the paper by Jones et al. (2005) it was demonstrated that the beat signal between the third harmonic generate in a gas jet (similar to our experiment) and the third harmonic generated with a standard solid state conversion shows Hertz level linewidth, which demonstrates again that the excess phase noise from the gas jet is small. As the interesting wavelength range is below (or at) 120 nm of course it still remains to be shown that the components H7 and above actually exhibit a frequency comb that can be utilized for high resolution spectroscopy. Yet this first test suggests that this is indeed the case, especially if a highly stable high finesse resonator is employed that has the ability to remove noise from the driving laser as elaborated in section 3.2.6. Indeed some of the excess noise contributions discussed in section 3.1.3 can be estimated. The phase modulation amplitude due to plasma density fluctuations at the fundamental laser frequency has to be smaller than a resonator linewidth for modulation frequencies that lie outside the bandwidth of the feedback loop (a few tens of kHz) as otherwise the circulating power would have to be strongly modulated, which is not observed. The resonator linewidth is about 10 mrad (finesse of 100π) and the plasma phase shift fluctuations have to be smaller than that for frequencies higher than the servo bandwidth. As the plasma phase shift is quadratically dependent on the optical frequency, the rms phase shift on the 11th harmonic is 121 times smaller and therefore in the 0.1 mrad range. Intensity fluctuations of the fundamental field are smaller than 5% in the demonstrated experiment. As the nonlinear phase shift for the long trajectory (worst case) is given by (A.26) for plateau harmonics and in our case $U_p \approx \hbar\omega_0$, the total nonlinear phase shift is on the order of unity. Therefore the nonlinear phase fluctuations should be less than 100 mrad. The phase noise of the fundamental comb was not analyzed, therefore the upconverted phase noise can not be evaluated here. However, the driving laser may be stabilized to a high finesse reference cavity so that Hertz level linewidth may be achieved, effectively eliminating the problem for the lower harmonics, say up to twentieth order or so.

To clarify if the additional Xe[∞] feature at 103 nm is a plasma fluorescence or not, the channeltron detector was placed at the other vacuum port of the generation chamber, which uses the entrance window as a XUV mirror and looks into the HHG source in the propagation direction of the fundamental beam. If the emission at 103 nm were fluorescence with no phase relation to the driving beam, the emission pattern should be symmetric around the polarization direction of the driving radiation and light should be observable in the reverse direction. As nothing was observed at this port, the conclusion is that the observed line has to have a certain amount of phase

coherence with respect to the driving field, so that the emission is directed in the propagation direction of the fundamental beam. The information from this quick experiment is too limited to construct a complete physical picture of the origin of the observed feature. It is however remarkable, that no previous experiment on HHG observed such a thing. It is therefore interesting to discuss the possible cause of it.

At first, it is remarkable that the emission frequency is very close to the ionization limit of xenon. This indicates that Rydberg states of high principal quantum number n are involved in the process. A first question is therefore, why should Rydberg states become populated? Two possibilities are direct multiphoton excitation of the states and recombination of free electrons with ions in the plasma. Recombination from the plasma requires a third particle, that carries away the momentum of the electron and typically leads to states with high angular momentum, so that a radiative decay of the Rydberg state is not possible due to selection rules. The third particle would also carry away some fraction of the phase information of the driving field, so that it can not be assumed that the emission is directed, even if the recombined electrons were able to decay to the ground state directly. Direct photonic excitation seems to be ruled out by the fact, that the driving radiation is far detuned from any subharmonic of the transition frequencies in question. But, as the intensity in the driving field is very high, the atomic level structure will be strongly perturbed by the driving field. For the high n states, which are almost like free electrons, the AC Stark shift is essentially the same as for free electrons, whose energy is increased by U_p with respect to the field free case. With a peak ponderomotive potential of 1.3 eV, the Rydberg states are shifted into eightphoton resonance with the driving field and some population can accumulate during the passage of the pulse. It is also very unlikely that these states are directly field ionized by one pulse (if n is high enough), as the ionization time is on the order of one Kepler period (orbit time).

Now that there is (coherent) population, it can radiate in phase with the driving field until coherence is lost. If that time is much longer than the duration of the pulse, most of the time during emission there will be no perturbing field and the emission will be at the frequency of the unperturbed transition frequency, leading to the observed line. This process is depicted in figure 4.25.

This explanation is very qualitative and needs to be investigated more closely. In particular, it does not explain where the missing energy between the absorbed photons and the emitted photon goes. It was proposed that it might induce a blue shift of the driving field. Another thing that remains unexplained is the fact that this spectral feature was not observed in other experiments. The biggest difference between the presented experiment and other HHG results is that the duration between adjacent pulses hitting the target is reduced by more than three orders of magnitude. For that reason the gas target is not entirely replaced from one pulse to the next and the atoms see about three pulses before leaving the focus (assuming thermal velocities at 300 K). Additionally the peak intensity is relatively low compared to other experiments with similar short pulses. This could lead to a lower plasma density. At high plasma density on the other hand the Rydberg states could be destabilized by the stray electric fields of the ions and electrons, which could make the effect disappear. The reduction in generated power in the Xe^∞ feature at high intensities that is observed in the presented results also points in this direction.

Another feature in the observed XUV spectrum 4.19 requiring explanation, is the double

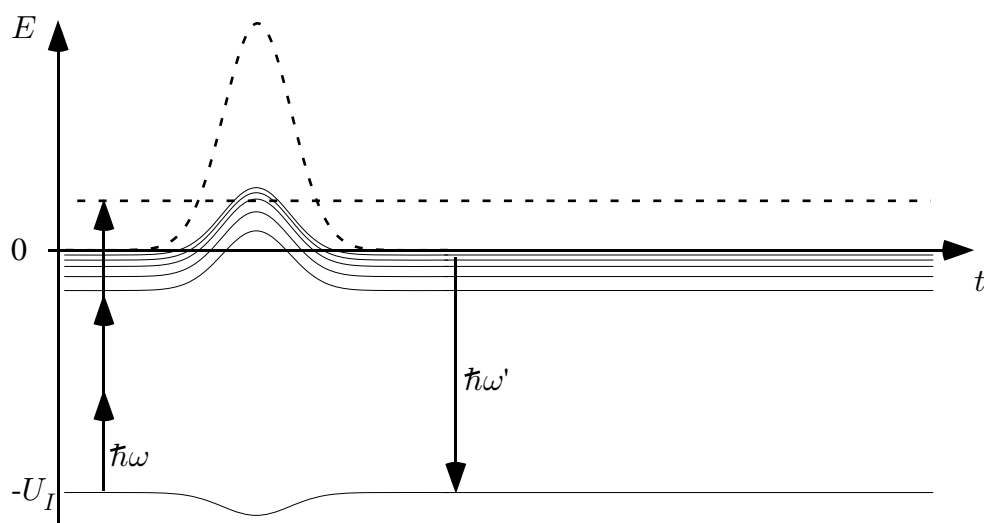


Figure 4.25: Process leading to the Xe^∞ feature at 103 nm. The high-lying Rydberg states are resonantly excited during the pulse (dashed peak) by a multi photon (3 photons in this sketch, in xenon this would be 8 in our case) process that is shifted into resonance by the AC-Stark effect. The excited dipole radiates for a long time so that most of the emission is at the unperturbed frequency.

peak structure of the H7. This can be attributed to nearby resonances in xenon, that modify the nonlinear response.

Chapter 5

Outlook

With coherent quasi continuous extreme ultraviolet sources being a reality now, new exciting applications immediately come to mind. The relatively simple spatially coherent source could enable high spatial resolution microscopy or holography applications.

The XUV pulse train of unprecedented high repetition rate might enable new investigations in attosecond physics. For example in experiments where space charge is a critical parameter, it would become possible to work in an intensity regime, where the charge created per XUV pulse is much smaller than one electron, while maintaining an event rate in the MHz range. This results in an increase of the quantum limited signal to noise ratio by at least two orders¹ of magnitude compared to conventional kHz amplifier sources.

The major application however can be foreseen to lie in the field of high accuracy spectroscopy. The anticipated temporal coherence of the XUV pulse train will make the accuracy of state of the art time standards available in a spectral region or energy range that was previously inaccessible to high precision physics. In a specific ambitious project, we plan to apply frequency combs in the XUV directly to precision spectroscopy of sharp resonances in laser-cooled trapped ions. The hydrogen-like helium ion with a 1S-2S two-photon transition near 60 nm is a particularly interesting candidate, since this simple atom permits unique confrontations between quantum electrodynamic theory and experiment.

This type of frequency comb spectroscopy can be understood as a multi pulse Ramsey-type quantum interference spectroscopy and has been demonstrated for a few pulses by Witte et al. (2005) in the deep UV on a two photon transition in krypton and more recently in xenon at 125 nm photon wavelength (Zinkstok et al. 2006). While demonstrating that there is still sufficient phase coherence between the pulses in the pulse sequence, the transient methods employed to generate the finite length pulse trains² introduce time dependent nonlinear phase shifts which in turn break the frequency comb structure. The ability to characterize these phase shifts will most probably limit the achievable accuracy for this type of experiments. In contrast, the XUV source demonstrated here operates continuously, so that the nonlinear phase shifts exhibit the

¹as the repetition rate is about five orders of magnitude higher

²In the mentioned experiments, an amplifier was charged with a finite amount of energy that was distributed amongst a few pulses from a near infrared frequency comb laser which were subsequently converted nonlinearly into the VUV.

same periodicity as the original frequency comb. As a result the frequency comb structure can be expected to be mapped faithfully into the up converted pulse train.

For many of the mentioned applications the output power of the demonstrated coherent XUV frequency comb source was still too low for a real spectroscopy application. Yet the dependence of the generated power as a function of driving power that was observed indicates that a moderate increase of the circulating power inside the enhancement resonator can lead to orders of magnitude higher output power in the XUV. Such an increase of the circulating power can be achieved by increasing the resonator finesse while keeping the circulating pulse duration constant as well as by increasing the power of the driving laser.

During the time of writing a new high power Ti:Sapphire laser system is being developed that is based on the chirped pulse oscillator scheme demonstrated Fernandez et al. (2004) but with a higher repetition rate and stronger pump source. The system will be running at 80 MHz repetition rate and will most probably provide more than 4 Watt average output power with pulse durations on the order of 30 fs. This means that at least a 4 fold increase of the peak power compared to the current laser system can be expected. If saturation effects are not important and a power scaling of the 11th harmonic as given in figure 4.20 in section 4.2.2 is assumed, an output power approaching the μW range can be expected with the current enhancement resonator already.

The resonator finesse can be increased by placing the entire enhancement resonator into a vacuum chamber. Like this, the brewster windows maintaining the vacuum in the current setup can be removed and one of them can be replaced by a thinner plate that only serves as an output coupler for the generated radiation. As a result the losses inside the resonator, stemming from absorption and scatter in air as well as the surfaces and bulk material of the windows is drastically reduced. In addition the amount of dispersion that needs to be compensated becomes much smaller so that it is possible to reduce the number of (inherently more lossy) chirped mirrors inside the resonator. When increasing the resonator finesse, however controlling the resonator dispersion accurately becomes more critical. But with the new method described in section 3.2.4 the precise requirement for a dispersion compensating mirror can be determined and an appropriate coating can be designed³. In this way, enhancement resonators with a finesse exceeding 500 and tailored dispersion for supporting 30 fs pulses can be expected so that one may expect to even reach tens of μJ circulating pulse energy, which is already comparable to the pulse energies used by Witte et al. (2005) but with a continuous source.

With an expected output power in the μW range for XUV photons, in addition to the exciting applications mentioned above one may as well think of a variation of fourier transform spectroscopy: Instead of building a Michelson interferometer for the XUV light itself, which is technically difficult it is possible to build a Michelson interferometer for the fundamental infrared radiation and feed the output of that into the enhancement resonator for XUV generation. Such a system can be interesting for spectroscopy applications where the coherence time of the system under study is shorter than the time between two pulses from the frequency comb, so that

³As a side effect, this method for dispersion characterization of a resonator can also be used as a high sensitivity spectroscopy tool. A sample placed inside will cause absorption and refractive index changes. The sensitivity of our method to absorption is comparable to classical ring down spectroscopy, while our method also yields the real part of the refractive index.

the comb will not be visible to the system.

Appendix A

Quantum mechanical description of the atomic polarization

The Schrödinger equation of an electron in an atomic potential $V(\mathbf{x})$ and exposed to an arbitrary laser field $\mathbf{E}(t)$ is¹

$$i\hbar \frac{\partial |\psi(t)\rangle}{\partial t} = \left(-\frac{\hat{\mathbf{p}}^2}{2m_e} + V(\hat{\mathbf{x}}) + e\hat{\mathbf{x}} \cdot \mathbf{E}(t) \right) |\psi(t)\rangle. \quad (\text{A.1})$$

It was assumed here, that the intensity in the field is sufficiently low, so that the magnetic field component can be neglected. After solving this equation the atomic dipole moment

$$\mathbf{d}(t) = e \langle \psi(t) | \hat{\mathbf{x}} | \psi(t) \rangle \quad (\text{A.2})$$

can be calculated, which serves as a source of a classical electromagnetic wave. The spectrum of the dipole emission is determined by the Fourier transform of the dipole moment

$$\hat{d}(\omega) = \frac{1}{\sqrt{2\pi}} \int d(t) e^{-i\omega t} dt. \quad (\text{A.3})$$

A.1 Solution in the strong field limit

The solution to (A.1) was found by Lewenstein et al. (1994). The presented description follows their arguments closely. The so-called strong field approximation (SFA) used to solve (A.1) involved the basic assumptions

1. No bound states of the system contribute to the evolution except the ground state $|0\rangle$.
2. The depletion of the ground state can be neglected.

¹In this context, hats on symbols denote quantum mechanical operators not fourier transforms. This is true only if the symbol is multiplied into a bra or ket state vector.

3. In the continuum, the electron can be treated as a free particle moving in the external field and $V(\mathbf{x})$ can be neglected.

Due to assumption 1 the electron's wave function may be expanded in terms of the atomic ground state and the continuum states only

$$|\psi(t)\rangle = e^{i\frac{U_I}{\hbar}t} \left(a(t) |0\rangle + \int d^3\mathbf{p}' b(\mathbf{p}', t) |\mathbf{p}'\rangle \right), \quad (\text{A.4})$$

U_I being the ionization potential (i.e. the negative ground state energy) and $|\mathbf{p}'\rangle$ the eigenstates of the free electron Hamiltonian with momentum² \mathbf{p}' . Plugging this into (A.1), multiplying with $\langle \mathbf{p} |$ and using $a(t) = 1$ (assumption 2) and $\langle \mathbf{p} | V(t) | \mathbf{p}' \rangle = 0$ (assumption 3) yields a Schrödinger equation for the continuum amplitudes

$$i\hbar \frac{\partial b(\mathbf{p}, t)}{\partial t} = \left(\frac{p^2}{2m} + U_I \right) b(\mathbf{p}, t) + e \sum_i E_i(t) \left(\langle \mathbf{p} | x_i | 0 \rangle + i\hbar \frac{\partial b(\mathbf{p}, t)}{\partial p_i} \right), \quad (\text{A.5})$$

where E_i, x_i, p_i denote the (cartesian) components of the vectors $\mathbf{E}, \mathbf{x}, \mathbf{p}$ respectively and $i = 1 \dots 3$. With the variable transformation

$$\tilde{\mathbf{p}} = \mathbf{p} - e\mathbf{A}(t), \quad (\text{A.6})$$

where $\mathbf{A}(t)$ is the vector potential of the electric field with an appropriate gauge such that $\dot{\mathbf{A}}(t) = \mathbf{E}(t)$, the time derivative of the transformed continuum amplitude is

$$\begin{aligned} i\hbar \frac{\partial \tilde{b}(\mathbf{p}, t)}{\partial t} &:= i\hbar \frac{\partial b(\mathbf{p} - e\mathbf{A}(t), t)}{\partial t} = -ie\hbar \frac{\partial \mathbf{A}(t)}{\partial t} \cdot \nabla_{\tilde{\mathbf{p}}} b(\tilde{\mathbf{p}}, t) + i\hbar \frac{\partial b(\tilde{\mathbf{p}}, t)}{\partial t} = \\ &= \left(\frac{(\mathbf{p} - e\mathbf{A}(t))^2}{2m} + U_I \right) \tilde{b}(\mathbf{p}, t) + e \sum_i E_i(t) \langle \mathbf{p} - e\mathbf{A}(t) | x_i | 0 \rangle, \end{aligned} \quad (\text{A.7})$$

where in the last step (A.5) was used. This is of the form $f'(x) = g(x) + h(x)f(x)$, which has solutions of the form $f(x) = \int_0^x dx' g(x') \exp(\int_{x'}^x dx'' h(x''))$, so that the solution to (A.7) is given by

$$\tilde{b}(\mathbf{p}, t) = -\frac{i}{\hbar} \int_0^t dt_0 e \sum_i E_i(t_0) \langle \mathbf{p} - e\mathbf{A}(t_0) | x_i | 0 \rangle \exp\left(-\frac{i}{\hbar} S(\mathbf{p}, t_0, t)\right), \quad (\text{A.8})$$

where

$$S(\mathbf{p}, t_0, t) = \int_{t_0}^t dt' \left(\frac{(\mathbf{p} - e\mathbf{A}(t'))^2}{2m} + U_I \right). \quad (\text{A.9})$$

is the classical action (plus a constant) of the electron moving in the laser field with canonical momentum \mathbf{p} . At first glance, the influence of the atomic potential has completely disappeared from (A.8). But the atomic structure still plays some role as the integrand in S is shifted up

²i.e. $\hat{\mathbf{p}} |\mathbf{p}\rangle = \mathbf{p} |\mathbf{p}\rangle$

by the binding energy U_I and the ground state $|0\rangle$ determines the tunnel amplitude $\langle \tilde{\mathbf{p}} | x_i | 0 \rangle_{t_0}$. The induced atomic dipole moment can be evaluated by plugging (A.4) and (A.8) into (A.2). If the continuum-continuum matrix elements are neglected ($\langle \tilde{\mathbf{p}}' | x | \tilde{\mathbf{p}} \rangle = 0$) the resulting dipole moment is

$$d(t) = \int_0^t dt_0 \int d^3\mathbf{p} \frac{i}{\hbar} e \sum_i E_i(t_0) \langle \mathbf{p} - \mathbf{A}(t_0) | x_i | 0 \rangle \langle 0 | \mathbf{x} | \mathbf{p} - \mathbf{A}(t) \rangle e^{-\frac{i}{\hbar} S(\mathbf{p}, t_0, t)}. \quad (\text{A.10})$$

This expression has a very nice physical interpretation. It is the integral of probability amplitudes corresponding to the following process: The first term in the integrand

$$e \sum_i E_i(t_0) \langle \mathbf{p} - \mathbf{A}(t_0) | x_i | 0 \rangle \quad (\text{A.11})$$

is the (dipole) amplitude to make a transition from the ground state to the continuum with a (canonical) momentum \mathbf{p} at time t_0 . Then that momentum state evolves freely only influenced by the laser field and acquires a phase factor $\exp(-iS(\mathbf{p}, t_0, t)/\hbar)$ until it recombines at time t with the parent ion into the ground state with the amplitude $\langle 0 | \mathbf{x} | \mathbf{p} - \mathbf{A}(t) \rangle$. The emitted spectrum of such a dipole is readily obtained from the Fourier transform of (A.10)

$$\hat{d}(\omega) = e \frac{i}{\hbar} \int dt dt_0 d^3\mathbf{p} \sum_i E_i(t_0) \langle \mathbf{p} - \mathbf{A}(t_0) | x_i | 0 \rangle \langle 0 | \mathbf{x} | \mathbf{p} - \mathbf{A}(t) \rangle e^{-\frac{i}{\hbar} S(\mathbf{p}, t_0, t) - i\omega t}. \quad (\text{A.12})$$

To evaluate the integral (A.12) it can be argued, that the dipole matrix elements change much more slowly as a function of \mathbf{p} and t than the classical action S , as long as the time interval $t - t_0$ is short enough (a few optical cycles). Because the classical action provides the phase for an oscillatory term, the major contributions to the integral come from the regions in the integration volume where the exponent in (A.12) has a saddle point

$$\nabla_{\mathbf{p}}(S(\mathbf{p}, t_0, t) + \hbar\omega t) = \mathbf{x}(t) - \mathbf{x}(t_0) = 0 \quad (\text{A.13})$$

$$-\frac{\partial(S(\mathbf{p}, t_0, t) + \hbar\omega t)}{\partial t_0} = \frac{(\mathbf{p} - e\mathbf{A}(t_0))^2}{2m} + U_I = 0 \quad (\text{A.14})$$

$$\frac{\partial(S(\mathbf{p}, t_0, t) + \hbar\omega t)}{\partial t} = \frac{(\mathbf{p} - e\mathbf{A}(t))^2}{2m} + U_I + \hbar\omega = 0. \quad (\text{A.15})$$

Equation (A.13) uses the well known identity from classical mechanics $\nabla_{\mathbf{p}}H = \dot{\mathbf{x}}$ where H is the classical hamiltonian of the free electron and the fact that $S = \int(H + U_I)$. The integral may then be approximated, using such a saddle point method, by a weighted sum of the values of the integrand at these saddle points

$$\hat{d}(\omega) = \sum_n G_n(\omega) \exp\left(-\frac{i}{\hbar} S(\mathbf{p}_n(\omega), t_{0n}(\omega), t_n(\omega)) - i\omega t_n(\omega)\right), \quad (\text{A.16})$$

where weights $G_n(\omega)$ contain the dipole transition amplitudes (bound-continuum) and a factor that takes the size of the saddle point into account, while the values of $\{\mathbf{p}_n(\omega), t_{0n}(\omega), t_n(\omega)\}$ are determined by solving (A.13-A.15).

From the saddle point conditions, quite some physical insight can be gained. It is known from classical Lagrangian mechanics, that the classical trajectories lie at saddle points of the classical action³ S . Therefore the major contributions to the (quantum mechanical) dipole moment (A.12) come from the classical trajectories of the free electron in the laser field, that start at t_{0n} , with a momentum \mathbf{p}_n and end at the time t_n . The saddle point conditions above tell us about some properties of these trajectories. The momentum saddle point condition (A.13) tells us that the classical trajectories in the continuum start and end at the same point. As obviously the ground state to continuum dipole matrix elements vanish for electron positions outside the ground state wave function⁴, the quasi-free trajectories contributing to the start in the vicinity of the parent ion and also end there. The start time condition (A.14) says that the kinetic momentum $\mathbf{p} - e\mathbf{A}(t_0)$ at the start time has to be imaginary and is approximately zero for the limit of very strong fields $U_I \ll U_p$. Here U_p is the average kinetic energy of the free electron in the driving field as given in (3.8). This is an indication that a tunneling mechanism is responsible for the bound-free transition. Finally (A.15) shows that the energy of the emitted photon is equal to the kinetic energy at the end of the free trajectory plus the binding energy U_I .

A.2 Dipole spectrum for harmonic and frequency comb drive

It is interesting to look at the frequency content of the spectrum generated by the HHG process. For a harmonic driving field,

$$\mathbf{E}(t) = \mathbf{E}_0 \cos \omega_0 t, \quad (\text{A.17})$$

the Fourier spectrum of the field as well as the vector potential only have a single component at ω_0

$$\hat{\mathbf{A}}(\omega) = \hat{\mathbf{A}}_0 \delta(\omega - \omega_0). \quad (\text{A.18})$$

Because S is quadratic in $\mathbf{p} - \mathbf{A}(t)$ and $\mathbf{A}(t + n\tilde{t}/2) = (-1)^n \mathbf{A}(t)$, where $\tilde{t} = 2\pi/\omega_0$, the action is periodic with half the driving period

$$S(\mathbf{p}, t_0 + n\frac{\tilde{t}}{2}, t + n\frac{\tilde{t}}{2}) = S((-1)^n \mathbf{p}, t_0, t), \quad (\text{A.19})$$

and due to the symmetry properties of the ground state $|0\rangle$ it can easily be seen, that the dipole moment has the property

$$d(t + n\frac{\tilde{t}}{2}) = (-1)^n d(t). \quad (\text{A.20})$$

Therefore, it can be written using its Fourier transform, which contains only odd multiples of the fundamental frequency ω_0

$$d(t) = \sum_n \hat{d}_n e^{i(2n+1)\omega_0 t}. \quad (\text{A.21})$$

³Actually, the classical equations of motion are obtained from the classical action by looking for a saddle point of the action with respect to a variation of $\mathbf{p}(t)$, not a constant \mathbf{p} as it appears in (A.9). However for this particular action, those saddle points have constant \mathbf{p} , therefore condition (A.13) actually selects the classical trajectory.

⁴because the ground state wave function $|0\rangle$ is localized around the atom and falls off quickly.

As a result, only odd harmonics of the driving frequency can be generated.

This is a consequence of energy conservation, i.e. the energy of generated photons may only be the sum or difference of an (odd) number of photons from the driving field. The statement may be extended to driving field of any spectral content and specifically for the case of a frequency comb, the spectrum of the $2j + 1$ harmonic is the sum of $2j + 1$ photons⁵ of the driving field (with frequencies as in (2.8)) resulting in a spectrum with frequencies

$$\omega_n(2j + 1) = n\omega_r + (2j + 1)\omega_{CE}. \quad (\text{A.22})$$

A.3 Phase of the generated radiation

By looking at equation (A.16) it is immediately seen that the phase of each trajectory leading to an emission at the frequency ω_0 is given by its classical action via

$$\phi_n(\omega_0) = \frac{1}{\hbar}(S(p_n(\omega_0), t_{0n}(\omega_0), t_n(\omega_0)) - \omega_0 t_n) \quad (\text{A.23})$$

where $p_n(\omega_0)$, $t_{0n}(\omega_0)$, $t_n(\omega_0)$ are the canonical momentum, birth and recombination time of the n^{th} such trajectory as determined by the equations (A.13–A.15). For the case of a harmonic driving field this becomes

$$\phi_n = -\frac{U_p}{\hbar} 2 \int_{t_{0n}}^{t_n} (\sin(\omega t_{0n} - \sin(\omega t'))^2 dt' + \frac{U_I}{\hbar} t_{0n} + 3.17 \frac{U_{p\omega_0}}{\hbar} t_n \quad (\text{A.24})$$

where the cutoff intensity⁶ $U_{p\omega_0} = (\hbar\omega_0 - U_I)/3.17$ of the frequency ω_0 was introduced as a reference scale. Because the trajectories longer than one optical cycle are strongly suppressed, as mentioned in the last paragraph, it is usually sufficient to restrict the analysis to trajectories shorter than that. Then there are only two such trajectories for each dipole frequency, which are customarily called the short and long trajectories, according to their travel time τ (see figure 3.3 for $\tau < 1$). The phase variation of these two trajectories (at fixed output frequency ω_0) as a function of drive intensity will now be discussed. For drive intensities below the cutoff intensity $U_{p\omega_0}$ the frequency ω_0 will not be generated. Above the threshold the duration of the short trajectory tends to zero, as $U_p/U_{p\omega_0}$ increases. So does the classical action. A numerical analysis⁷ yields for the phase of the short trajectory

$$\phi_{short}(U_p, \omega_0) \approx \frac{2\pi U_p}{\hbar\omega_0} \left(0.88 \frac{U_p}{U_{p\omega_0}}\right)^{-1.25} + C, \quad \frac{U_p}{U_{p\omega_0}} \gg 1, \quad (\text{A.25})$$

where the remaining terms outside the integral in (A.24) are essentially constant and replaced by C . The long trajectory has a duration that is close to one cycle with a start time close to zero and

⁵or sum of $(2j+1)+m$ photons minus m photons

⁶actually the cutoff ponderomotive energy, that is linked to the cutoff intensity for radiation at ω_0 via eq. (3.8).

⁷It has to be kept in mind, that the saddle points (p_n, t_{0n}, t_n) depend on the ratio between drive and cutoff intensity, $U_p/U_{p\omega_0}$ and can not be given in closed form even for harmonic drive. Therefore a numerical analysis is necessary.

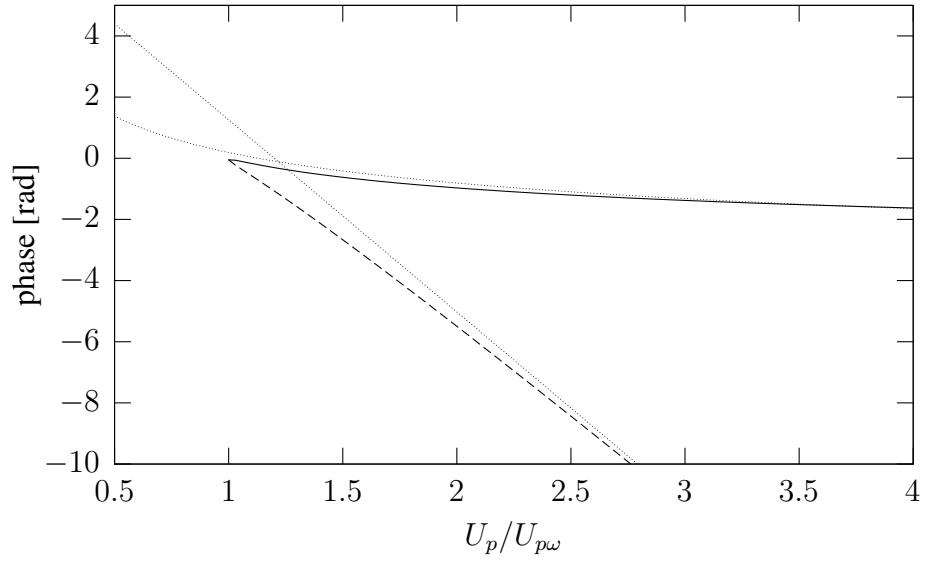


Figure A.1: Phase of the generated radiation for the short (solid) and long (dashed) trajectory from (A.24) and asymptotes (A.25) and (A.26) (dotted) for parameters $U_{p\omega_0} = U_I = \hbar\omega$

stop time at the next cycle. Therefore the integral in (A.24) is about $1/2$ and the remaining terms are about constant. Therefore the phase shift becomes

$$\phi_{long}(U_p) \approx \frac{U_p}{\hbar\omega_0} + C, \quad \frac{U_p}{U_{p\omega_0}} \gg 1. \quad (\text{A.26})$$

It is roughly linear in U_p with a slope of $2\pi/\hbar\omega$. Figure A.1 illustrates this.

Bibliography

- M. V. Ammosov, N. B. Delone and V. P. Krainov. *Tunnel ionization of complex atoms and atomic ions in a varying electromagnetic-field*. Zhurnal Eksperimentalnoi I Teoreticheskoi Fiziki, **91**, pp. 2008–2013 (1986). Translation in Soviet Physics - JETP (USA), **64**, pp. 1191-1194 (1986).
- K. W. An, C. H. Yang, E. E. Dasari and M. S. Feld. *Cavity ring-down technique and its application to the measurement of ultraslow velocities*. Optics Letters, **20**, pp. 1068–1070 (1995)
- Y. V. Baklanov and V. P. Chebotayev. *Narrow resonances of 2-photon absorption of super-narrow pulses in a gas*. Applied Physics, **12**, pp. 97–99 (1977)
- P. Balcou, P. Salières, A. LHuillier and M. Lewenstein. *Generalized phase-matching conditions for high harmonics: The role of field-gradient forces*. Physical Review A, **55**, pp. 3204–3210 (1997)
- D. Bauer and P. Mulser. *Exact held ionization rates in the barrier-suppression regime from numerical time-dependent schrodinger-equation calculations*. Physical Review A, **59**, pp. 569–577 (1999)
- M. Bellini, C. Lyngå, A. Tozzi, M. B. Gaarde, T. W. Hänsch, A. L’Huillier and C.-G. Wahlström. *Temporal coherence of ultrashort high-order harmonic pulses*. Physical Review Letters, **81**, pp. 297–300 (1998)
- G. Bonsch and E. Potulski. *Measurement of the refractive index of air and comparison with modified edlen’s formulae*. Metrologia, **35**, pp. 133–139 (1998)
- Robert W. Boyd. *Nonlinear Optics*. Academic Press, San Diego, 2nd edition (2003). ISBN 0-12-121682-9
- F. Brunner, T. Sudmeyer, E. Innerhofer, F. Morier-Genoud, R. Paschotta, V. E. Kisel, V. G. Shcherbitsky, N. V. Kuleshov, J. Gao, K. Contag, A. Giesen and U. Keller. *240-fs pulses with 22-W average power from a mode-locked thin-disk Yb:KY(WO₄)₂ laser*. Optics Letters, **27**, pp. 1162–1164 (2002)
- Y. Chen, F. X. Kartner, U. Morgner, S. H. Cho, H. A. Haus, E. P. Ippen and J. G. Fujimoto. *Dispersion-managed mode locking*. Journal of the Optical Society of America B-Optical Physics, **16**, pp. 1999–2004 (1999)

- P. B. Corkum. *Plasma perspective on strong-field multiphoton ionization*. Physical Review Letters, **71**, pp. 1994–1997 (1993)
- S. A. Diddams, L. Hollberg, L. S. Ma and L. Robertsson. *Femtosecond-laser-based optical clockwork with instability $\leq 6.3 \times 10^{-16}$ in 1 s*. Optics Letters, **27**, pp. 58–60 (2002)
- S. A. Diddams, D. J. Jones, J. Ye, T. Cundiff, J. L. Hall, J. K. Ranka, R. S. Windeler, R. Holzwarth, Th. Udem and T. W. Hänsch. *Direct link between microwave and optical frequencies with a 300 thz femtosecond laser comb*. Physical Review Letters, **84**, pp. 5102–5 (2000)
- S. A. Diddams, Th. Udem, J. C. Bergquist, E. A. Curtis, R. E. Drullinger, L. Hollberg, W. M. Itano, W. D. Lee, C. W. Oates, K. R. Vogel and D. J. Wineland. *An optical clock based on a single trapped $^{199}\text{Hg}^+$ ion*. Science, **293**, pp. 825–828 (2001)
- James Neil Eckstein. *High Resolution Spectroscopy Using Multiple Coherent Interactions*. Ph.D. thesis, Stanford (1978)
- A. Einstein. *Die grundlage der allgemeinen relativitätstheorie*. Annalen der Physik, **49**, pp. 769–822 (1916)
- A. Fernandez, T. Fuji, A. Poppe, A. Furbach, F. Krausz and A. Apolonski. *Chirped-pulse oscillators: a route to high-power femtosecond pulses without external amplification*. Optics Letters, **29**, pp. 1366–1368 (2004)
- M. Ferray, A. L’Huillier, X.F. Li, Lompré L. A., G. Mainfray and C. Manus. *Multiple-harmonic conversion of 1064 nm radiation in rare gases*. Journal of Physics B, At. Mol. Opt. Phys., **21**, p. L31 (1988)
- R. L. Fork, O. E. Martinez and J. P. Gordon. *Negative dispersion using pairs of prisms*. Optics Letters, **9**, pp. 150–152 (1984)
- T. M. Fortier, D. J. Jones and S. T. Cundiff. *Phase stabilization of an octave-spanning ti:sapphire laser*. Optics Letters, **28**, pp. 2198–200 (2003)
- T. Fuji, J. Rauschenberger, A. Apolonski, V. S. Yakovlev, G. Tempea, Th. Udem, C. Gohle, T. W. Hänsch, W. Lehnert, M. Scherer and F. Krausz. *Monolithic carrier-envelope phase-stabilization scheme*. Optics Letters, **30**, pp. 332–334 (2005)
- V. Gerginov, C. E. Tanner, S. A. Diddams, A. Bartels and L. Hollberg. *High-resolution spectroscopy with a femtosecond laser frequency comb*. Optics Letters, **30**, pp. 1734–6 (2005)
- G. Ghosh. *Dispersion-equation coefficients for the refractive index and birefringence of calcite and quartz crystals*. Optics Communications, **163**, pp. 95–102 (1999)
- C. Gohle, Th. Udem, M. Herrmann, J. Rauschenberger, R. Holzwarth, H. A. Schuessler, F. Krausz and T. W. Hänsch. *A frequency comb in the extreme ultraviolet*. Nature, **436**, pp. 234–237 (2005)

- T. W. Hänsch and B. Couillaud. *Laser frequency stabilization by polarization spectroscopy of a reflecting reference cavity*. Optics Communications, **35**, pp. 441–444 (1980)
- J. P. Heritage, E. W. Chase, R. N. Thurston and M. Stern. *A simple femtosecond optical third-order disperser*. In *Conference on Lasers and Electro-Optics*, volume 10 of *1991 Technical Digest Series*, p. 74 (1991). CTuB3
- R. Holzwarth, Th. Udem, T. W. Hänsch, J. C. Knight, W. J. Wadsworth and P. S. J. Russell. *Optical frequency synthesizer for precision spectroscopy*. Physical Review Letters, **85**, pp. 2264–2267 (2000)
- A. Huber, Th. Udem, B. Gross, J. Reichert, M. Kourogi, K. Pachucki, M. Weitz and T. W. Hänsch. *Hydrogen-deuterium $1s$ - $2s$ isotope shift and the structure of the deuteron*. Physical Review Letters, **80**, pp. 468–71 (1998)
- E. Innerhofer, T. Sudmeyer, F. Brunner, R. Haring, A. Aschwanden, R. Paschotta, C. Honninger, M. Kumkar and U. Keller. *60-w average power in 810-fs pulses from a thin-disk yb : Yag laser*. Optics Letters, **28**, pp. 367–369 (2003)
- E. Innerhofer, T. Sudmeyer, F. Brunner, R. Paschotta and U. Keller. *Mode-locked high-power lasers and nonlinear optics a powerful combination*. Laser Physics Letters, **1**, pp. 82–85 (2004)
- John David Jackson. *Classical Electrodynamics*. John Wiley & Sons, Inc. (1962). ISBN 0-471-43132-X
- R. J. Jones and J. C. Diels. *Stabilization of femtosecond lasers for optical frequency metrology and direct optical to radio frequency synthesis*. Physical Review Letters, **86**, pp. 3288–91 (2001)
- R. J. Jones, T. Ido, T. Loftus, M. Boyd, A. Ludlow, K. Holman, M. Thorpe, K. Moll and J. Ye. *Stabilized femtosecond lasers for precision frequency metrology and ultrafast science*. Laser Physics, **15**, pp. 1010–1013 (2005)
- R. J. Jones and J. Ye. *Femtosecond pulse amplification by coherent addition in a passive optical cavity*. Optics Letters, **27**, pp. 1848–1850 (2002)
- R. J. Jones and J. Ye. *High-repetition-rate coherent femtosecond pulse amplification with an external passive optical cavity*. Optics Letters, **29**, pp. 2812–2814 (2004)
- R.J. Jones and J. Ye (2005a). Private communication
- R.J. Jones and J. Ye. *Phase-coherent frequency combs in the vacuum ultraviolet via high-harmonic generation inside a femtosecond enhancement cavity*. Physical Review Letters, **94**, p. 193201 (2005b). doi:10.1103/PhysRevLett.94.193201

- V.L. Kalashnikov, C. Gohle and Th. Udem. *Maximization of ultrashort pulse power stored in a passive resonator synchronously pumped by a femtosecond oscillator*. In *Advanced Solid-State Photonics*, OSA Technical Digest, p. MB2 (2005)
- Axel Kasper. *Erzeugung und Charakterisierung ultrakurzer Lichtpulse aus Titan:Saphir Laser-Oszillatoren*. Ph.D. thesis, Fakultät für Physik der Technischen Universität München (1997)
- F. Keilmann, C. Gohle and R. Holzwarth. *Time-domain mid-infrared frequency-comb spectrometer*. *Optics Letters*, **29**, pp. 1542–1544 (2004)
- L. V. Keldysh. *Ionization in field of a strong electromagnetic wave*. *Soviet Physics JETP-USSR*, **20**, pp. 1307–1314 (1965)
- W. H. Knox, N. M. Pearson, K. D. Li and C. A. Hirshman. *Interferometric measurements of femtosecond group delay in optical components*. *Optics Letters*, **13**, pp. 574–6 (1988)
- H Kogelnik and T Li. *Laser beams and resonators*. *Proceedings of the IEEE*, **54**, pp. 1312–1329 (1966)
- F. Kottmann, W. Amir, F. Biraben, C. A. N. Conde, S. Dhawan, T. W. Hänsch, F. J. Hartmann, V. W. Hughes, O. Huot, P. Indelicato, L. Julien, P. Knowles, S. Kazamias, Y. W. Liu, F. Mulhauser, F. Nez, R. Pohl, P. Rabinowitz, J. M. F. Dos Santos, L. A. Schaller, H. Schneuwly, W. Schott, D. Taqqu and Jfca Veloso. *The muonic hydrogen lamb shift experiment at psi*. In *Hyperfine Interactions*, volume 138, pp. 55–60. Kluwer Academic Publishers., Netherlands (2001)
- M. Kourogi, B. Widiyatomo, Y. Takeuchi and M. Ohtsu. *Limit of optical-frequency comb generation due to material dispersion*. *IEEE Journal of Quantum Electronics*, **31**, pp. 2120–6 (1995)
- A. P. Kovács, K. Osvay, Z. Bor and R. Szipöcs. *Group-delay measurement on laser mirrors by spectrally resolved white-light interferometry*. *Optics Letters*, **20**, pp. 788–90 (1995)
- K. C. Kulander, K.J. Schafer and J.L. Krause. *Super-Intense Laser-Atom Physics*, volume 316 of *NATO Advanced Study Institute, Series B*, p. 95. Plenum, New York (1993)
- L.D. Landau and E.M. Lifschitz. *Quantenmechanik*. Akademie-Verlag, 2nd edition (1966)
- M. Lewenstein, P. Balcou, M. Y. Ivanov, A. L’Huillier and P. B. Corkum. *Theory of high-harmonic generation by low-frequency laser fields*. *Physical Review A*, **49**, pp. 2117–2132 (1994)
- J. Limpert, T. Clausnitzer, A. Liem, T. Schreiber, H. J. Fuchs, H. Zellmer, E. B. Kley and A. Tunnermann. *High-average-power femtosecond fiber chirped-pulse amplification system*. *Optics Letters*, **28**, pp. 1984–1986 (2003)

- J. Limpert, T. Schreiber, T. Clausnitzer, K. Zollner, H. J. Fuchs, E. B. Kley, H. Zellmer and A. Tunnermann. *High-power femtosecond yb-doped fiber amplifier*. Optics Express, **10**, pp. 628–638 (2002)
- F. Lindner, W. Stremme, M. G. Schatzel, F. Grasbon, G. G. Paulus, H. Walther, R. Hartmann and L. Struder. *High-order harmonic generation at a repetition rate of 100 kHz*. Physical Review A, **68**, p. 013814 (2003)
- I. H. Malitson. *Refraction and dispersion of synthetic sapphire*. Journal of the Optical Society of America, **52**, pp. 1377–1379 (1962)
- A. Marian, M. C. Stowe, J. R. Lawall, D. Felinto and J. Ye. *United time-frequency spectroscopy for dynamics and global structure*. Science, **306**, pp. 2063–2068 (2004)
- G. Materlik and Th. Tschentscher. *Tesla technical design report, part v*. Technical report, DESY (2001)
- Gail McConnell, Allister I Ferguson and Nigel Langford. *Cavity-augmented frequency tripling of a continuous wave mode-locked laser*. Journal of Physics D, **34**, pp. 2408–2413 (2001)
- J. D. McMullen. *Analysis of compression of frequency chirped optical pulses by a strongly dispersive grating pair*. Applied Optics, **18**, pp. 737–741 (1979)
- A. McPherson, Gibson G., Jara H., U. Johann, T. S. Luk, I. A. McIntyre, Boyer K. and Rhodes C.K. *Studies of multiphoton production of vacuum-ultraviolet radiation in the rare gases*. Journal of the Optical Society of America B, **5**, p. 595 (1987)
- A. A. Michelson. *On the application of interference methods to spectroscopic measurements*. Phil. Mag., **34**, p. 280 (1891)
- A. A. Michelson and E. W. Morley. *On the relative motion of the earth and the luminiferous ether*. American Journal of Science, **34**, pp. 333–345 (1887)
- Tobias Nebel. *Measuring the Group Delay Dispersion of Optical Elements*. Master's thesis, Fakultät für Physik der Ludwig-Maximilians-Universität München (2005)
- M. Niering, R. Holzwarth, J. Reichert, P. Pokasov, Th. Udem, M. Weitz, T. W. Hänsch, P. Lemonde, G. Santarelli, M. Abgrall, P. Laurent, C. Salomon and A. Clairon. *Measurement of the hydrogen 1s-2s transition frequency by phase coherent comparison with a microwave cesium fountain clock*. Physical Review Letters, **84**, pp. 5496–9 (2000)
- A. O'Keefe and D. A. G. Deacon. *Cavity ring-down optical spectrometer for absorption measurements using pulsed laser sources*. Review of Scientific Instruments, **59**, pp. 2544–51 (1988)
- Edward D. Palik (editor). *Handbook of Optical Constants of Solids II*. Academic Press, New York (1991). ISBN 0-12-544422-2

- M.A. Persaud, J.M. Tolchard and A.I. Ferguson. *Efficient generation of picosecond pulses at 243 nm*. IEEE Journal of Quantum Electronics, **27**, pp. 1253–1258 (1990)
- J. C. Petersen and A. N. Luiten. *Short pulses in optical resonators*. Optics Express, **11**, pp. 2975–2981 (2003)
- J. Reichert, R. Holzwarth, Th. Udem and T. W. Hänsch. *Measuring the frequency of light with mode-locked lasers*. Optics Communications, **172**, pp. 59–68 (1999)
- J. Reichert, M. Niering, R. Holzwarth, M. Weitz, Th. Udem and T. W. Hänsch. *Phase coherent vacuum-ultraviolet to radio frequency comparison with a mode-locked laser*. Physical Review Letters, **84**, pp. 3232–5 (2000)
- L. Ricci, M. Weidemüller, T. Esslinger, A. Hemmerich, C. Zimmermann, V. Vuletic, W. König and T. W. Hänsch. *A compact grating-stabilized diode laser system for atomic physics*. Optics Communications, **117**, pp. 541–9 (1995)
- B. Rossi and D. B. Hall. *Variation of the rate of decay of mesotrons with momentum*. Physical Review, **59**, pp. 223–228 (1941)
- Jacques Rutman. *Characterization of phase and frequency instabilities in precision frequency sources: Fifteen years of progress*. Proceedings of the IEEE, **66**, pp. 1048–1075 (1978)
- C. Sáinz, P. Jourdain, R. Escalona and J. Calatroni. *Real time interferometric measurements of dispersion curves*. Optics Communications, **110**, pp. 381–90 (1994)
- Schott. *Catalogue Optisches Glas*. Schott Geschäftsbereich Optik (1984)
- M. J. Snadden, A. S. Bell, E. Riis and A. I. Ferguson. *Two-photon spectroscopy of laser-cooled Rb using a mode-locked laser*. Optics Communications, **125**, pp. 70–76 (1996)
- R. Szipocz, K. Ferencz, C. Spielmann and F. Krausz. *Chirped multilayer coatings for broad-band dispersion control in femtosecond lasers*. Optics Letters, **19**, pp. 201–203 (1994)
- H. R. Telle. *Frequency Control of Semiconductor Lasers*, chapter 5, pp. 137–172. Microwave and Optical Engineering. Wiley & Sons, Inc. (1996)
- P. Tournois. *Acousto-optic programmable dispersive filter for adaptive compensation of group delay time dispersion in laser systems*. Optics Communications, **140**, pp. 245–249 (1997)
- Th. Udem, S. A. Diddams, K. R. Vogel, C. W. Oates, E. A. Curtis, W. D. Lee, W. M. Itano, R. E. Drullinger, J. C. Bergquist and L. Hollberg. *Absolute frequency measurements of the Hg^+ and Ca optical clock transitions with a femtosecond laser*. Physical Review Letters, **86**, pp. 4996–9 (2001)
- Th. Udem, A. Huber, B. Gross, J. Reichert, M. Prevedelli, M. Weitz and T. W. Hänsch. *Phase-coherent measurement of the hydrogen 1s-2s transition frequency with an optical frequency interval divider chain*. Physical Review Letters, **79**, pp. 2646–9 (1997)

- Th. Udem, J. Reichert, R. Holzwarth and T. W. Hänsch. *Accurate measurement of large optical frequency differences with a mode-locked laser*. Optics Letters, **24**, pp. 881–3 (1999a)
- Th. Udem, J. Reichert, R. Holzwarth, T.W. Hänsch and M Kourogi. *The measurement of large optical frequency differences and the design of a new type of frequency chain*. In *Proceedings of the 1999 Joint Meeting of the European Frequency and Time Forum and the IEEE International Frequency Control Symposium*, volume 2, pp. 620–625 (1999b)
- R. S. Van Dyck Jr., P. B. Schwinberg and H. G. Dehmelt. *New high-precision comparison of electron and positron g-factors*. Physical Review Letters, **59**, pp. 26–29 (1987)
- Y. Vidne, M. Rosenbluh and T. W. Hänsch. *Pulse picking by phase-coherent additive pulse generation in an external cavity*. Optics Letters, **28**, pp. 2396–2398 (2003)
- J. von Zanthier, Th Becker, M. Eichenseer, AYu Nevsky, Ch Schwedes, E. Peik, H. Walther, R. Holzwarth, J. Reichert, Th. Udem, T. W. Hänsch, P. V. Pokasov, M. N. Skvortsov and S. N. Bagayev. *Absolute frequency measurement of the In^+ clock transition with a mode-locked laser*. Optics Letters, **25**, pp. 1729–31 (2000)
- Masayoshi Watanabe, Ryuzo Ohmukai, Kazuhiro Hayasaka, Hidetsuka Imajo and Shinji Urabe. *High-power second-harmonic generation with picosecond and hundreds-of-picosecond pulses of a cw mode-locked ti:sapphire laser*. Optics Letters, **19**, pp. 637–639 (1994)
- A. M. Weiner, D. E. Leaird, J. S. Patel and J. R. Wullert. *Programmable shaping of femtosecond optical pulses by use of 128-element liquid-crystal phase modulator*. Ieee Journal of Quantum Electronics, **28**, pp. 908–920 (1992)
- A. Wicht, K. Danzmann, M. Fleischhauer, M. Scully, G. Muller and R. H. Rinkleff. *White-light cavities, atomic phase coherence, and gravitational wave detectors*. Optics Communications, **134**, pp. 431–9 (1997)
- S. Witte, R. T. Zinkstok, W. Ubachs, W. Hogervorst and K. S. E. Eikema. *Deep-ultraviolet quantum interference metrology with ultrashort laser pulses*. Science, **307**, pp. 400–403 (2005). doi:10.1126/science.1106612
- V. P. Yanovsky and F. W. Wise. *Frequency doubling of 100-fs pulses with 50% efficiency by use of a resonant enhancement cavity*. Optics Letters, **19**, pp. 1952–1954 (1994)
- G. L. Yudin and M. Y. Ivanov. *Nonadiabatic tunnel ionization: Looking inside a laser cycle*. Physical Review A, **6401**, pp. art. no.–013409 (2001)
- R. Zerne, C. Altucci, M. Bellini, M. B. Gaarde, T. W. Hänsch, A. L’Huillier, C. Lyngåand C. G. Wahlstrom. *Phase-locked high-order harmonic sources*. Physical Review Letters, **79**, pp. 1006–9 (1997)

M. Zimmermann, C. Gohle, R. Holzwarth, Th. Udem and T. W. Hänsch. *Optical clockwork with an offset-free difference-frequency comb: accuracy of sum- and difference-frequency generation*. *Optics Letters*, **29**, pp. 310–12 (2004)

Roel Th. Zinkstok, Stefan Witte, Wim Ubachs, Wim Hogervorst and Kjeld S.E. Eikema. *Demonstration of frequency comb laser spectroscopy in the vacuum-ultraviolet*. In *Conference on Lasers and Electrooptics* (2006)

Danke

Ich möchte mich an dieser Stelle herzlich bei allen bedanken, die mich in den letzten vier Jahren tatkräftig unterstützt und damit diese Arbeit erst ermöglicht haben.

An erster Stelle steht hier Thomas Udem, der mich mit Begeisterung in das für mich neue Thema der optischen Frequenzmessung einführte, mir half ein spannendes Projekt in diesem Gebiet zu finden und mir bei Problemen stets mit Rat und Tat, aber auch mit albernem Sprüchen zur Seite stand.

Professor Theodor W. Hänsch danke ich dafür, mich in seine Arbeitsgruppe aufgenommen zu haben und weil er mir völlig freie Hand bei der Wahl und Ausführung meines Themas lies und dennoch regelmässig neue Ideen und Ausstattung hervor zauberte, um die Umsetzung zu einem erfolgreichen Ende zu führen.

Die Fallsteller, eine ganz neuen Spezies in unsere Arbeitsgruppe, Maximilian Herrmann und Frank Markert haben so fest an mein Projekt geglaubt, dass sie verwegene genug waren, bereits ein Ionenfallenexperiment vorzubereiten, ohne zu wissen ob die Spektroskopiequelle funktionieren würde. Das hat mich ungemein angespornt. Vielen Dank. Überhaupt war das Arbeitsklima in der Gruppe stets entspannt und die Diskussionen und anderen Geschichten während der Kaffeepause und im Biergarten interessant, hilfreich und amüsant. Dafür danke ich Stellvertretend Marcus Zimmermann, Peter Fendel, Ronald Holzwarth, Tobias Nebel, Brigitta Bernhard und Katherina Predehl. In kritischen Phase habe ich tatkräftige Unterstützung von der Ultraschnellen Eingreiftruppe unter der Leitung von Ferenz Krausz erhalten. Besonders hervorzuheben ist Jens Rauschenberger, der sich so begeistern ließ, dass er gleich umgesattelt hat. Aber auch die Hilfe von Alma Fernandez, Roswita Graf und Alexander Apolonskiy sind hier zu erwähnen. Grosser dank gebührt auch allen die mir immer wieder meine Schusseligkeit verzeihen, selbst wenn ich vergesse sie hier zu erwähnen.

Ganz besonderer Dank gilt meiner Familie, insbesondere meiner Frau Doris, die mich stets liebevoll zu Zeiten der Stagnation ermuntert und bei Übereifer gebremst hat sowie meinen zwei Töchtern, Marlene und Laura, die nicht nur die Menge meines Schlafes reduziert sondern auch mein Leben entscheidend bereichern haben.

Zuletzt möchte ich noch meinen Eltern danken, die mir das alles überhaupt ermöglicht haben.

Vielen Dank!

Lebenslauf

Christoph Gohle

- 5.12.1973 Geburt in München
- 1980-1984 Besuch der Grundschule in der Grandlstrasse in München
- 1984-1993 Besuch des Max-Planck Gymnasiums in München
- 1993-1994 Wehrersatzdienst in München
- 1994-2001 Studium zum Diplomphysiker an der Ludwig-Maximilians-Universität in München
- 2001 Drei Monate Praktikum am BEC-Experiment der Gruppe Rempe
am Max-Planck-Institut für Quantenoptik in Garching
- 2001-2006 Doktorand am Frequenzkammexperiment der Gruppe Hänsch
am Max-Planck-Institut für Quantenoptik in Garching